ECHO PARTICLE IMAGE/TRACKING VELOCIMETRY: TECHNICAL DEVELOPMENT AND *IN VIVO* APPLICATIONS IN CARDIOVASCULAR AND CEREBROVASCULAR FLOWS

by
Zeng Zhang

A dissertation submitted to Johns Hopkins University in conformity with the requirements for the degree of Doctor of Philosophy

Baltimore, Maryland
March 2023

© 2023 Zeng Zhang
All Rights Reserved

Abstract

Contrast-enhanced ultrasound (CEUS) imaging utilizes intravascular echogenic microbubbles (1-5µm in diameter) to visualize the blood flow in various organs. In this dissertation, we develop and implement techniques for analyzing the motions of microbubbles to quantify cardiovascular and cerebrovascular flows.

Obtaining accurate bubble center locations from noisy CEUS images is a primary challenge. Since the bubble trace is typically modeled as a point scatter convolved with a point spread function (PSF), techniques including blind deconvolution, supervised, and self-supervised learning are introduced and calibrated for identifying the PSF and locating the bubble center. The enhanced CEUS images enable echo particle image velocimetry (echo-PIV) for characterizing 2D cardiovascular flows, and the global-optimized Kalman filter-based echo particle tracking velocimetry (echo-PTV) for determining bubble trajectories which are subsequently used for mapping the cerebral and ocular microcirculation at a spatial resolution of 20µm.

These techniques are applied to two applications. First, echo-PIV is used for monitoring the aortic root flow in an adult pig undergoing veno-arterial extracorporeal membrane oxygenation (VA-ECMO), a life support technology whose parameters can be optimized based on the aortic root hemodynamics. Phase-averaged and instantaneous flow fields show that, for the pig with severe myocardial ischemia, the cardiac ejection velocity, velocity-time integral, and mean arterial pressure (MAP) reach their peak at an ECMO flow rate of 3.0L/min, indicating an optimal flow rate that provides adequate support.

Second, we investigate non-invasive methods for estimating intracranial pressure (ICP), a critical parameter for hydrocephalus patients that cannot be invasively measured safely. Echo-PTV is used to map cerebral and ocular microcirculation of pediatric hydrocephalus porcine models for inferring ICP. Results show that accounting for pulse pressure, highly correlated relationships between ICP and cortical microcirculation density are obtained with correlation coefficients beyond 0.85. For cerebral ischemia, nondimensionalized cortical micro-perfusion decreases by an order of magnitude when the ICP exceeds 50% of MAP. Moreover, retinal microcirculation also shows a highly correlated relationship with ICP when accounting for pulse pressure. These findings suggest that CEUS-based microcirculation measurement is a plausible noninvasive method for evaluating the ICP and detecting brain ischemia.

Primary Reader and Advisor: Professor Joseph Katz

Secondary Readers: Professor Gretar Tryggvason, Professor Misun Hwang

Acknowledgments

I would like to express my sincere gratitude to all those who have supported me throughout my doctoral studies.

First and foremost, I want to express my deepest appreciation to my parents, Mr. Songlin Zhang and Mrs. Guimin Zhang, for their love, support, and encouragement throughout my life. I would not have made it this far without them. As I reflect on the 2050 days and nights that I spent in Baltimore, I faced many challenges and setbacks, and there were countless sleepless nights. But whenever I felt overwhelmed, I would think back to the memories of the times we spent together, drinking soda and talking in the middle of a summer night. Those memories have been my source of strength and comfort, even though we are thousands of miles apart. I am so fortunate to have parents like them, who teach me the value of hard work, determination, and perseverance, who always put their children's needs first and provide a loving home, and who have been my rock, my inspiration, and my guiding light. I am so grateful to have them in my life, and my love for them is more than words can express.

My heartfelt thanks also go to my advisor, Prof. Joseph Katz, I am truly grateful for his exceptional guidance, encouragement, and support. I cannot thank him enough for giving me the opportunity to work and study at a world-class school that has changed my life. He has challenged me to think critically and creatively, and his insights and knowledge have expanded my horizons and broadened my perspectives. I have gained valuable skills and experiences that will serve me well in my future endeavors. His mentorship has helped me grow both as a researcher and as a person, and I am grateful for his unwavering commitment to my success.

I would then like to acknowledge my collaborator, Prof. Misun Hwang, for her guidance in this field of research and for providing me with the professional laboratory conditions that have allowed me to pursue my research interests. Her positive and hardworking attitude has been a model for me to follow, and her dedication to work has inspired me to strive for excellence in everything that I do.

I would also like to express my gratitude to several esteemed faculty members. Professors Rajat Mittal, Charles Meneveau, and Gretar Tryggvason have served in my department qualification exam, while Professors Aleksander Popel, Darryn Waugh, Rui Ni, and Rajat Mittal have contributed significantly as my Graduate Board Oral (GBO) examination committee members. Most notably, I extend my heartfelt appreciation to thesis readers Professors Gretar Tryggvason and Misun Hwang, who have generously dedicated their time to review and offer invaluable insights into my work.

I am grateful for the support and collaboration of numerous friends and colleagues who have contributed their professional expertise and assistance throughout my doctoral journey. From the Children's Hospital of Philadelphia, I would like to thank Prof. Todd Kilbaugh, Drs. Anush Sridharan, Sophie Haddad, Mrigendra Karmacharya, Sunil Unnikrishnan, Theodore Cary, and Laith Sultan, as well as Sarah Morton, Anthony Davis, Yuxi Lin, and Takayuki Sueishi. From the Johns Hopkins University School of Medicine, my appreciation extends to Drs. Xun Zhou, Alejandro Suarez-Pierre, and Cecillia Lui, along with Sean Kearney, Enoch Yeung, Prof. Henry Halperin, and Prof. Chun Woo Choi. Additionally, I am grateful for the support of my colleagues at Johns Hopkins University, including Drs. Kaushik Sampath, Omri Ram, Lakshmana Dora, Jin Wang, Jian Gao, Huang Chen, Yuanchao Li, Xinzhi Xue, Jibu Tom Jose, Subhra Shankha Koley, Karuna Agarwal, Diego Muriel Delgado, and Spencer Zimmerman, as well as Yuhui Lu, Ayush Saraswat, Subhamoy Gupta, Deepan Sharma, Changyang Tan, Chintan Panigrahi, Suker Li, Rayce Martin, Barbara Adamson, Yury Ronzhes, Xianyang Chen, Yang Liu, Hongjin Wang, Yifan Du, and Lei Zeng. Each of their contributions to my research projects has been vital, and their hard work and dedication have played a crucial role in helping me achieve my goals.

And last, but certainly not least, I want to express my deepest appreciation and love to my girlfriend, Miss Yuxi Zhou, for her remarkable patience and understanding. With her unwavering support and infinite tolerance, she has remained steadfastly by my side despite the challenges of time, distance, and unforeseen circumstances that we have faced over the years. The promise of a future together has been a constant source of motivation and inspiration during difficult times, endowing me with exceptional courage. Additionally, I extend my appreciation to her family for their care and concern, which have been invaluable throughout this journey.

Dedication

To

Mr. Songlin Zhang, Mrs. Guimin Zhang, and Miss Yuxi Zhou

in gratitude for their unwavering love, encouragement, and sacrifices

"To ordain conscience for heaven and earth;

To secure life and fortune for the people;

To continue lost teachings for past sages;

To establish peace for all future generations."

Contents

Abstract ii

Acknowledgments iv

Dedication vii

Contents viii

List of Tables xi

List of Figures xii

Chapter 1. Introduction 1

1.1. Contrast-enhanced ultrasound imaging (CEUS) and echo particle image/tracking velocimetry (echo-PIV/PTV) 1

1.2. Enhancement of CEUS images 2

1.3. Monitoring cardiovascular flows during veno-arterial extracorporeal membrane oxygenation (VA-ECMO) 5

1.4. Non-invasive assessment of intracranial pressure (ICP) for hydrocephalus 6

1.5. Dissertation outline 9

Chapter 2. CEUS Imaging and Data Processing 11

2.1. Animal management 11

2.2. CEUS imaging 14

2.2.1. CEUS imaging using clinically available ultrasound scanners 14

2.2.2. CEUS imaging using ultrafast ultrasound scanners 17

2.3. CEUS image enhancement 18

2.3.1. Blind deconvolution 18

2.3.2. Generation of synthetic images for training and evaluating neural networks 20

2.3.3. U-net for blind deconvolution 24

2.3.4. Super-resolution neural network for blind deconvolution (SupBD-net) 26

2.3.5. Self-supervised neural network for blind deconvolution (SelfBD-net) 29

2.4. Optimized echo-PIV 36

2.5. Echo-PTV and ultrasound localization microscopy (ULM) 37

Chapter 3. Evaluation of Data Processing Methods 40

3.1. Uncertainties in bubble center location for echo-PIV and echo-PTV 40

3.1.1. Bubble localization by blind deconvolution and supervised learning methods 40

3.1.2. Bubble localization by self-supervised learning 43

3.2. The spatial resolution of vessel detection for echo-PTV and ULM 49

3.2.1. Evaluation of the spatial resolution based on synthetic images 49

3.2.2. Evaluation of the spatial resolution and velocity measurement via real CEUS data 56

Chapter 4. Application of Echo-PIV in Cardiovascular Flows 61

4.1. Background: monitoring cardiac flows during VA-ECMO 61

4.2. Phase-averaged flow field 62

4.3. Characterization of cardiac outflow during VA-ECMO 63

Chapter 5. Application of Echo-PTV in Cerebral and Ocular Blood Flows 68

5.1. Background: non-invasive ICP assessment and brain ischemia detection using cerebral and ocular microcirculation 68

5.2. Visualization of the cerebral vasculature 69

5.3. Quantification of the impact of elevated ICP on the cerebral blood flow........................... 71

5.4. Microdialysis and cerebral microcirculation during ischemia 79

5.5. The impact of ICP on the pulsatility of cerebral blood flow.. 83

5.6. Quantification of the impact of elevated ICP on the ocular blood flow............................. 85

5.7. Discussions about the advantages and limitations of the current method........................... 86

Chapter 6. Conclusion 91

Bibliography 94

Curriculum Vitae 107

List of Tables

Table 2-1 Test cases and baseline information of the pediatric porcine models for cerebrovascular flow measurement. 12

List of Figures

Figure 2-1 Illustration of the problems in raw CEUS images and sample results of blind deconvolution. (a) A sample raw CEUS image of a porcine's coronal brain section. A bubble trace (white box) is magnified at the top right to show its millimetric scale, which is much larger than its physical size (~5μm). A group of closely seated bubbles is marked in the yellow circle showing the difficulty in distinguishing them. The dashed boxes are the moving interrogation windows used for estimating the local PSF. (b) The corresponding estimated spatial distribution of PSF. Highlighted in the white, yellow, and blue dashed boxes are the PSFs corresponding to the same windows in (a). (c) A sample enhanced image after blind deconvolution. 18

Figure 2-2 The procedure for generating the synthetic images. The prescribed centers with various peak intensities are generated at 10 times the original image resolution and are convolved with a PSF interpolated to the same scale. The resulting image is down-sampled to the native image resolution and combined with the background noise with realistic intensity distribution. The subarea of a CEUS image containing a similar PSF is demonstrated next to the synthetic data. .. 20

Figure 2-3 The PDF of the relative RMS intensity difference (ε_k) between the original PSFs and the up-and-down-sampled ones. 22

Figure 2-4 An illustration of the network structure of U-net. The current U-net consists of 3 encoder levels, a bridging level, and 3 decoder levels. In each encoding step, the input information is processed by a convolution block (ConvBlock, detail shown in top right), consisting of two successive 3×3 2D convolution layers, each followed by a Rectified Linear Unit (ReLU) layer. The output of the ConvBlock is downsized by half using a 2×2 max pooling layer and passed on to the next ConvBlock where the feature channels are doubled. A dropout layer, which randomly drops

20% of the input features, is used after the bridging step to prevent overfitting. Subsequently, the incoming information is upsized by 2 in decoding steps using a transposed convolution followed by ReLU (UpConv, detail shown in bottom right), concatenated with the output of the encoding layers at the same level, and processed by the ConvBlock. For each decoder layer, the feature channels are reduced by half. Finally, a convolution layer is used for generating the 2D image outputs. The output size of each step is marked as image size × number of feature channels below each block. 25

Figure 2-5 An illustration of the network structure of SupBD-net. The current SupBD-net consists of two ConvBlocks for extracting lower-level features of the CEUS image, four local residual blocks (ResBlock) along with one global residual block for higher-level feature extraction, one transpose convolution layer for upscaling, one final convolution layer for converting higher dimensional features into 2D images, and a sigmoid layer to ensure a 0-1 intensity range of the output image. The image size × number of feature channels are listed above each block. The bottom left shows the components of ConvBlock in SupBD-net, including a 2D convolution layer followed by an Instance Normalization (IN) layer and a Leaky Rectified Linear Unit (LeakyReLU) layer. The bottom right shows the components of the residual blocks, input information is processed by a 2D convolution layer followed by IN, LeakyReLU, another 2D convolution, and IN. The output of the last IN is added to the input of the whole ResBlock and passed on to the following layers.... 28

Figure 2-6 An illustration of the network structure of SelfBD-net. Shown in the top left is an additional network, named k-net, used for estimating the PSF from the raw CEUS image. The k-net shares the same preprocessing and local-global residual blocks as SupBD-net, followed by another ConvBlock and a final convolution layer for generating outputs. Here, all the convolution kernels in k-net are 7×7. The k-net and the pretrained x-net are jointly trained on the CEUS images with unknown PSFs using the loss functions provided in the top right. Here, the x-net is selected as SupBD-net, but it can be other pretrained networks for identifying the bubble centers. 30

Figure 2-7 Comparison of the signal-to-noise ratio (SNR) for image intensity, gradient, and hessian. (a) A sample comparison of a clean synthetic CEUS image (left) versus the same one with added noise at a typical level (right). From top to bottom, demonstrated images are image intensity, gradient magnitude, and the magnitudes of the first and second eigenvalues of image hessian. The corresponding SNR for the noisy image is listed in the bottom right of each image. (b) The SNR PDF for 2500 noisy synthetic CEUS images with a typical bubble density and noise level. The dashed line shows the center SNR level for image intensity, and the red dots show the center SNR level for each value. 31

Figure 2-8 The procedures for training SelfBD-net. (a) Step 1: updating the k-net while freezing the x-net. While x-net is prone to generate a cluster of false detections around the true center, the brightest one in each cluster is used for approximating the true center and for calculating the loss functions. After 40 iterations, the k-net converges and learns to deform the gaussian disk to resemble the true PSF shown on the right. (b) Step 2: freezing the k-net and updating layers after the global residual learning in x-net. The first 50 iterations are demonstrated where the false detections (red circle) in the x-net output are gradually removed and the closely seated bubbles (green circle) are separated. The resulting estimated bubble centers are close to the true centers shown on the right........ 34

Figure 2-9 Image preprocessing and bubble tracking procedures. (a) A sample raw CEUS image. (b) The spatial distribution of the point spread function estimated by blind deconvolution. (c) The enhanced image after deconvolution and modified histogram equalization. (d) A heatmap of the centers of all the detected bubbles. (e) The bubble tracking process highlighting several strategies used for detecting likely trajectories. Exposures are color coded as indicated in the legend. (f) Illustrations of strategies for data association to determine the optimal non-overlapping trajectories. 37

Figure 3-1 Sample images demonstrating the raw synthetic image, true bubble center map, and the center maps obtained based on blind deconvolution, U-net, and SelfBD-net. The scale bar is provided at the bottom right of the raw image and the image size is listed at the bottom of each one. Enclosed in the yellow circle are two closely seated bubbles that cannot be separated by blind deconvolution, can be separated with distinguishable centers by U-net, and are fully separated by SupBD-net. Enclosed in the red circle are falsely enhanced noises by blind deconvolution. 41

Figure 3-2 Variations of the mean error in the detected bubble center (E_c - bars) and its standard deviation (error bars) for varying bubble concentration (columns), peak noise levels (rows), and PSF area and aspect ratio (horizontal axis). Black bars: blind deconvolution, blue bars: U-net, and red bars: SupBD-net. The left vertical axis shows values in μm and the right shows values in pixels. 43

Figure 3-3 Visualization of the SelfBD-net outputs. (a) A comparison of the true (top row) and the estimated PSFs (bottom row) along with their 2D correlation coefficient (Q). (b) A sample case comparing the output of each method. Here, enclosed in the yellow box are two closely seated bubbles that are only correctly distinguished by the SelfBD-net. 44

Figure 3-4 Evaluation of SelfBD-net using vertically oriented PSFs. Variations of E_c (a) and the percentage of falsely detected bubbles (λ, b) with increasingly elongated PSFs under a bubble concentration of 0.5mm^{-2} and a peak noise level of 0.16. For the PSF with an aspect ratio of 1.81, also shown are the variations of E_c with increasing noise level under a bubble concentration of 0.5mm^{-2} (c) and with increasing bubble concentration under a peak noise of 0.16 (d). For a,c, and d, the left vertical axis shows values in μm and the right in pixels. For a-d, the bar height shows mean values and the error bar shows the standard deviation. 45

Figure 3-5 Evaluation of SelfBD-net using the same dataset as Section 3.1.1 with horizontally oriented PSFs, a bubble concentration of 0.5mm^{-2}, and a peak noise level of 0.16. (a) Variations of the percentage of unseparated bubbles with the normalized bubble distance, which is defined for each bubble as the distance to its nearest neighbor normalized by the length of the PSF FWHM along the line connecting the two centers (D^*). (b) Comparison of E_c between SelfBD-net and SupBD-net for increasing PSF size. The left vertical axis shows values in μm and the right in pixels. The bar height shows mean values and the error bar shows the standard deviation. 48

Figure 3-6 Spatial resolution of closely located parallel lines for different image processing methods. (a) Sample heatmaps of bubble trajectories showing the effect of increasing line spacing (D_l). (b) Sample cross-sectional profiles showing the effect of PSF FWHM length in the direction perpendicular to the line (L_p). The definitions of the error in line location (E_l) and line width (σ_l) are indicated in the top left. For (a) and (b), the vertical dashed lines show the true location of each line. 49

Figure 3-7 Variations of nondimensionalized: (a) line location error (E_l^*), and (b) line width (σ_l^*) with PSF size (L_p^*). All variables are nondimensionalized by the corresponding line spacing. The red line shows the least-square-fitted power law, whose expression as well as the coefficient of determination (R^2) are provided at the bottom of each panel. The solid dots denote data of horizontal lines, and hollow dots represent data of vertical lines. 52

Figure 3-8 Determining the threshold for negligible ghost lines using Support Vector Machine (SVM). (a) Sample illustration of the definition of the parameters, namely, the area ratio occupied by each line structure, p_1, and the linewise mean/standard deviation of the intensity for each peak which is normalized by the maximum peak, p_2. (b) Scatter plots of p_1 and p_2, as well as the decision boundaries estimated by the SVM. The red dots represent data of ghost lines, the blue dots represent data of primary lines, and the black encircled ones are the support vectors. A few examples are shown on the right side demonstrating cases with negligible ghost lines (cases 1-4), and inngeligble ones (cases 5-8). 53

Figure 3-9 Summarization of the ability of each method to separate closely located parallel lines for all D_l and L_p. 55

Figure 3-10 Visualization of cortical microvasculature in the left cerebral hemisphere of a piglet. (a) Maps of blood vessels obtained by different image processing methods. White-enclosed subregions are magnified to demonstrate their abilities to reconstruct a cluster of microvessels. (b) A magnified view of the blue-enclosed region in (a). Two cross-sectional profiles along four closely spaced microvessels (line 1) and two moderately spaced microvessels (line 2) are provided to compare the spatial resolution of different methods. (c) A magnified view of the yellow-enclosed region in (a), where the cross-sectional profile along a moderate blood vessel (line 3) is provided for all methods comparing their abilities to identify the location and width of such vessels. 59

Figure 3-11 Evaluation of the velocity measurement. (a) A scatter plot comparing the phase averaged velocities measured by echo-PTV and pulsed-wave Doppler ultrasound. Results beyond the maximum PTV measurement range (11 cm/s), and below the minimum range of Doppler measurements (1 cm/s), are not included. Most of the micro-vessel data fall below the doppler limit. (b) A Bland-Altman plot comparing the PTV and Doppler measurements, with the mean value and the 95% confidence interval highlighted. (c) A comparison of the PTV- and Doppler-measured phase-averaged velocity distributions in a blood vessel at varying intracranial pressure levels. .. 60

Figure 4-1 Vectors and contour maps of the phase-averaged velocity magnitude ($|V|$) for varying ECMO flow rates (rows) and phases in the cardiac cycle (columns). The ECMO flow rate is indicated on the left, and the cardiac phase in the bottom. A reference vector is provided in the top left corner. The sample electrocardiogram (ECG) corresponds to Q_E=4.0L/min. 62

Figure 4-2 Sample instantaneous images of the aortic valve for Q_E=3.0L/min showing the distance between valve tips (D_A). Indicated in the first column is the location and orientation of the line ox_c located 0.8cm away from the sino-tubular junction where v_c is measured. 63

Figure 4-3 (a) Sample spatio-temporal evolution of v_c along the line ox_c for Q_E=4.0L/min. (b) Phase-averaged velocity distributions (V_c) along the line ox_c for each Q_E. 64

Figure 4-4 (a) Phase evolution of the spatially averaged velocity $\langle V_c \rangle$. (b) Phase evolution of the rate of change of $\langle V_c \rangle$ ($\langle a_c \rangle = \partial \langle V_c \rangle / \partial t$). 65

Figure 4-5 (a) Variations of maximum velocity ($\langle V_c \rangle^{\max}$), maximum deceleration magnitude ($|\langle a_c \rangle^{\min}|$), the phase interval between valve opening and closing ($\Delta\Phi_{\mathrm{open}}$), and phase of the maximum deceleration ($\Phi_{a_c^{\min}}$) with Q_E. (b) Variations of velocity-time integral (VTI) over 1min calculated from $\langle V_c \rangle$, and MAP during image acquisition with Q_E. 66

Figure 5-1 Cerebral vascular map and velocity distribution for piglet #0121 at the baseline ICP. (a) A heatmap of all the trajectories containing at least 4 exposures visualizing the micro- and macro-vascular distributions in a coronal plane. The blue star marks the location of the pulsed-wave Doppler ultrasound measurement. (b) The corresponding time-averaged velocity distribution. (c) Several sub-regions are labeled for statistical analysis of perfusion, including the micro-vessels in the thalamus (#1), several parts of the cortex (#2, #3, and #4), as well as a macro blood vessel (#5). A few regions are magnified to provide a closer view of the current regions of interest. Sample velocity profiles across two different blood vessels are also provided in (c). 69

Figure 5-2 Visualization and quantification of the influence of increasing ICP on cerebral perfusion. (a) Sample visualizations of cerebral blood vessels (top row) and the corresponding velocity distributions (bottom row) of piglet #0121 with increasing ICP. (b-d) Relationships between the ICP and the Cerebral Microcirculation (CMC, original cohort) parameter of the thalamus (b), cortical subregion #2 (c), and all three cortical subregions combined (d, $\mathrm{CMC_{cort}}$). (e) Relationships between the ICP and the time-averaged velocity (V_5) in the macro blood vessel #5 at the point marked with a blue star in (a). For (b-e) data are presented as mean ± SD, where the error bars show the temporal standard deviations of CMCs or V_5 over n=20 cardiac phases. The curves are least-square fitted quadratic functions, with the corresponding coefficient of determination (R^2) shown on each plot. Also presented are the correlation coefficients (r) and the corresponding P values between the CMCs or V_5 and the ICP. (Figures attached on the next page.) 71

Figure 5-3 Exploring different combinations of perfusion and hemodynamic parameters aimed at improving the correlation with the ICP. (a) Relationships between hemodynamic parameters and ICP for all the piglets. From left to right: MAP, systolic (SBP) and diastolic blood pressure (DBP), pulse pressure (PP=SBP-DBP), and cerebral perfusion pressure (CPP=MAP-ICP). (b) Variations of the CMC_{cort} with hemodynamic parameters. (c) Variations of combinations of hemodynamic parameters with ICP. (d) Variations of CMC_{cort} with combinations of hemodynamic parameters. For (c, d), each plot contains a least square fitted curve along with its R^2, as well as r and P. 76

Figure 5-4 Combining the perfusion parameters with hemodynamic variables to obtain highly correlated functional relationships for the assessment of ICP. (a) A heatmap of R^2 of the least-squared fits between a series of hemodynamic parameters and CMC (or V_5). (b) A heatmap of R^2 of the least-squared fits between the ICP and the combined hemodynamic-perfusion parameters. Here, two-way ANOVA multiple comparison results with Benjamini-Hochberg correction are also demonstrated, where 'ns' indicates P=0.72, '**' P=0.0016, and '***' P=0.0001. (c-i) Variations of CMC/PP with ICP, in the: (c) combined cortical regions (#2-4); (d) thalamus (#1), and cortical subregions #2 (e), #3 (f), and #4 (g); (h) combined thalamus and cortical data (#1-4); and (i) macro vessel. Corresponding values of R^2 for the parabolic curve fit, as well as r and P for the two-tailed Pearson correlation, are provided for each plot. (j-p) Trends of PP-(0.17CMC-0.29)MAP with ICP in the: (j) combined cortical regions (#2-4); (k) thalamus (#1), and cortical subregions #2 (l), #3 (m), and #4 (n); (o) combined thalamus and cortical data (#1-4); and (p) macro vessel. Here, the corresponding R^2 for the fitting, as well as r and P for the two-tailed Pearson correlation are shown. For (c-p) the functions are developed based on the original cohort (colored symbols) and validated by validation data (hollow symbols). Subscript ‘ori’ denotes the values based on the original cohort, while ‘all’ denotes the values based on original and validation cohorts combined. (Figures attached on the next page.) 77

Figure 5-5 The relative errors in ICP prediction based on the (a) parabolic function in Figure 5-4c and (b) linear function in Figure 5-4j for the original (closed bar) and validation (open bar) data. For (a, b), the bar height denotes the mean value with the error bar showing the standard deviation. Here, two-way ANOVA multiple comparison results with Benjamini-Hochberg correction are also demonstrated, where ‘ns’ $P>0.05$, ‘*’ $P<0.05$, ‘**’ $P<0.01$, and ‘***’ $P<0.001$. 79

Figure 5-6 Microdialysis results. (a) Pyruvate. (b) Lactate. (c) Glycerol. (d) Glucose. 79

Figure 5-7 Comparison to microdialysis data showing a drastic reduction in perfusion once cerebral ischemia occurs. (a) Trends of lactate-to-pyruvate ratio (L/P) with increasing ICP for the current experiment (circles) and previously reported results (cross, Zoremba et al. 2007). The dashed line at L/P=30 has been suggested as the threshold for cerebral ischemia (Purins et al. 2012). (b) Trends of L/P vs. the nondimensionalized cortical micro-perfusion parameter $\rho(\mathrm{CMC_{cort}})^2/\mathrm{PP}$. (c) Trends of $\rho(\mathrm{CMC_{cort}})^2/\mathrm{PP}$ with $\mathrm{ICP/MAP}$ in logarithmic scales. In (a-c), the same group of encircled cases is identified to have cerebral ischemia, all occurring at $\mathrm{ICP/MAP} \geq 0.5$. (d) Variations of $\rho V_5^2/\mathrm{PP}$ with $\mathrm{ICP/MAP}$. (e and f) A sample comparison of the baseline (e) and ischemia (f) cases for piglet #0306 showing the omnipresent sharp reduction in perfusion during ischemia. 81

Figure 5-8 Relationships between nondimensional perfusion parameters and $\mathrm{ICP/MAP}$ in different parts of the brain. The locations of measurements include microcirculation in the: (a) Thalamus, and cortical regions #2 (b), 3 (c), and 4 (d), as well as: (e) the combined cortical microcirculation in regions #2-4, (f) The combined microcirculation in regions #1-4, and (g) the velocity in macro blood vessel #5. All cases whose L/P>30 are marked in the triangle. In (a-f), the fitted functions are based on the data of the original cohort, along with their R^2, the correlation coefficients and P values for the two-tailed Pearson correlation. 82

Figure 5-9 Influence of increasing ICP on the pulsatility of the micro-perfusion. (a) Variations with the cardiac phase of the phase-averaged CMC (over 250 cardiac cycles) after subtracting the systolic value ($\Delta \mathrm{CMC}_{\Phi}$). Data are presented as mean ± SD, where error bars indicate the standard deviations among cases. (b) Trends of the maximum cyclic variations in micro-perfusion ($\left|\Delta \mathrm{CMC}_{\Phi}\right|_{\max}$) with increasing ICP for different brain regions. (c) The nondimensional cyclic variations in CMC for the cortex regions combined, $\rho\left|\Delta \mathrm{CMC}_{\Phi \mathrm{cort}}\right|_{\max}^{2} / \mathrm{PP}$, plotted vs. $\mathrm{ICP} / \mathrm{MAP}$. The encircles cases correspond to the ischemia cases marked in Figure 5-7. (d) The pulsatility index for the $\mathrm{CMC}_{\mathrm{cort}}$. Corresponding values of R^2 for the parabolic curve fit, as well as r and P (0.0006) for the two-tailed Pearson correlation, are provided. 83

Figure 5-10 Variations of ocular vascular blood flow with increasing ICP. (a) Sample vasculatures in eight parallel ocular axial planes at ICP=9mmHg. (b) Visualization of the effect of increasing ICP on the retinal microvascular heatmaps (left) and the average blood flow velocity (right). (c) Heatmaps (left) and velocity (right) in the retrobulbar major vasculature with increasing ICP. (d) The Retinal Microcirculation Coefficient (RMC) scaled by the PP plotted vs. the ICP. (e) Variations of the mean velocity in the retrobulbar major vessels scaled by PP with increasing ICP. In d and e, each color indicates a different pig, and the yellow curve is a parabolic least-square fit to the data. The corresponding R^2 and r are indicated on each plot. 85

Figure 5-11 The time-intensity curve analysis of disruption & replenishment sequences. Columns (left to right): values of the cortex, thalamus, cortex/thalamus, and the whole coronal plane. Rows (top to bottom): parameters including peak intensity, refilling rate, rise time, average wash-in slope (k), max intensity/k, and area under the curve of the wash-in phase (WIAUC). The ischemia cases are marked by black boxes. The R^2 for each parabolic fit is provided. 88

Chapter 1. Introduction

1.1. Contrast-enhanced ultrasound imaging (CEUS) and echo particle image/tracking velocimetry (echo-PIV/PTV)

Visualization and quantification of macro- and micro-vascular blood flows provide vital information about hemodynamic conditions and could guide timely surgical interventions for various types of diseases (Vincent et al. 2011). As a convenient bedside tool, Contrast-Enhanced Ultrasound (CEUS) imaging visualizes cardiovascular flows (Schinkel et al. 2016) and neonatal cerebral perfusion (Hwang 2019) by observing the motions of intravascular echogenic microbubbles (1-5μm in diameter). Conventional data analysis monitors the variations in CEUS image intensity over time to estimate the perfusion (Greis 2011). Meanwhile, several postprocessing techniques have been developed to obtain quantitative blood flow information by analyzing the motions of bubbles, such as echo Particle Image Velocimetry, echo-PIV (Crapper et al. 2000; Kim et al. 2004; Poelma 2017; Zhang et al. 2020), and echo Particle Tracking Velocimetry, echo-PTV (Sampath et al. 2018; Jeronimo et al. 2020; Zhang et al. 2022).

In echo-PIV, the CEUS image is divided into small interrogation windows and the spatially averaged velocity of microbubbles in each window is determined by the cross-correlation of successive frames (Adrian et al. 2011). This method has been applied for characterizing flows associated with cardiomyopathy, heart failure, and acute myocardial infarction (Abe et al. 2013; Mangual et al. 2013; Agati et al. 2014; Martínez-Legazpi et al. 2014). Echo-PTV, which tracks bubbles over time, has been used to refine PIV results (Keane et al. 1995; Sampath et al. 2018). For example, Sampath et. al. (Sampath et al. 2018) introduces a multiparameter-based procedure, which integrates image enhancement, PIV, and PTV to obtain an optimized flow field measurement.

More importantly, the bubble tracks obtained by echo-PTV enable the reconstruction of microvascular structures and flows in various organs at a spatial resolution of less than 20μm, a technique referred to as Ultrasound Localization Microscopy (ULM) in the ultrasound community (Siepmann et al. 2011; Viessmann et al. 2013; Desailly et al. 2013; Christensen-Jeffries et al. 2014; Ackermann and Schmitz 2016a). Pioneering *in vivo* works include the demonstration of isolated microbubble tracing in tumor vessels (Siepmann et al. 2011), and the super-resolution flow mapping in a mouse ear (Christensen-Jeffries et al. 2014). Subsequently, this method has been used for reconstructing the cerebral and renal vascular systems in rodent models (Errico et al. 2015; Foiret et al. 2017; Lin et al. 2017), as well as for detecting a small deep-seated human cerebral aneurysm (Demené et al. 2021). Early applications have used pre-clinical/clinical CEUS scanners with framerates typically less than 100 frames per second (Siepmann et al. 2011; Viessmann et al. 2013; Christensen-Jeffries et al. 2014; Opacic et al. 2018), and recent studies have already utilized ultrafast ultrasound imaging, extending to more than 1000 frames per second (Errico et al. 2015; Demené et al. 2021). Further details can be found in a recent review article (Couture et al. 2018).

1.2. Enhancement of CEUS images

Obtaining accurate microbubble locations is vital for the fidelity of echo-PIV and PTV measurements. This is particularly emphasized for ULM because the spacing between micro-vessels is typically much smaller than the size of the bubble trace (~500μm) in the CEUS image. Given that the actual microbubble diameter is one order of magnitude smaller than the pixel size, the bubble trace can be modeled as a convolution of a point scatter with a spatially varying Point Spread Function (PSF). Among the techniques developed to assess the bubble center location, some previous studies have developed deconvolution procedures for estimating the local PSF (Foroozan et al. 2018; Zhang et al. 2020) and removing it from the bubble trace. Others have estimated the PSF as a 2D gaussian fit to the trace of individual bubbles and then detected the bubble center from correlations of this PSF with the CEUS images (Demené et al. 2021). In both cases, the localization accuracy is adversely affected by the spatially varying background noise, and by the presence of overlapping traces. Recent studies have shown that the deconvolution of CEUS images using end-to-end deep learning could reduce the error in bubble location by 75% (Liu et al. 2020), and could be more than 60 times faster than conventional blind deconvolution methods (Bai et al. 2019). Similarly, superior processing speed and accuracy by deep learning methods have also been demonstrated by van Sloun et al. (2020). Inspired by these improvements, the current study also utilizes deep learning but introduces a super-resolution method that improves the accuracy of the measurements. Moreover, a self-supervised approach is proposed that detects bubble centers only based on raw CEUS images without the reference of true bubble locations. Hence, such a method is generalizable to a broad range of CEUS imaging applications with very different PSFs.

The current study starts with the classic U-net (Ronneberger et al. 2015) architecture as a baseline, which is widely used for medical imaging and has been reported to deliver good performance in image enhancement, object detection, and morphometry (Falk et al. 2019). This U-net is trained for an end-to-end task that extracts the true centers of bubble traces from raw CEUS images at the native image resolution, e.g., 60μm/pix. Then, to achieve higher sub-pixel precision, we utilize an image super-resolution technique, where the resulting image has a smaller pixel size. While Isola et al. (2017) use U-net for this purpose, a later study (Wang et al. 2018) shows that the quality of results is improved by replacing the U-net with a series of local and global residual blocks (He et al. 2016). Residual learning prevents the vanishing and/or exploding gradients (Glorot and Bengio 2010) as well as the degradation problems (He and Sun 2015) in deep learning. Hence, it is particularly suitable for constructing very deep neural networks, leading to improved performance (He et al. 2016). Consequently, residual learning has been widely applied to generate super-resolution images (Ledig et al. 2017; Lim et al. 2017a). Therefore, we adopt this approach to develop a supervised Super-resolution Blind Deconvolution network (SupBD-net) for improving the detection of the bubble centers. The primary challenge in the application of supervised learning to CEUS images is the variability of noise levels, backgrounds, and bubble trace morphologies, which are affected by the types of contrast agent and transducer, as well as the image setting, depth, and organ structure. To overcome these issues, the training dataset should have broad characteristics, an objective achieved by generating synthetic data involving PSFs with random magnifications and orientations as well as varying background noise and bubble densities.

Finally, we introduce a self-supervised method that does not need to be trained based on references of true bubble locations by integrating ideas derived from the conventional blind deconvolution approach, namely the minimization of mean square error between the original image and the estimated bubble center convolved with the estimated PSF. This blind deconvolution approach also uses additional regularization terms based on prior knowledge that the physical size of the bubble is smaller than one pixel, i.e., it is a point scatter, hence the number of non-zero pixels around the bubble center should be minimal in the output. Mimicking this procedure, the proposed Self Blind Deconvolution network (SelfBD-net) uses two jointly trained networks, one for estimating the PSF, and the second, which is based on the pretrained SupBD-net, for detecting the bubble center. The only information required for training this network pair is the raw CEUS image, hence it can be utilized for processing CEUS images with unknown PSFs.

The performances of blind deconvolution, U-net, SupBD-net, and SelfBD-net are evaluated by realistic synthetic images involving a wide range of PSF morphologies, background noise levels, and bubble densities. Criteria include the error in bubble center location and the percentage of failed detections in cases of closely seated bubbles. Moreover, the performance of SelfBD-net is also tested based on synthetic images that have substantially different PSFs than the training set, in particular for cases where U-net and SupBD-net fail. Furthermore, the overall performance in localization and tracking is evaluated by testing the ability of these methods to distinguish between closely separated parallel bubble trajectories. The results show that the deep learning-based procedures substantially outperform blind deconvolution, both in terms of processing speed and detection accuracy.

Based on the enhanced images, this dissertation applies the echo-PIV and PTV techniques to two applications. In the first one, we use echo-PIV to monitor the cardiovascular flows in the aortic root during the veno-arterial extracorporeal membrane oxygenation (VA-ECMO) for estimating the optimal ECMO flow rate. In the second one, we use echo-PTV to measure the microvascular flows in the brain and eye for the non-invasive assessment of intracranial pressure. The backgrounds and importance of such applications are introduced in the following sections.

1.3. Monitoring cardiovascular flows during veno-arterial extracorporeal membrane oxygenation (VA-ECMO)

VA-ECMO is a salvage therapy that provides patients with both respiratory and circulatory support by draining blood from the venous system, oxygenating it outside the body, and returning it retrograde to the arterial system (Pavlushkov et al. 2017). The most commonly applied configuration is femoral-femoral VA-ECMO, in which the arterial ECMO flow to the patient is retrograde via the femoral artery. It has been widely applied to patients with cardiogenic shock, severe cardiac failure, and chronic cardiomyopathy (Makdisi and Wang 2015). However, determining the optimal VA-ECMO flow rate (Q_E) is challenging (Martin et al. 1991; Becker et al. 1998). High Q_E is favorable for adequate end-organ perfusion. Nonetheless, it has been proposed that retrograde arterial flow may increase the afterload to the heart (Burkhoff et al. 2015; Rao et al. 2018). Consequently, the metabolic work demand on the myocardium might increase, hindering myocardial tissue recovery (Ostadal et al. 2015). Clinical management relies on monitoring the hemodynamic states (Chung et al. 2014; Schmidt et al. 2015), but outcomes of the therapy are influenced by patient- and treatment-related factors (Lim et al. 2017b; Donker et al. 2019). Insights regarding the interactions between ECMO flows and native cardiac output at the admixing zone may lead to a quantitative assessment of the impact of the afterload created by the retrograde arterial ECMO flow.

While a series of numerical studies have examined the effect of VA-ECMO on the flow structures in the ascending and descending aorta (Assmann et al. 2012; Stevens et al. 2017, 2018; Gu et al. 2018, 2019; Zhang et al. 2018), to the best of our knowledge, there is no corresponding experimental data. In contrast, there is considerable information on the flow in the aortic root involving applications of mostly phase-contrast MRI (Kilner et al. 1993; Kvitting et al. 2004; Markl et al. 2004; Hope et al. 2007, 2010; Morbiducci et al. 2011), but also vector flow imaging utilizing multi-directional doppler ultrasound (Hansen et al. 2015, 2016, 2017), both of which do not involve applications of ECMO. Hence, in this dissertation, we use the optimized echo-PIV to characterize the interactions between ECMO flow and native cardiac output in the aortic root of an adult Yorkshire pig with severe myocardial ischemia. The choice to focus on the aortic root is based on the expectation that the flow structure there might be affected by direct interactions between the cardiac and ECMO flows. The instantaneous and phase-averaged velocity distributions are analyzed to elucidate the effects of the ECMO flow rate on the flow patterns, as well as the duration and magnitude of cardiac outflow.

1.4. Non-invasive assessment of intracranial pressure (ICP) for hydrocephalus

Hydrocephalus involves abnormal cerebrospinal fluid (CSF) accumulation in the brain ventricles (Tully and Dobyns 2014). Affecting 1.1‰ of infants (Munch et al. 2012), it is the leading cause of brain surgery in newborns and results in long-term neurologic disabilities in up to 78% of patients (Fernell et al. 1993; Kahle et al. 2016). Intracranial hypertension and ventriculomegaly are major complications of hydrocephalus (Shakeri et al. 2008; Kahle et al. 2016), which could lead to compromised cerebral blood flow (CBF), brain ischemia, inflammation, secondary neurovascular damage, and brain herniation (Adams-Chapman et al. 2008; Kahle et al. 2016). Aimed at alleviating the elevated intracranial pressure (ICP), the most common treatment consists of CSF diversion to another anatomical location outside of the central nervous system via an invasive ventricular shunt (Shakeri et al. 2008). The clinical decision for this surgical intervention relies primarily on computed tomography (CT) depicting ventriculomegaly following clinical symptomatology (Shakeri et al. 2008; Tully and Dobyns 2014). Unfortunately, by the time of radiographic diagnosis of ventriculomegaly, the ICP is often elevated significantly, and the brain tissue is at risk of ischemia and irreversible brain damage. Compounding the difficulty of early diagnosis and intervention, medical or surgical, is the fact that some patients have an elevated ICP without ventricular enlargement (Reed Murtagh et al. 1979; Iskandar et al. 1998; Zorc et al. 2002). Therefore, a brain CT is often not sensitive enough to detect an elevated ICP and ongoing ischemia, placing the infant at risk for permanent brain damage. Hence, there is a dire need for other techniques that could guide timely treatment.

Since accurate ICP measurements utilizing invasive sensors are rarely adopted due to the risks associated with infection, catheter tract hemorrhage, parenchymal damage, and neurological deficits (Zhang et al. 2017), considerable efforts have been invested in developing noninvasive methods (Khan et al. 2017). They include transcranial Doppler (Kolarovszki et al. 2013), MRI (Leliefeld et al. 2008), near-infrared spectroscopy (NIRS) (Kirkpatrick et al. 1995), diffuse correlation spectroscopy (Ruesch et al. 2020), and venous ophthalmodynamometry (Firsching et al. 2011). These clinical studies have shown that hydrocephalus is associated with increased ICP (Firsching et al. 2011), reduced CBF (Leliefeld et al. 2008; Kolarovszki et al. 2013; Yeom et al. 2014), reduced cerebral oxygen saturation, and increased oxygen extraction (Kochan et al. 2017). However, prior studies have shown that the global CBF (Leliefeld et al. 2008) or flow indices in macro-vessels (Hanlo et al. 1995) are inadequate for monitoring the ICP. In contrast, several *in-vivo* results have shown that capillary rarefaction and significantly declined capillary flows are associated with elevated ICP (Bragin et al. 2011; Dai et al. 2016). It has also been reported that when cerebral perfusion pressure (CPP) is reduced, the percentage changes to microvascular flow in several cerebral regions, including the bregma, striatum, cortex, and cortical rim, are significantly higher than the changes to the total CBF (Zaharchuk et al. 1999). Accordingly, histology and microscopy in animal studies and autopsies have demonstrated associations among hydrocephalus, increased ICP, decreased capillary density within the cortical parenchyma, and microvascular injury (Wozniak et al. 1975; Oka et al. 1985; Nakada et al. 1992; Caner et al. 1993). Furthermore, animal studies have shown that the increased capillary resistance due to an elevated ICP causes non-nutritive thoroughfare channel shunt flow, which leads to tissue hypoxia (Bragin et al. 2011). These findings suggest that a parameter that accounts for the cerebral micro-perfusion, including the density of micro-vessels and the velocity in them, could be used as a potential marker for ICP and ischemia associated with hydrocephalus. Implementing such a method requires techniques capable of mapping the microvascular perfusion in various organs at a high spatial resolution, which could be applied in clinical settings. Hence, in this dissertation, we implement ULM in a high-fidelity porcine model of neonatal hydrocephalus, which has a close approximation to human anatomy and hemodynamic response (Duhaime et al. 2000), to quantify the relationship between ICP and the spatio-temporal distribution of cerebral blood flow. Note that such a model simulates the unclosed anterior fontanel of neonates, facilitating high-quality CEUS imaging (Hwang 2019). However, the quality of data in adults or older children is expected to be inferior due to transcranial imaging. Hence, we have also explored the relationships between ocular microcirculation and ICP since the central retinal arteries and veins are exposed to the CSF.

Using a clinical CEUS system and a particle tracking velocimetry method, we map the micro- and macro-circulations in the brain and eye of hydrocephalic pediatric pig models at varying ICP levels. The data are used for visualizing and quantifying the changes to the spatial distribution of perfusion in the brain and eye. Quantitative analysis of perfusion is performed using the time-averaged velocity in the macro-vessels, and a cerebral or retinal microcirculation (CMC/RMC) parameter for the regional microvascular perfusion, which accounts for the concentration of micro-vessels and the velocity in them. Combining the cortical CMC or retinal RMC with hemodynamic parameters leads to highly-correlated functional relationships with the ICP. Furthermore, when the lactate to pyruvate (L/P) ratio obtained from cerebral microdialysis exceeds the ischemic threshold, there is a significant decrease in the cortical CMC. These findings suggest that the CEUS-based microcirculation measurements could potentially serve as a noninvasive tool for evaluating the ICP level and detecting brain ischemia in hydrocephalus.

1.5. Dissertation outline

This dissertation consists of two major topics, namely the development and evaluation of techniques for echo-PIV and PTV as well as the *in vivo* applications of these techniques in cardiovascular and cerebrovascular flows. The experimental procedures, as well as the newly developed image enhancement and data analysis techniques, are introduced in Chapter 2. Subsequently, these methods are evaluated based on the synthetic data and real CEUS images in Chapter 3. In Chapter 4, the application of echo-PIV to monitor the cardiovascular flows in the aortic root during VA-ECMO is discussed, where the optimal ECMO flow rates can be determined based on the flow structures and parameters. Then, the application of echo-PTV for measuring cerebral and ocular microcirculation is discussed in Chapter 5. Based on the measurements, highly correlated relationships between the cortical and retinal microperfusion with ICP are discovered, which can be used for the non-invasive assessment of ICP and the detection of brain ischemia. Chapter 6 concluded the whole dissertation. Overall, the development and implementation of echo-PIV and PTV techniques for analyzing CEUS images have significant potential for improving diagnostic and treatment outcomes in various medical fields, including cardiology, neurology, and critical care medicine. With ongoing advancements in image processing and machine learning algorithms, these techniques may become more efficient and widely applicable, providing a non-invasive and accurate method for assessing blood flow and detecting abnormalities in patients.

Further research and clinical trials will be essential to fully realize the potential of these technologies in improving patient care.

Chapter 2. CEUS Imaging and Data Processing

This chapter covers procedures for managing animals and performing CEUS imaging on both clinically available and ultrafast ultrasound scanners. Additionally, it introduces newly developed image processing techniques designed specifically for dealing with noisy CEUS images. Finally, the chapter discusses methods for the quantitative analysis of CEUS images, including the optimized ultrasound image velocimetry (echo-PIV), as well as globally optimized Kalman filter-based ultrasound tracking velocimetry (echo-PTV).

2.1. Animal management

In this dissertation, studies involved the measurements of macrovascular aortic flows during VA-ECMO and microvascular flows in the brain and eye for the noninvasive assessment of ICP. Hence, the choices of animal models and their management procedures varied between macro and micro-vascular flow studies, which are described in detail below.

For cardiovascular flow imaging, the study was approved by the Institutional Animal Care and Use Committee of Johns Hopkins University. The experiments were performed on a female adult Yorkshire pig (30kg). The animal underwent endotracheal intubation and general anesthesia with inhaled isoflurane. Systemic heparin was administered (5000 IU) intravenously, and cannulas for ECMO and monitoring lines were placed. Vascular access was obtained in the bilateral femoral veins and arteries, jugular veins, and right carotid artery. Through percutaneous access under fluoroscopic guidance, a 3.0×8.0mm coronary angioplasty balloon (Sprinter Legend, Medtronic, MN, Minnesota, USA) was placed across the left anterior descending coronary artery and inflated for the duration of the experiment to induce severe myocardial ischemia. The ECMO flow was introduced for two rounds through peripheral cannulation of the femoral artery and vein, starting

5min after inducing ischemia. For each round, the flow rate, Q_E, was initiated at 4.0L/min and then decreased successively by 0.5L/min down to 1.5L/min. During the first round, Q_E was kept constant for 3min at each step while recording the hemodynamic parameters, including mean arterial pressure (MAP), left and right ventricular pressures, and electrocardiogram (ECG). The left ventricular pressure catheter was removed before the second round to prevent shadowing in the aortic root, facilitating ultrasound imaging. For the second round, Q_E was kept constant for 10min at each step for the CEUS imaging.

Table 2-1 Test cases and baseline information of the pediatric porcine models for cerebrovascular flow measurement.

	Piglet Number	Weight (kg)	Baseline MAP (mmHg)	Baseline PP (mmHg)	Baseline ICP (mmHg)	Tested ICP Levels (mmHg)	Microdialysis
Original cohort	#0117	10.30	63.76	20.70	8.08	8[a],17,21,23,28	No
	#0121	10.10	68.44	15.62	7.26	7,14,18,23,29,41,46[b]	Yes
	#0122	10.80	83.17	28.70	14.41	14,22,23,30,38,39,61	Yes
	#0211	11.20	65.81	20.64	6.97	7,19,20,28,47	Yes
	#0306	9.50	62.93	24.23	9.02	9,16,22,25,31,38,55	Yes
Validation cohort	#0212	11.90	105.59	35.01	6.78	7,14,21,33,42,60	Yes
	#0219	10.50	98.22	26.31	2.65	3,13,21,30,34,47,57	Yes
	#0713	10.20	74.90	23.90	9.40	9,21,28,35,39	Yes

[a] Not included owing to inconsistency in imaging plane.
[b] Microdialysis data unavailable owing to unstable physiological condition.

For the cerebral microvascular flow imaging, the study was approved by the Institutional Animal Care and Use Committee of the Children's Hospital of Philadelphia. The original cohort consisted of five 4-week-old female piglets (10±0.65kg, Table 2-1), which had been identified as high-fidelity models for human children (Duhaime et al. 2000). Additional three (10.8±0.91kg) were used for validation. All piglets received anesthesia with intramuscular injection of ketamine (20-40mg/kg) and xylazine (1.5-3mg/kg), followed by inhaled 4% isoflurane and 100% FiO_2 via snout mask. After endotracheal intubation, mechanical ventilation was provided in 21% FiO_2 and 2% isoflurane to maintain anesthesia. For hemodynamic monitoring and intravenous fluid administration, the right femoral artery and bilateral femoral veins were cannulated under ultrasound guidance. The heart rate, respiratory rate, arterial blood pressure, ECG, and rectal temperature, were recorded for the duration of the experiments. The arterial blood pressure signals collected by an invasive hemodynamics monitoring sensor (Millar, USA) were compiled using the Blood Pressure Module of the LabChart software (ADInstruments, USA) to obtain the systolic and diastolic pressures. During the period of image acquisition, the systolic and diastolic pressures were stable with a maximum variation of ±3mmHg. The data analysis was based on the time-averaged hemodynamics values during the period of image acquisition. As for neuromonitoring, burr holes were prepared for the placement of a parenchymal ICP monitor (NEUROVENT PTO, Raumedic, Germany), a brain tissue oxygen monitor (Licox, Integra LifeSciences, USA), and a cerebral microdialysis catheter (CMA 71 Elite, mDialysis, Sweden). The ICP transducer was inserted through the right parietal bone, 1cm from both the coronal and sagittal sutures, and 2cm below the skull entering the subdural space. The Licox catheter system was placed via a frontal burr hole, terminating at the grey-white matter junction. The microdialysis catheter was placed through the right parietal bone and inserted 1 cm into the brain parenchyma. To simulate hydrocephalus, a ventricular catheter was inserted into the left lateral ventricle for the delivery of artificial cerebrospinal fluid. It was infused at a rate needed for elevating the ICP to the desired level, as shown in Table 2-1, indicated by continuous ICP monitoring. On average it took about 40min to increase the ICP by 10mmHg. The microdialysate samples were collected for each ICP level and analyzed for pyruvate, lactate, glycerol, and glucose using an automated ISCUS Flex Microdialysis Analyzer (mDialysis, Sweden) and LABpilot software (mDialysis, Sweden). At the end of each experiment, the animal was euthanized using potassium chloride.

The ocular microvascular flow imaging was conducted based on the same hydrocephalic pediatric porcine models as that of cerebral microvascular flow imaging. There were four 4-week-old female piglets (10±0.47kg) involved in this study. All of the animal preparation and management protocols, including anesthesia, ventilation, temperature management, cannulation, neuromonitoring, hemodynamic monitoring, and elevation of ICP incrementally from 10 to 50mmHg in a step of 10mmHg, followed the procedures described above.

2.2. CEUS imaging

2.2.1. CEUS imaging using clinically available ultrasound scanners

In this dissertation, the imaging of cardiovascular and cerebrovascular flows was conducted based on different clinically available ultrasound systems. The detailed imaging procedures, as well as the choice and delivery of contrast agents, are described below.

For cardiovascular flow imaging, the contrast-enhanced echocardiography was performed using the GE Vivid-E9 system (GE Healthcare, Chicago IL, USA) with a 6VT-D transesophageal probe. The choice to use a transesophageal probe, instead of a transthoracic probe, which was commonly utilized in clinical applications, was the low quality of the images captured by the latter in the pig's left ventricle and aorta, too low for the velocity measurement. The images were acquired in the mid-esophageal long-axis view, focusing on the aortic root. All of the smoothing and speckle removal functions were turned off to maximize the number of detected bubbles. Data were recorded in the '2D' mode instead of the 'contrast' mode, which was typically used for CEUS imaging, to maximize the frame rate and to retain clear images of the aortic walls and valve needed for defining the region of interest (ROI). Subsequently, the mechanical index was kept below 0.2, and the ultrasound beam sector was narrowed and tilted to focus only on the aortic root. The scanning depth was also tuned to bring the aortic root to about 2/3 of the total depth for an optimal view. Under these settings, the current system achieved an image acquisition rate of 75 frames per second. For each Q_E level, 2mL of 1.5:40 diluted contrast agent (Definity, Lantheus Medical Imaging, Billerica MA, USA) was administered through the arterial cannula (OptiSite, Edwards Lifesciences, Irvine CA, USA) and flushed with 10mL saline. Based on the examination of numerous datasets from a pre-study, we found that a bubble concentration of 60-80 bubbles per cm^2 would be optimal for the image quality achieved in this study. At this concentration, there were as many bubbles as possible in the image needed for the PIV analysis, which the image enhancement procedures (described in the following section) could detect, separate from adjacent bubbles, determine their centers, and track them across frames. Because of the bolus injection, the bubble concentration varied over time. During the wash-in phase, which started 30-60s after the injection, the high bubble concentration saturated the image, making it unsuitable for PIV/PTV. Subsequently, during the wash-out phase, the concentration gradually decreased for a period of 60-120s. During part of this period, the bubble concentration decreased to the 60-80 bubbles/cm^2 range, which was an optimal condition for detection and tracking. To ensure that we did not miss this period, the data acquisition started a few seconds earlier and stopped when the concentration decreased below the optimal range. The entire data acquisition period for each condition lasted usually for 15 cardiac cycles. A fraction of the recorded images, typically two-thirds, contained decipherable traces in the optimal range. By opting to process data obtained during 10 cycles, we were able to maintain a consistent number of cycles for all the ECMO flow rates. It should be noted that longer periods could have been chosen if the bubble were infused continuously at a moderate concentration.

For cerebrovascular flow imaging, all of the CEUS scans were performed using the Siemens ACUSON Sequoia system (Siemens Medical Solutions, USA). To mimic the neonatal skull and obtain clear images, a 2×2cm^2 cranial window was drilled upper right to the midline in the parietal region with intact dura. The window was selected to fit the tip of the 9EC4 transducer (Siemens Medical Solutions, USA), with the probe tip in contact with the dura. It should be noted that while the cranial window affected the amount of CSF required for reaching a certain ICP level, e.g., 6 times more CSF was needed for reaching ICP=40mmHg with the cranial window, the indicated ICP values are measured directly and reflects the actual pressure exerted on the brain tissue. The ultrasound probe was aligned in the coronal plane containing the maximum transverse diameter of the bilateral thalami and then fixed to the experimental table using a stereotactic arm. The piglet's head was also fixed to the table to minimize the motion caused by breathing. Due to the wide velocity range in this plane, over 10 cm/s in the large blood vessels and less than 1cm/s in micro-vessels, it was necessary to acquire the images at the highest possible framerate. Hence, the ultrasound sector width was reduced to focus on one hemisphere, allowing image acquisition at a rate of 48 frames per second. For each level, the ICP was kept steady for 5min to ensure that the hemodynamic conditions were stabilized before CEUS imaging. Then, a pulsed-wave Doppler measurement was conducted for the major blood vessels. Subsequently, a bolus of 0.2mL Lumason (Bracco Diagnostics, USA) was prepared following the manufacturer's instructions, injected manually, and followed by a quick flush of 10mL saline. The image acquisition of bolus injection took 90s. Then a veterinary syringe pump (Practivet, USA) was connected to the femoral vein catheter to deliver the Lumason steadily at 0.6mL/min for the bubble tracking procedures. The pump was gently shaken during the infusion to keep the microbubbles from sedimentation. When bubble concentration in the field of view appeared to stabilize (after 1min of infusion), the image acquisition started. This infusion rate was selected, based on a pre-study, to establish a bubble concentration low enough to facilitate the detection and tracking of individual bubbles while still maintaining a sufficient number for fully mapping the vascular structures. Ideal concentrations varied between 100 to 150 bubbles per image. For each ICP level, the CEUS cine clips were acquired for 120s, each consisting of 5760 images. The grayscale tissue images were generated simultaneously while acquiring the CEUS images and used for correcting motion artifacts. Specifically, an affine transformation was used for matching the grayscale images in each series with the first one, and for repositioning the CEUS images accordingly. To keep the bubbles fresh, a new vial of Lumason was used per ICP level.

2.2.2. CEUS imaging using ultrafast ultrasound scanners

This dissertation performed CEUS imaging for ocular blood flows using a research-based ultrafast ultrasound scanner Verasonics Vantage 256 (Verasonics, WA, USA) equipped with a Verasonics L11-4v linear array transducer (7MHz) and a GE M5Sc-D phased array transducer (2.8MHz). The transducers were programmed to transmit and receive plane-wave ultrasound in 7 angles ranging from -14° to 14°. These seven echoes were coherently compounded to form one image at a rate of 400 frames per second. To minimize the relative motions between the ultrasound transducers and the animal, the piglet's head was fixed to the experimental table. To compensate for eye movement, the ocular images were acquired sequentially in eight parallel axial planes separated by 0.75mm by mounting the transducers on a 6-degree-of-freedom, programable, precision translation platform (X-LSM and X-RSW series, Zaber). The microbubbles (Lumason, Bracco Diagnostics, NJ, USA) were prepared following the product label and infused at 0.6mL/min using a veterinary syringe pump (Practivet, AZ, USA) connected to the femoral vein line. The infusion rate was selected, based on a pre-study, to establish a preferred bubble concentration low enough to facilitate the detection and tracking of individual bubbles while still maintaining a sufficient number for fully mapping the vascular structures. For each ICP level, the bubble infusion was started 5min after the ICP reached the desired level and stabilized. Image acquisition started once the bubble reached a steady concentration in the field of view, typically 75s after the infusion was started, and ended at 150s.

It should be noted that while the clinical scanners displayed CEUS images directly, special image processing was needed for the Verasonics scanner to obtain the bubble images. Specifically, the raw data were processed offline using an in-house code based on MATLAB R2021b, which filtered out spatio-temporal stagnant patterns generated by the surrounding tissues. Here we used a Singular Value Decomposition (SVD) based clutter filtering technique (Demené et al. 2015), followed by the removal of a sufficient number of low-order modes needed for filtering out the tissue signals. For the current data, the number of removed modes typically varied between 10 to 15.

2.3. CEUS image enhancement

2.3.1. Blind deconvolution

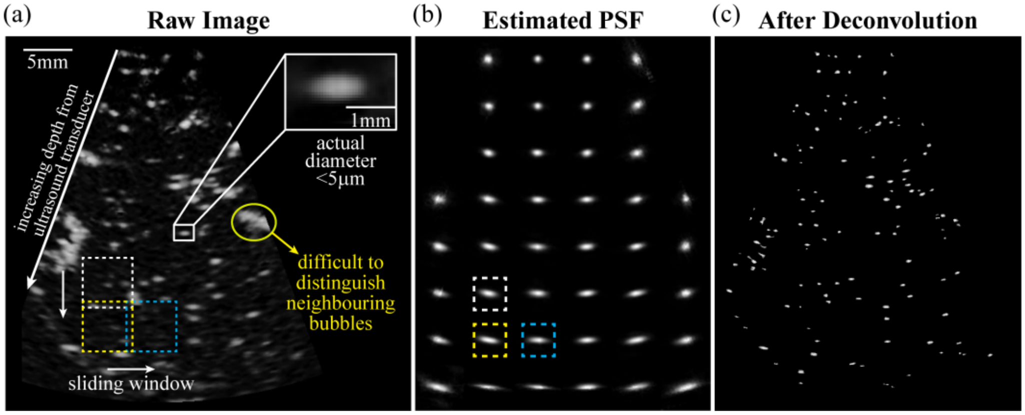
(a)
Raw Image
(b)
Estimated PSF
(c)
After Deconvolution
5mm
increasing depth from ultrasound transducer
1mm
actual diameter <5µm
difficult to distinguish neighbouring bubbles
sliding window

Figure 2-1 Illustration of the problems in raw CEUS images and sample results of blind deconvolution. (a) A sample raw CEUS image of a porcine's coronal brain section. A bubble trace (white box) is magnified at the top right to show its millimetric scale, which is much larger than its physical size (~5µm). A group of closely seated bubbles is marked in the yellow circle showing the difficulty in distinguishing them. The dashed boxes are the moving interrogation windows used for estimating the local PSF. (b) The corresponding estimated spatial distribution of PSF. Highlighted in the white, yellow, and blue dashed boxes are the PSFs corresponding to the same windows in (a). (c) A sample enhanced image after blind deconvolution.

Figure 2-1 is a sample CEUS image of the coronal brain section recorded using the Siemens scanner. As highlighted in the white box, the typical Full Width at Half Maximum (FWHM) of a bubble trace is in the order of hundreds of microns, much larger than the physical size of the contrast agent (~5µm). Consequently, closely located bubbles cannot be easily distinguished, as demonstrated in the yellow encircled area. Exacerbating the analysis is the tendency of the bubble trace to become increasingly elongated with increasing depth in the direction perpendicular to the scanline.

Yet, obtaining precise localization for closely seated bubbles is vital for the subsequent quantitative analysis, e.g., the reconstruction and flow measurement of neighboring micro blood vessels that are separated by tens of microns. Since the bubble is an order of magnitude smaller than the pixel size of the imaging system, the CEUS image has been modeled as distributed point scatters blurred by spatially varying point spread functions (PSFs) with added noise (Szabo 2004; Christensen-Jeffries et al. 2014; Zhang et al. 2020). This model can be expressed as:

$$\boldsymbol{y} = \boldsymbol{k} \otimes \boldsymbol{x} + \boldsymbol{n} \tag{2.1}$$

where $\boldsymbol{y}$ is the raw CEUS image, $\boldsymbol{k}$ is the 2D point spread function, $\boldsymbol{x}$ is the distribution of point scatters with values of one being bubble centers and zero otherwise, $\otimes$ denotes the convolution operator, and $\boldsymbol{n}$ is the noise matrix. To determine the spatially varying $\boldsymbol{x}$ and $\boldsymbol{k}$, one can minimize the cost function $\mathcal{L}_{\boldsymbol{BD}}$ defined as:

$$\mathcal{L}_{\boldsymbol{BD}} = \left\|\boldsymbol{x} \otimes \boldsymbol{k} - \boldsymbol{y}\right\|_2^2 + \gamma\left\|\boldsymbol{k}\right\|_2^2 + \lambda_1\left\|\boldsymbol{x}\right\|_0 + \lambda_2\left\|\nabla\boldsymbol{x}\right\|_0 \tag{2.2}$$

in small sub-areas of the raw image, where the PSF variations in it can be ignored. The last three terms on the right side are regularization terms, where $\left\|\boldsymbol{p}\right\|_0 = \sum\left|p_{ij}\right|^0$ and $\left\|\boldsymbol{p}\right\|_2 = \left(\sum\left|p_{ij}\right|^2\right)^{1/2}$ are the L_0 and L_2 norms, and γ, λ_1, and λ_2 are assigned weights, whose values are selected empirically based on previous studies (Pan et al. 2017). The use of two L_0 norms is designed to ensure that the resulted $\boldsymbol{x}$ contains a minimal number of non-zero values and gradients, i.e., it is reduced to distributed point scatters. The algorithms for solving this minimization problem can be found in Pan et al. (2017). In this work, the $\mathcal{L}_{\boldsymbol{BD}}$ is solved within interrogation windows of 80×80 pixels with a 10% overlap between neighbors sliding across the raw image (dashed squares in Figure 2-1a) to obtain the spatial distribution of the PSF (Figure 2-1b). Owing to the nonuniform bubble distribution, the PSF at each location is estimated by averaging the results obtained from 20 randomly selected images. Deconvolving the raw image with these PSFs (Whyte et al. 2014) at the corresponding locations, subtracting the non-uniform background calculated by averaging 15 consecutive images, and subsequently enhancing it using modified histogram equalization (Sampath et al. 2018) provides the underlying point scatters (Figure 2-1c). Such deconvolution-based image enhancement has also been used in other studies (Foroozan et al. 2018; Heiles et al. 2019). The current blind deconvolution code is scripted in MATLAB 2021b (MathWorks, MA, USA) and executed parallelly on a six-core intel i7-8700K CPU. It takes about 54.9 minutes to process 7000 200×360 pixels CEUS images. One of the shortcomings of this approach, as evaluated later, is that it is capable of distinguishing between closely spaced bubbles only when they are separated by more than one FWHM of the local PSF. For detecting micro-blood vessels, this limitation has motivated the development of machine learning-based techniques.

2.3.2. Generation of synthetic images for training and evaluating neural networks

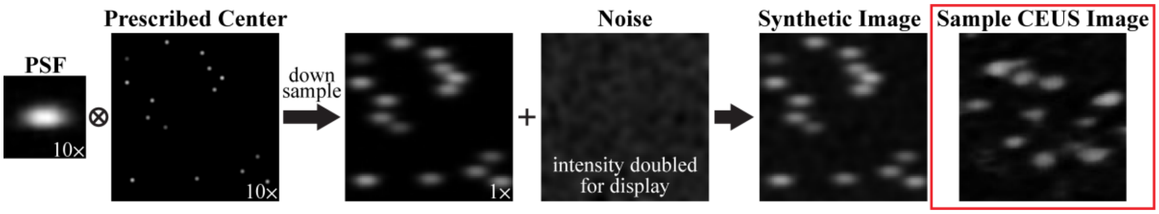

Figure 2-2 The procedure for generating the synthetic images. The prescribed centers with various peak intensities are generated at 10 times the original image resolution and are convolved with a PSF interpolated to the same scale. The resulting image is down-sampled to the native image resolution and combined with the background noise with realistic intensity distribution. The subarea of a CEUS image containing a similar PSF is demonstrated next to the synthetic data.

The training and validation of the neural networks as well as the evaluation of different methods are conducted based on realistic synthetic images. This approach allows us to enhance the generalizability of the supervised networks for varying noise levels, bubble densities, and PSF morphologies with the exact knowledge of the locations of bubble centers. Following Eqn. (2.1), the synthetic input training data are generated as a convolution of randomly distributed points ($\boldsymbol{x}$) with the local PSF ($\boldsymbol{k}$) along with added noise. As demonstrated in Figure 2-2, $\boldsymbol{x}$ is generated on a high-resolution map in which the pixel size is one-tenth of that of the native CEUS image, i.e., it is comparable to the diameter of the contrast agent. The typical bubble density in the CEUS images is about 0.5mm^{-2}, hence the synthetic bubble densities involved in the training vary between 0.1 to 1.0mm^{-2}. Since all images in this study are stored as the Single data type, i.e., the intensity varies from 0 to 1, each synthetic bubble center is assigned a random peak intensity in the 0.6 to 1.0 range to simulate the uneven bubble intensities in the actual CEUS images. The intensity distribution of $\boldsymbol{k}$ originates from the spatially varying PSFs (Figure 2-1b) obtained by blind deconvolution based on fifteen different experimental datasets. These PSFs are further randomly rotated in the -20° to +20° range and resized using a factor ranging between 0.8 to 2. As illustrated in Figure 2-2, $\boldsymbol{k}$ is also up-sampled to ten times the native image resolution using bicubic interpolation and then convolved with $\boldsymbol{x}$. The resulting image is subsequently down-sampled to the native image resolution using bicubic interpolation, forming an 80×80 pixels synthetic image, whose size would be 4.8×4.8mm^2. To evaluate the effects of up- and down-sampling on the intensity distributions of the PSFs, we up- and down-sample 228 PSFs to obtain $\hat{\boldsymbol{k}}$ and measure the Root-Mean-Square (RMS) of the difference between the original ($\boldsymbol{k}$) and processed ($\hat{\boldsymbol{k}}$) data. Figure 2-3 is the probability density function (PDF) of the relative RMS error, i.e.,

$$\varepsilon_k = RMS\left(\hat{\boldsymbol{k}} - \boldsymbol{k}\right) \Big/ RMS\left(\boldsymbol{k}\right) \tag{2.3}$$

As is evident, the mode is about 1.2%, confirming that resizing of $\boldsymbol{k}$ does not introduce significant errors. The noise is modeled as low-intensity random speckles that are subsequently blurred by a 2D gaussian filter. The PDFs of the noise intensity are obtained by sampling the background in the raw CEUS images and rounding their peak levels to 0.10, 0.15 (most commonly seen), and 0.20. In addition, we also generate a noisier artificial distribution by stretching the most intense PDF to 0.25. The example of noise and the final noisy synthetic image is shown in Figure 2-2. For reference, we also provide a sample original CEUS image with a similar PSF, showing that the synthetic data has similar characteristics.

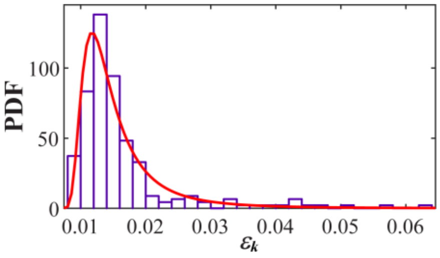

Figure 2-3 The PDF of the relative RMS intensity difference (ε_k) between the original PSFs and the up-and-down-sampled ones.

To generate the training references for the U-net and SupBD-net, bubble center maps established at 10 times the native image resolution have been downsized to one and three times the native resolution, respectively. After down-sampling, the pixels containing the true centers (but reduced resolution) are prescribed values of 1, while others are set as 0. To improve training stability, the low-resolution center maps are blurred by a 5×5 2D gaussian kernel, as recommended by Nehme et al. (2018). In total, 250,000 input and reference image pairs have been created for the training and validation of supervised learning methods.

The same approach, but with modified PSFs, is used for generating the evaluation data for the SelfBD-net. They are based on five increasingly elongated PSFs along the scanline of the CEUS data not included in the previous training datasets, which are further rotated by 90° to make them substantially different than any of the ones used for training and validation. For each PSF, 2500 image pairs with a bubble concentration of 0.5mm^{-2} and a peak noise level of 0.16 have been generated without random resizing of the PSF. Moreover, synthetic images based on a particular PSF with an aspect ratio of 1.81 are generated to evaluate the effect of peak noise levels ranging from 0 to 0.24, whose PDFs are based on the CEUS data with a peak noise intensity of 0.15, and the effect of bubble concentration ranging from 0.25 to 1mm^{-2}.

In addition, two sets of data are generated for comparing the performance of different image processing methods. For evaluating the accuracy in detecting the bubble centers, the synthetic data involve 3 bubble concentrations, namely 0.25, 0.5, and 1mm^{-2}, corresponding to the typically observed low, normal, and dense bubble distributions. The 5 increasingly elongated PSFs along the scanline are based on experimental datasets that are not included in the training sets, without additional random rotation and resizing. The peak noise levels are 0, 0.08, 0.16, and 0.24, and their PDFs are based on the CEUS data with a peak noise intensity of 0.15. A total of 2500 synthetic image pairs are generated for each bubble density, PSF, and noise level. For evaluating the ability to distinguish between closely located microvessels, the synthetic bubbles are translated over 2500 time steps along two parallel lines separated by 30, 60, 120, 180, 240, 300, and 360μm at a typical mean microvascular velocity magnitude of 5mm/s. These lines are orientated either horizontally or vertically. New bubbles are generated based on the actual time history of microbubbles passing through a cross-section of a microvessel, where values from different microvessels are assigned to each line. The PSFs are similar to those described above and the noise profile follows the CEUS data with a peak noise intensity of 0.15.

2.3.3. U-net for blind deconvolution

As part of our initial approach and as a baseline for comparing the different machine learning techniques, a U-net has been trained for extracting the bubble centers from raw CEUS images. The coding, training, and validation have been performed using the Deep Learning Toolbox in MATLAB 2021b. Following the conventional network structure (Ronneberger et al. 2015), as sketched in Figure 2-4, raw CEUS images are divided into 80×80 pieces and are processed using 3 encoding steps to convert the input information into features. For each encoder layer, the incoming information is processed by the conventional convolutional network architecture, ConvBlock, which, as illustrated on the top right of Figure 2-4, consists of two successive 3×3 2D convolution layers, each followed by a Rectified Linear Unit (ReLU) layer. The output of the ConvBlock is downsized by half using a 2×2 max pooling layer and passed on to the next ConvBlock, where the feature channels are doubled. The output of the encoding layers to the bridging level is 10×10 pixels images along with 256 feature channels. In the bridging level, after another ConvBlock, the number of features is doubled. In the next step, a Dropout layer is used to randomly drop 20% of the features during each training iteration to prevent overfitting (Ronneberger et al. 2015). Subsequently, the information undergoes 3 levels of decoding to project the features back onto the pixel space. In each layer, the incoming information is upsized by two along each spatial dimension using the UpConv block, which consists of a transposed convolution layer followed by a ReLU layer, as illustrated in the bottom right of Figure 2-4. The upsized data are concatenated with the output of the encoder block at the same scale and processed by another ConvBlock, where the feature channels are reduced to half of that of the previous decoding layer. Finally, the information generated through the encoding-decoding path is condensed into a single image by a 3×3 convolution layer as the output of the U-net.

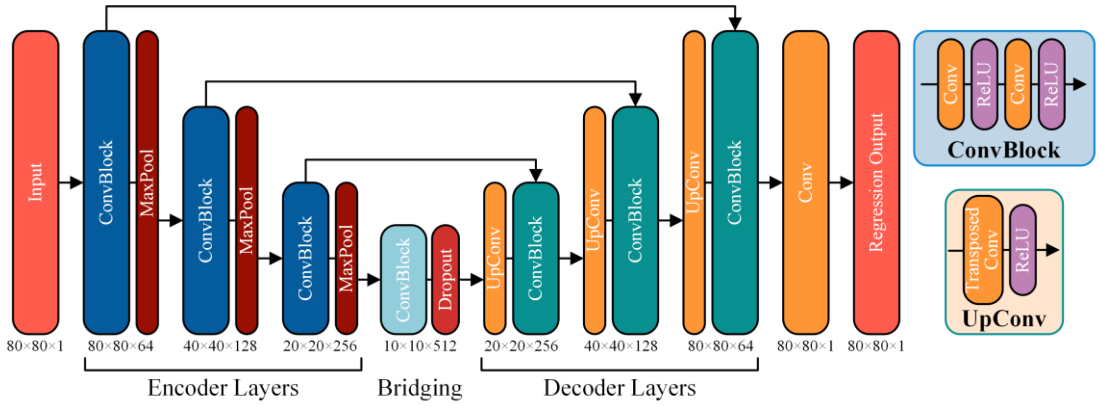
Input
ConvBlock
MaxPool
ConvBlock
MaxPool
ConvBlock
MaxPool
ConvBlock
Dropout
UpConv
ConvBlock
UpConv
ConvBlock
UpConv
ConvBlock
Conv
Regression Output
80×80×1
80×80×64
40×40×128
20×20×256
10×10×512
20×20×256
40×40×128
80×80×64
80×80×1
80×80×1
Encoder Layers
Bridging
Decoder Layers
Conv
ReLU
Conv
ReLU
ConvBlock
Transposed Conv
ReLU
UpConv

Figure 2-4 An illustration of the network structure of U-net. The current U-net consists of 3 encoder levels, a bridging level, and 3 decoder levels. In each encoding step, the input information is processed by a convolution block (ConvBlock, detail shown in top right), consisting of two successive 3×3 2D convolution layers, each followed by a Rectified Linear Unit (ReLU) layer. The output of the ConvBlock is downsized by half using a 2×2 max pooling layer and passed on to the next ConvBlock where the feature channels are doubled. A dropout layer, which randomly drops 20% of the input features, is used after the bridging step to prevent overfitting. Subsequently, the incoming information is upsized by 2 in decoding steps using a transposed convolution followed by ReLU (UpConv, detail shown in bottom right), concatenated with the output of the encoding layers at the same level, and processed by the ConvBlock. For each decoder layer, the feature channels are reduced by half. Finally, a convolution layer is used for generating the 2D image outputs. The output size of each step is marked as image size × number of feature channels below each block.

The training is based on 250,000 pairs of synthetic images out of which 70% are used for training and the rest as the validation set. During each training iteration, a minibatch of 24 randomly selected images is processed in the forward path to estimate the corresponding maps of bubble centers $\tilde{\boldsymbol{x}}$. They are then compared to the training references $\boldsymbol{x}$ to calculate the squared-error loss, namely $\mathcal{L}_{U\text{-}net} = \|\tilde{\boldsymbol{x}} - \boldsymbol{x}\|_2^2$. The gradients of $\mathcal{L}_{U\text{-}net}$ with respect to the network parameters are backpropagated to update the current network using the gradient decent optimizer Adam (Kingma and Ba 2014). For each epoch, the entire training dataset is randomly shuffled to bypass local optima, and at the end of each epoch, the result is validated. The learning rate is initialized as 0.001 and is subsequently reduced by 10 for every 5 epochs (Shin et al. 2016). The training ends when the validation loss stops decreasing over the next 5 epochs. The parameters of the trained network for the last five epochs are stored, and the network parameters giving the minimum validation loss are selected as the final result. The training is carried out on a desktop PC, equipped with an NVIDIA 1080Ti GPU, 1 Intel i7-8700K CPU, and 64 GB DDR4 RAM. The training takes 28 hours. Once trained, it only takes about 4.4 minutes for U-net to process 7000 200×360 pixels CEUS images.

2.3.4. Super-resolution neural network for blind deconvolution (SupBD-net)

As described in the introduction, we utilize a residual learning-based SupBD-net to achieve higher sub-pixel accuracy in localizing the bubble centers. The network structure mainly follows the previously developed super-resolution method SRResNet (Ledig et al. 2017), but with some modifications tailored to the current application. Specifically, as illustrated in Figure 2-5, the input raw CEUS images pass two convolution blocks for preprocessing and extracting shallow layer features. The components of each convolution block are illustrated in the bottom left box of Figure 2-5. Different from the typical elements in U-net, the ConvBlocks in SupBD-net consist of a 2D convolution layer followed by an Instance Normalization (IN) layer (Ulyanov et al. 2016) and a Leaky Rectified Linear Unit layer (LeakyReLU). There are two reasons for this modification. First, IN has been proven to be favorable for single-image enhancement problems (Vu et al. 2018) by normalizing the mean value and covariance of each image in a minibatch. This step prevents the effects of instance-specific mean and covariance shift caused by variations in image intensity and noise level of a specific training set, hence enabling the network to focus on learning the common features of the trace-to-center conversion for every image. Second, the LeakyReLU layer performs a threshold operation, where any negative input is multiplied by a fixed scalar, selected as 0.2, following Radford et al. (2015), to prevent the assignment of zero gradients to negative values in ReLU. Subsequently, four residual blocks (ResBlock) are used for local residual learning, and the output is added to that of the second ConvBlock for global residual learning. Such a local-global residual learning scheme is adopted from a previous study of image super-resolution (Lim et al. 2017a). The number of local ResBlocks is selected based on a preliminary test, showing that four blocks achieve a good balance between localization accuracy and processing speed. The components of the ResBlock are sketched in the bottom right of Figure 2-5. It has been modified from the typical residual block by replacing the batch normalization with IN and ReLU with LeakyReLU for the same reasons as previous steps. The features extracted by the local-global residual learning are up-sampled by a transposed convolution layer, which triples the spatial resolution. After another IN and LeakyReLU, a 2D convolution layer generates the high resolution images. Finally, a sigmoid layer scales the data to ensure a 0 to 1 intensity range. It should be noted that, adopting the values used in SRResNet (Ledig et al. 2017), the convolution kernel size is 9×9 for the first and last 2D convolution layers, and 3×3 for the others. The image size and the number of feature channels after each step in SupBD-net is listed above the corresponding block in Figure 2-5.

The training dataset, training methods, and the selection of training parameters of SupBD-net are almost the same as those of U-net, but with two differences. First, while the training input is at the native image resolution, the training references, i.e., the true centers, are at a spatial resolution that is 3 times finer than that of the input CEUS images. Second, the minibatch size is reduced to 16 due to the limitations of the GPU memory. The training takes 116 hours. For a trained SupBD-net, it takes 27.5 minutes to process 7000 200×360 pixels CEUS images.

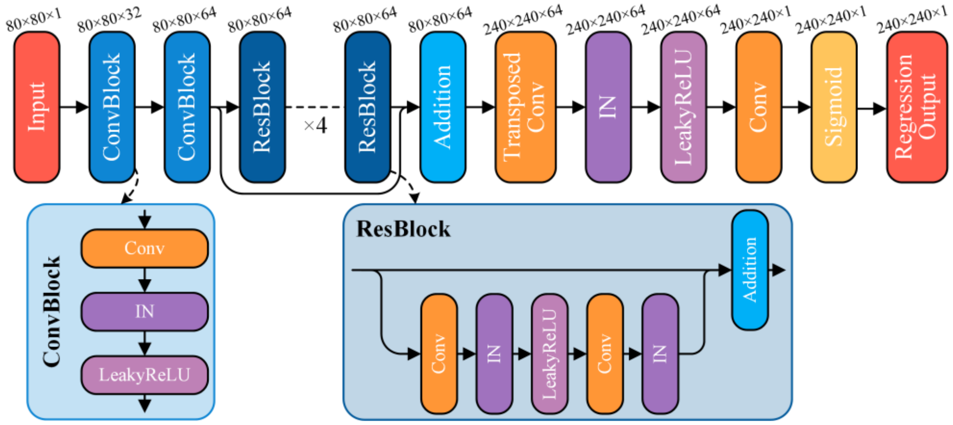
80×80×1
80×80×32
80×80×64
80×80×64
80×80×64
80×80×64
240×240×64
240×240×64
240×240×64
240×240×1
240×240×1
240×240×1
Input
ConvBlock
ConvBlock
ResBlock
×4
ResBlock
Addition
Transposed Conv
IN
LeakyReLU
Conv
Sigmoid
Regression Output
ConvBlock
Conv
IN
LeakyReLU
ResBlock
Addition
Conv
IN
LeakyReLU
Conv
IN

Figure 2-5 An illustration of the network structure of SupBD-net. The current SupBD-net consists of two ConvBlocks for extracting lower-level features of the CEUS image, four local residual blocks (ResBlock) along with one global residual block for higher-level feature extraction, one transpose convolution layer for upscaling, one final convolution layer for converting higher dimensional features into 2D images, and a sigmoid layer to ensure a 0-1 intensity range of the output image. The image size × number of feature channels are listed above each block. The bottom left shows the components of ConvBlock in SupBD-net, including a 2D convolution layer followed by an Instance Normalization (IN) layer and a Leaky Rectified Linear Unit (LeakyReLU) layer. The bottom right shows the components of the residual blocks, input information is processed by a 2D convolution layer followed by IN, LeakyReLU, another 2D convolution, and IN. The output of the last IN is added to the input of the whole ResBlock and passed on to the following layers.

2.3.5. Self-supervised neural network for blind deconvolution (SelfBD-net)

As explained in the introduction, our objective in developing SelfBD-net is to establish an approach that is not limited to the scope of the training dataset, which can be generalized and applied to other datasets that have substantially different PSFs and noise levels. Such a need is particularly important for CEUS images, where the bubble trace characteristics and noise levels vary with the ultrasound wavelength, beamforming mechanism, transducer design, built-in post-processing algorithm, and organ being imaged. The proposed SelfBD-net is derived from the conventional blind deconvolution method, where instead of optimizing ***x*** and ***k*** simultaneously in Eqn. (2.2), their cost functions are separated as follows:

$$\mathcal{L}_{\boldsymbol{x},\,\boldsymbol{BD}} = \underbrace{\left\|\boldsymbol{x} \otimes \boldsymbol{k} - \boldsymbol{y}\right\|_2^2}_{\mathcal{L}_{\boldsymbol{y},\,\boldsymbol{BD}}} + \underbrace{\lambda_1 \left\|\boldsymbol{x}\right\|_0 + \lambda_2 \left\|\nabla \boldsymbol{x}\right\|_0}_{\mathcal{R}_{\boldsymbol{x},\,\boldsymbol{BD}}} \tag{2.4}$$

$$\mathcal{L}_{\boldsymbol{k},\,\boldsymbol{BD}} = \underbrace{\left\|\boldsymbol{x} \otimes \boldsymbol{k} - \boldsymbol{y}\right\|_2^2}_{\mathcal{L}_{\boldsymbol{y},\,\boldsymbol{BD}}} + \underset{\mathcal{R}_{\boldsymbol{k},\,\boldsymbol{BD}}}{\gamma \left\|\boldsymbol{k}\right\|_2^2} \tag{2.5}$$

In blind deconvolution, these equations are solved alternatively and iteratively for estimating and updating the PSF and true centers. This section introduces a self-supervised learning method that solves these optimization problems using neural networks. As illustrated in Figure 2-6, in SelfBD-net, a new network, denoted as k-net, is added for estimating the PSF, in addition to the center estimation network, which is denoted as x-net. The structure of the k-net follows the same logic as that of the SupBD-net, except that there are only 3 local residual blocks, and there are no upsizing steps. Also, after testing different sizes for the convolution kernels, we have selected a 7×7 kernel as a compromise between computation time and data quality. The currently selected x-net is the pretrained SupBD-net in order to take advantage of some of its learned center features, yet it is not limited to this selection.

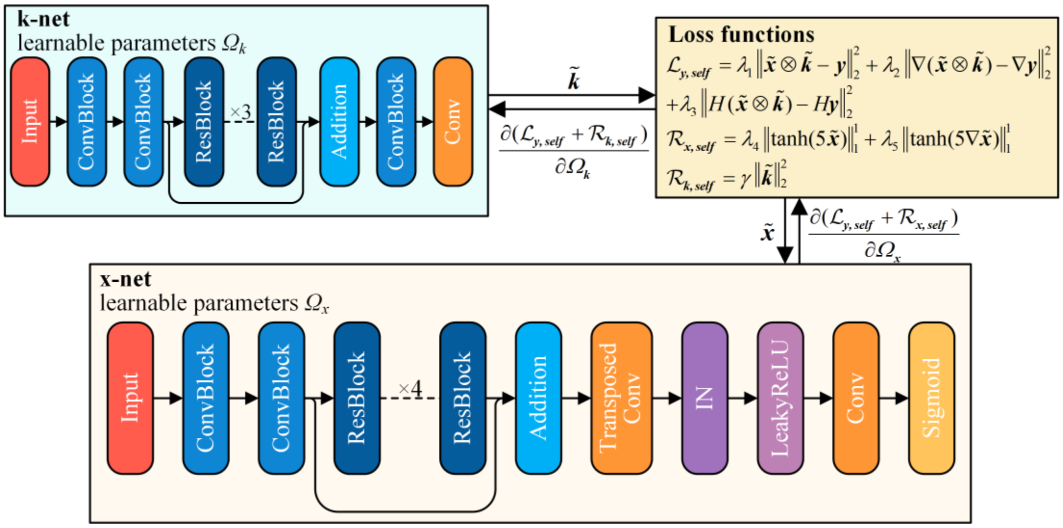
k-net
learnable parameters Ω_k
Input
ConvBlock
ConvBlock
ResBlock
×3
ResBlock
Addition
ConvBlock
Conv
$\tilde{k}$
$\frac{\partial(\mathcal{L}_{y,self}+\mathcal{R}_{k,self})}{\partial\Omega_k}$
Loss functions
$\mathcal{L}_{y,self}=\lambda_1\|\tilde{x}\otimes\tilde{k}-y\|_2^2+\lambda_2\|\nabla(\tilde{x}\otimes\tilde{k})-\nabla y\|_2^2$
$+\lambda_3\|H(\tilde{x}\otimes\tilde{k})-Hy\|_2^2$
$\mathcal{R}_{x,self}=\lambda_4\|\tanh(5\tilde{x})\|_1^1+\lambda_5\|\tanh(5\nabla\tilde{x})\|_1^1$
$\mathcal{R}_{k,self}=\gamma\|\tilde{k}\|_2^2$
$\tilde{x}$
$\frac{\partial(\mathcal{L}_{y,self}+\mathcal{R}_{x,self})}{\partial\Omega_x}$
x-net
learnable parameters Ω_x
Input
ConvBlock
ConvBlock
ResBlock
×4
ResBlock
Addition
Transposed Conv
IN
LeakyReLU
Conv
Sigmoid

Figure 2-6 An illustration of the network structure of SelfBD-net. Shown in the top left is an additional network, named k-net, used for estimating the PSF from the raw CEUS image. The k-net shares the same preprocessing and local-global residual blocks as SupBD-net, followed by another ConvBlock and a final convolution layer for generating outputs. Here, all the convolution kernels in k-net are 7×7. The k-net and the pretrained x-net are jointly trained on the CEUS images with unknown PSFs using the loss functions provided in the top right. Here, the x-net is selected as SupBD-net, but it can be other pretrained networks for identifying the bubble centers.

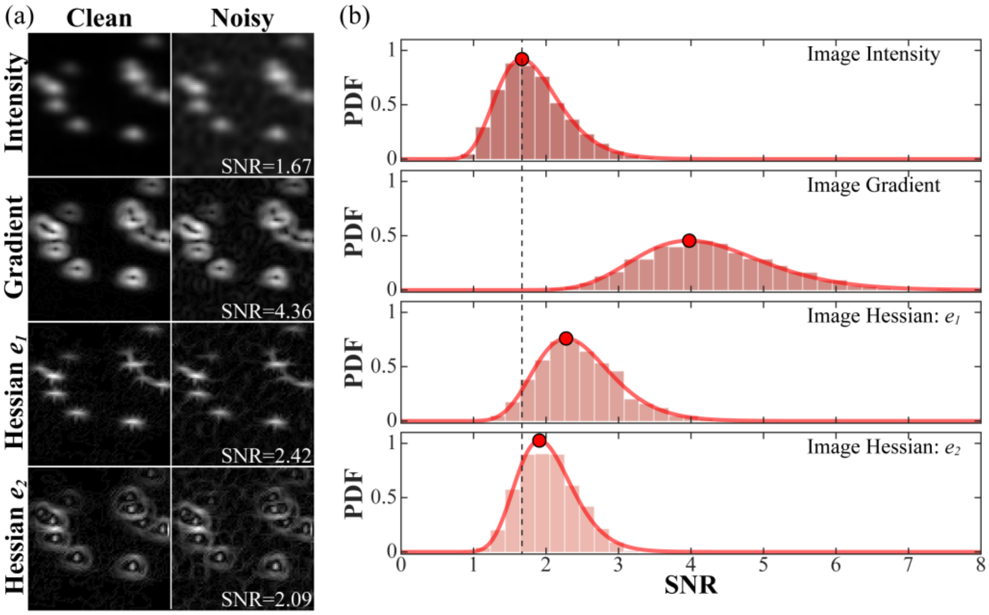

Figure 2-7 Comparison of the signal-to-noise ratio (SNR) for image intensity, gradient, and hessian. (a) A sample comparison of a clean synthetic CEUS image (left) versus the same one with added noise at a typical level (right). From top to bottom, demonstrated images are image intensity, gradient magnitude, and the magnitudes of the first and second eigenvalues of image hessian. The corresponding SNR for the noisy image is listed in the bottom right of each image. (b) The SNR PDF for 2500 noisy synthetic CEUS images with a typical bubble density and noise level. The dashed line shows the center SNR level for image intensity, and the red dots show the center SNR level for each value.

The SelfBD-net is trained by solving cost functions that are based on Eqns. (2.4) and (2.5), but with some modifications aimed at making them more suitable for the deep learning frameworks and at improving the results. As a starting point, the original loss term with the CEUS image $\boldsymbol{y}$, i.e., $\mathcal{L}_{y,BD} = \|\boldsymbol{x} \otimes \boldsymbol{k} - \boldsymbol{y}\|_2^2$, is expanded to

$$\mathcal{L}_{y,self} = \lambda_1 \|\tilde{\boldsymbol{x}} \otimes \tilde{\boldsymbol{k}} - \boldsymbol{y}\|_2^2 + \lambda_2 \|\nabla(\tilde{\boldsymbol{x}} \otimes \tilde{\boldsymbol{k}}) - \nabla \boldsymbol{y}\|_2^2 + \lambda_3 \|H(\tilde{\boldsymbol{x}} \otimes \tilde{\boldsymbol{k}}) - H\boldsymbol{y}\|_2^2 \tag{2.6}$$

by adding an L_2 loss of the image gradient (∇) and hessian (H) to the L_2 loss of intensity. Here, $\tilde{\boldsymbol{x}}$ and $\tilde{\boldsymbol{k}}$ are the bubble centers and the PSFs estimated by the x-net and k-net, respectively. The weights, λ_1, λ_2, and λ_3, are selected as 1, 5, and 25 respectively, to ensure that each final loss term is of the same order of magnitude as the others. The two additional terms are introduced for the following reasons. First, the image gradient and hessian have higher Signal-to-Noise Ratios (SNR) than image intensity. For example, Figure 2-7a compares the image intensity, gradient, as well as the first (e_1) and second (e_2) eigenvalues of the hessian matrix for a noise-free and noisy synthetic CEUS image. For each row, the SNR is defined as the RMS intensity of the clean image divided by the RMS of the intensity difference between the clean and noisy images. The results, indicated on each image, show that the gradient has the highest SNR, followed by the Hessians, and then by the image intensity. A more comprehensive comparison, which leads to the same conclusion, is provided in Figure 2-7b by showing the PDFs of the SNR based on 2500 synthetic images with typical bubble densities and noise levels. Therefore, adding additional true information with higher SNR to the cost function is likely to improve the robustness of the SelfBD-net. Second, the eigenvalues of image hessian encode information about the shape and the orientation of the object in the image (Jerman et al. 2016). Hence incorporating this information into the cost function is likely to enhance the ability to obtain a PSF with the correct shape. It should be noted that, during implementation, the L_2 loss is calculated directly for each term in the hessian matrix instead of the eigenvalues, since the MATLAB deep learning toolbox cannot handle complex eigenvalues.

Next, the two L_0 terms in Eqn. (2.4) are non-convex and non-differentiable. Hence, as discussed by Wang et al. (2016), solving an L_0 regularized optimization problem is computationally intractable, an issue known as non-deterministic polynomial-time hard (Natarajan 1995). In blind deconvolution, this issue is mitigated by introducing an approximate approach, which is detailed in Xu et al. (2011). Alternatively, as a common remedy, other convex and continuous regularization terms, such as L_1 or L_2 norms, are used as a relaxation of the L_0 norm. In the present SelfBD-net, we opt to use the L_1 norms of tanh(5$\boldsymbol{x}$) as a surrogate, which converts most of the non-zero values of $\boldsymbol{x}$ to almost 1. Hence, the sum of the absolute values of each element in tanh(5$\boldsymbol{x}$) approximates the number of non-zero values in $\boldsymbol{x}$, i.e. the L_0 norm. In this way, the two regularization terms for $\boldsymbol{x}$ can be approximated as:

$$\mathcal{R}_{\boldsymbol{x},\,\boldsymbol{self}} = \lambda_4 \left\| \tanh(5\tilde{\boldsymbol{x}}) \right\|_1^1 + \lambda_5 \left\| \tanh(5\nabla\tilde{\boldsymbol{x}}) \right\|_1^1 \tag{2.7}$$

Following Pan et al. (2017), and consistent with our previous experience with blind deconvolution, both λ_4 and λ_5 are selected as 4×10^{-3}. As for the cost function for the k-net in SelfBD-net, which is equivalent to Eqn. (2.5), the regularization term in Eqn. (2.8) remains unchanged, with γ=2, also following Pan et al. (2017).

$$\mathcal{R}_{\boldsymbol{k},\,\boldsymbol{self}} = \gamma \left\| \tilde{\boldsymbol{k}} \right\|_2^2 \tag{2.8}$$

Finally, as shown in Figure 2-6, $\mathcal{L}_{\boldsymbol{k},\,\boldsymbol{self}} = \mathcal{L}_{\boldsymbol{y},\,\boldsymbol{self}} + \mathcal{R}_{\boldsymbol{k},\,\boldsymbol{self}}$ is used for training the k-net and $\mathcal{L}_{\boldsymbol{x},\,\boldsymbol{self}} = \mathcal{L}_{\boldsymbol{y},\,\boldsymbol{self}} + \mathcal{R}_{\boldsymbol{x},\,\boldsymbol{self}}$ for training the x-net.

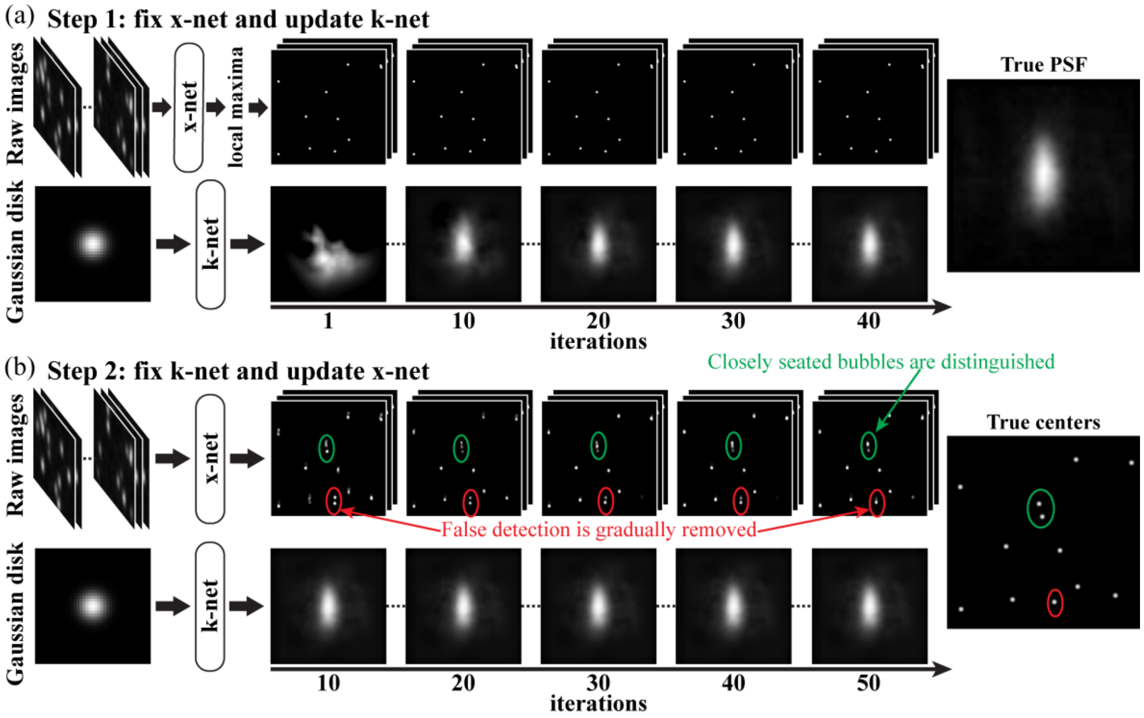
(a) Step 1: fix x-net and update k-net
Raw images
x-net
local maxima
Gaussian disk
k-net
True PSF
1
10
20
30
40
iterations
(b) Step 2: fix k-net and update x-net
Closely seated bubbles are distinguished
Raw images
x-net
True centers
False detection is gradually removed
Gaussian disk
k-net
10
20
30
40
50
iterations

Figure 2-8 The procedures for training SelfBD-net. (a) Step 1: updating the k-net while freezing the x-net. While x-net is prone to generate a cluster of false detections around the true center, the brightest one in each cluster is used for approximating the true center and for calculating the loss functions. After 40 iterations, the k-net converges and learns to deform the gaussian disk to resemble the true PSF shown on the right. (b) Step 2: freezing the k-net and updating layers after the global residual learning in x-net. The first 50 iterations are demonstrated where the false detections (red circle) in the x-net output are gradually removed and the closely seated bubbles (green circle) are separated. The resulting estimated bubble centers are close to the true centers shown on the right.

SelfBD-net is implemented in each 80×80 interrogation window as described above. The training strategy depicted in Figure 2-8 involves two steps: The first (Figure 2-8a) is aimed at obtaining an estimation for the PSF. Hence, the parameters for the pretrained x-net are not updated, while the parameters of the k-net are randomly initialized and trained to deform an input gaussian disk to the desired PSF. Since the image properties for each 80×80 interrogation window are the same, for this step, only eight randomly selected images are fed into the x-net to generate the estimated $\tilde{\boldsymbol{x}}$ needed for calculating $\mathcal{L}_{k,self}$. However, the un-updated x-net is likely to yield false detections, with a particular tendency to generate multiple bubble centers close to the true one. This issue, if left uncorrected, would lead to an underestimated PSF size and erroneous PSF intensity distribution.

Hence, from each cluster of local maxima in $\tilde{\boldsymbol{x}}$, we select the brightest peak that exceeds 0.5 as the estimated location of the bubble center. The resulting sparse distribution (top row of Figure 2-8a) is used for calculating $\mathcal{L}_{k,self}$, while the corresponding true map is presented on the right-hand side of Figure 2-8b. Note that since $\tilde{\boldsymbol{x}}$ is of a higher spatial resolution than $\tilde{\boldsymbol{k}}$ and $\boldsymbol{y}$, to calculate $\mathcal{L}_{y,self}$, the $\tilde{\boldsymbol{k}}$ is upsized to the same resolution as $\tilde{\boldsymbol{x}}$, convolved with $\tilde{\boldsymbol{x}}$, downsized to the native image resolution, and compared with $\boldsymbol{y}$. The sample training progress in Figure 2-8a demonstrates the evolution of the estimated PSF in steps of ten iterations. The Adam optimizer is used for updating the k-net. The initial learning rate is 0.0001, and it is reduced by a factor of 10 when $\mathcal{L}_{k,self}$ does not decrease for the next five iterations. The training is terminated when the RMS intensity difference in $\tilde{\boldsymbol{k}}$ between the current and the previous iteration is smaller than 1×10^{-6}. The sample in Figure 2-8a demonstrates that the k-net is able to gradually deform the input gaussian disk to a shape that resembles the true PSF, which is shown on the right. For this particular example, the k-net output converges after about 40 iterations, which takes less than 19s.

The next step, which is illustrated in Figure 2-8b, is to fix the k-net and refine the x-net. For each 80×80 interrogation window, eight randomly selected images are used for the validation, and the rest are used for training. For each iteration, a minibatch of 8 random images is fed into the x-net and the resulting $\tilde{\boldsymbol{x}}$ is used for calculating $\mathcal{L}_{x,self}$. Here, while the parameters of k-net are not updated, following typical procedures for transfer learning, parameters for layers after the global residual block of the x-net are updated. The initial learning rate for x-net is 0.0001. For every 5 iterations, x-net is validated, and the learning rate is reduced by a factor of 10 when $\mathcal{L}_{x,self}$ does not decrease for the next 5 validations. The reduction is repeated 3 times, and the network parameters yielding the least $\mathcal{L}_{x,self}$ over the past 5 validations are selected as the final result. The first 50 iterations in this training procedure are demonstrated in Figure 2-8b. Initially, the x-net generates a bubble center map containing two or more false detections in the vicinity of each true bubble center. As the training goes on, the falsely detected items, e.g. those encircled in red, are gradually removed, and the green-encircled traces are eventually reduced to a pair of closely located bubbles. This refinement process typically takes about 230s, and the resulting center map is very close to that of the true centers. Moreover, the updated parameters for the x-net of one interrogation window can be used for initializing those of its neighbors. Hence, the refinement durations for other windows can be reduced to around 90s. Once the SelfBD-net is trained for a new CEUS system, it takes 32.7 minutes to process 7000 200×360 pixels CEUS images.

2.4. Optimized echo-PIV

Based on the CEUS images enhanced by the methods described above, we perform the optimized echo-PIV/PTV, as described by Sampath et al. (2018), for the measurement of cardiovascular flows. This method repeats the cross-correlation-based PIV analysis for multiple image enhancement and PIV parameter combinations. Then, out of all the possible results, the optimum velocity is selected by iteratively eliminating outliers, i.e. by iteratively setting and updating the thresholds for the deviation of the magnitude and orientation of each velocity vector from those of its neighbors in space and time. The PIV results are used to guide the tracking of individual bubble traces (PTV) along with other constraints, including deviation from expected locations, bubble morphology, and velocity continuity. Then, singular value decomposition (Sheng et al. 2008) is used for interpolating the PTV data onto a cartesian grid and integrating it with the PIV results.

2.5. Echo-PTV and ultrasound localization microscopy (ULM)

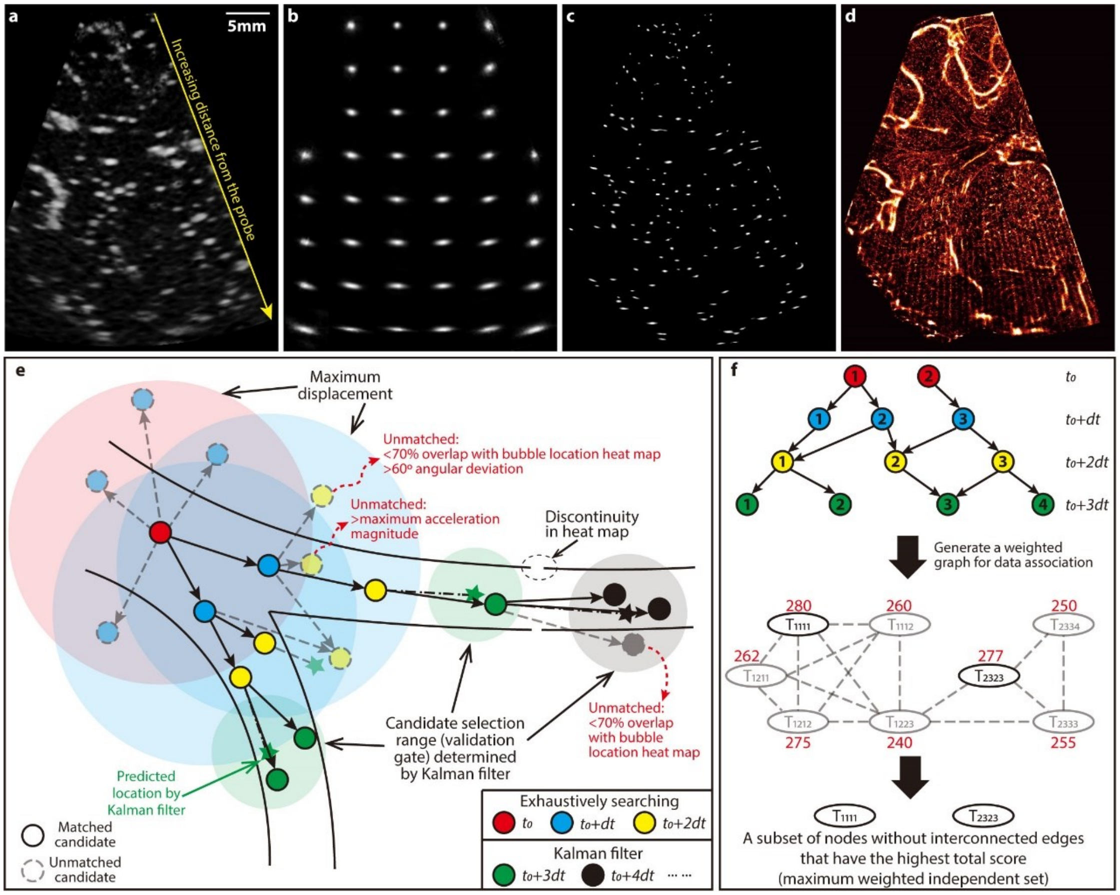
a
5mm
Increasing distance from the probe
b
c
d
e
Maximum displacement
Unmatched: <70% overlap with bubble location heat map >60° angular deviation
Unmatched: >maximum acceleration magnitude
Discontinuity in heat map
Candidate selection range (validation gate) determined by Kalman filter
Unmatched: <70% overlap with bubble location heat map
Predicted location by Kalman filter
Matched candidate
Unmatched candidate
Exhaustively searching
t_0
t_0+dt
t_0+2dt
Kalman filter
t_0+3dt
t_0+4dt ......
f
1
2
1
2
3
1
2
3
1
2
3
4
t_0
t_0+dt
t_0+2dt
t_0+3dt
Generate a weighted graph for data association
280
T_{1111}
260
T_{1112}
250
T_{2334}
262
T_{1211}
277
T_{2323}
T_{1212}
275
T_{1223}
240
T_{2333}
255
T_{1111}
T_{2323}
A subset of nodes without interconnected edges that have the highest total score (maximum weighted independent set)

Figure 2-9 Image preprocessing and bubble tracking procedures. (a) A sample raw CEUS image. (b) The spatial distribution of the point spread function estimated by blind deconvolution. (c) The enhanced image after deconvolution and modified histogram equalization. (d) A heatmap of the centers of all the detected bubbles. (e) The bubble tracking process highlighting several strategies used for detecting likely trajectories. Exposures are color coded as indicated in the legend. (f) Illustrations of strategies for data association to determine the optimal non-overlapping trajectories.

For microvascular flows, this dissertation utilizes microbubble trajectories to reconstruct microvascular structures and measure blood flow at a spatial resolution of 20μm. In the ultrasound community, this method is referred to as Ultrasound Localization Microscopy (ULM). Here, echo-PTV is conducted for hundreds of bubbles that are moving along blood vessels in various directions with different flow speeds. Moreover, there is no PIV reference to guide the tracking in this scenario. Hence, in this section, a new globally optimized method based on the Kalman filter is proposed.

Assuming that bubbles only travel within blood vessels, heatmaps of bubble centers (Figure 2-9d), obtained based on the enhanced CEUS images (Figure 2-9a-c), could be used as guidance for likely vessel locations. Hence, overlap with this heatmap is one of the criteria for detecting bubble trajectories. As illustrated in Figure 2-9d, tracking of a newly detected bubble at time t_0 (red circles) is initiated by searching for all the candidates displaced by less than a prescribed maximum distance in the following frame (blue), and then repeated to identify all possible matches in the 3rd frame (yellow). A series of criteria are used for removing unlikely candidates, including a minimum overlap with the vascular map (20% for speeds <1cm/s, 70% for speeds <5cm/s, and 90% for higher speeds), as well as maximum variations in the bubble perimeter (50%), area (50%), flow direction (60°), and velocity magnitude (one-third of the maximum prescribed distance). The overlap threshold is selected by examining numerous tracks and other thresholds are based on prior experience (Sampath et al. 2018). The remaining combinations of three exposures are considered possible trajectories. For each track, a Kalman filter is utilized to predict the state (i.e., location and morphology) of bubbles in the fourth frame (stars in Figure 2-9e). This filter is widely used for object tracking (Kim et al. 2015), including ULM (Ackermann and Schmitz 2016b; Solomon et al. 2019; Tang et al. 2020). Its prediction incorporates information of initially predicted states, correction using matched candidates falling within the uncertainty threshold, and measurement covariances. The uncertainty range is based on the Mahalanobis distance (D_M) (Mahalanobis 1936), which expresses the difference between measured and predicted states in terms of standard deviations. Since D_M^2 follows a chi-squared distribution (Manly and Alberto 2016), the threshold for selecting a subset of the candidates (Figure 2-9e green circles) is chosen by the inverse chi-squared cumulative distribution at a level of 0.95 (Guerra Paradas 2017). The procedure assigns a score to each track, which is incrementally updated based on D_M^2 and the covariances in each time step (Blackman 2004).

The purpose of the next step is to select the most likely trajectory for each time step, considering that in some cases the same bubble is assigned to multiple tracks, as illustrated at the top of Figure 2-9f. Starting from e.g. t_0, a data association procedure is carried out by solving the maximum weighted independent set (MWIS) problem (Östergård 2001) to ensure that trajectories do not coincide. The bubbles at each frame are numerically coded, and each potential track is labeled as T_{ijmn}, where i corresponded to the ith bubbles detected at t_0, j to a bubble detected at t_0+dt, m at t_0+2dt, and n at t_0+3dt. Then, an undirected graph is generated by assigning each potential trajectory as a node and linking nodes if they share any bubbles at any frame (middle panel in Figure 2-9f). Each node is assigned a weight equal to the sum of the tracking scores for the recent 3 steps (red numbers in Figure 2-9f). Since the correct subset of nodes should not be interlinked, solving for the MWIS (Östergård 2001) of this graph determines all the independent trajectories with the highest global tracking scores. In the shown example, the solution identified T_{1111} and T_{2323} as the global optimal tracks. Once this procedure is completed for the first four exposures, the Kalman filter followed by the MWIS-based selection are applied to detect the bubble in the following exposures. Finally, as an added measure to assure reliable tracking, after processing the first 33% of images, the results are used for identifying a reference flow direction. Then, the whole analysis is initiated again, this time with an additional criterion limiting the deviation in the flow direction to be less than 15° from that of the reference. The codes for bubble tracking are developed and validated in-house while utilizing the available image processing and object tracking toolbox functions in MATLAB (The MathWorks, USA).

Chapter 3. Evaluation of Data Processing Methods

Obtaining accurate bubble center locations is essential for the fidelity of the results for both echo-PIV and echo-PTV. In this chapter, the current work utilizes synthetic data with various bubble densities and noise levels to evaluate the mean errors of each image enhancement method for locating bubbles. Other parameters, including the ability to resolve closely located bubbles and to distinguish between closely located blood vessels, are also evaluated based on the synthetic data. These evaluations are verified using actual CEUS images. In addition, the velocity measurement is validated in actual CEUS images based on Doppler ultrasound. The details are discussed below.

3.1. Uncertainties in bubble center location for echo-PIV and echo-PTV

3.1.1. Bubble localization by blind deconvolution and supervised learning methods

A sample raw synthetic image along with the corresponding true bubble centers and the center maps obtained from blind deconvolution, U-net, and SupBD-net are presented in Figure 3-1. In the output of the blind deconvolution, the size of each trace is about 5×5 pixels and the intensity distribution in it is quite uniform, introducing uncertainties in the intensity-weighted center location of bubbles, and limiting the ability to separate closely spaced ones. The bubble center map generated by U-net typically contains 5×5 pixels traces but with a prominent peak and dark edge, hence the bubble center location can be better estimated by intensity-weighted averaging. The size of the SupBD-net output is 3×3 times larger, hence, while the size of each trace ranges between 5×5 and 7×7 pixels, its physical size is smaller than that of the other techniques. For the pair of bubbles encircled in yellow, which are separated by 64μm, blind deconvolution cannot separate them and they are identified as a single bubble. While their traces partially overlap in the U-net output, their centers can still be identified. In the SupBD-net result, the two bubbles are clearly separated. Also, blind deconvolution is prone to enhance some of the noise, as illustrated by the areas encircled in red. This shortcoming could be mostly mitigated by setting an intensity threshold, selected as 1.5 times the mode of the histogram of the temporally averaged CEUS image intensity. Enhancement of noise is not an issue for the U-net and SupBD-net results.

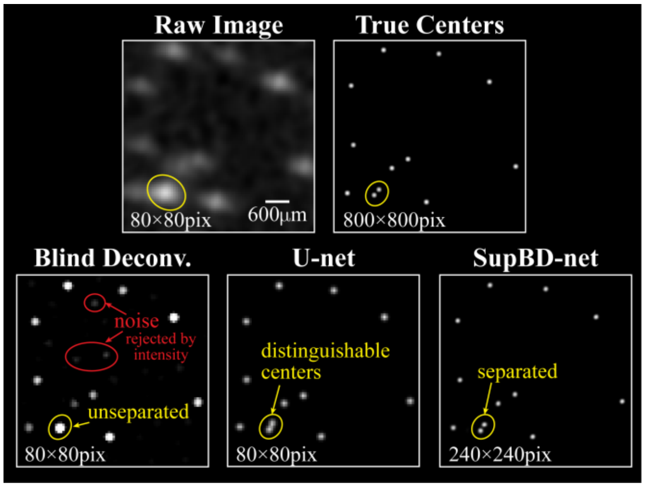
Raw Image
True Centers
80×80pix
600μm
800×800pix
Blind Deconv.
U-net
SupBD-net
noise
rejected by intensity
unseparated
80×80pix
distinguishable centers
80×80pix
separated
240×240pix

Figure 3-1 Sample images demonstrating the raw synthetic image, true bubble center map, and the center maps obtained based on blind deconvolution, U-net, and SelfBD-net. The scale bar is provided at the bottom right of the raw image and the image size is listed at the bottom of each one. Enclosed in the yellow circle are two closely seated bubbles that cannot be separated by blind deconvolution, can be separated with distinguishable centers by U-net, and are fully separated by SupBD-net. Enclosed in the red circle are falsely enhanced noises by blind deconvolution.

The accuracy of localizing bubble centers for different methods is quantified by the error in bubble center locations, E_c, defined as the spatio-temporal mean distance between the prescribed and the closest detected location of the bubble. For unseparated bubbles, where multiple true centers are detected as one, the distances are calculated for each true center. Results are summarized in Figure 3-2, where the columns, from left to right, show the effect of bubble concentration, corresponding to the low (0.25mm^{-2}), normal (0.5mm^{-2}), and high (1.0mm^{-2}) levels. The rows, from top to bottom, show the effect of increasing peak noise levels, where 0.16 is commonly seen in experiments. In each panel, the errors of blind deconvolution (black), U-net (blue), and SupBD-net (red) are presented for 5 PSFs with increasing area and aspect ratio, quantified based on the FWHM. These PSFs are selected along the scanline of the CEUS data. In general, for all cases, blind deconvolution yields the highest localization error, followed by the U-net, and then by SupBD-net. The variations of E_c with PSF sizes, bubble concentration, and noise level are discussed as follows:

First, for the same bubble concentration and noise level, E_c increases with the PSF size (area and aspect ratio). As a characteristic example, for normal concentration and typical noise level, E_c for blind deconvolution increases from 64 to 86μm with increasing PSF size. Since the typical pixel size is about 60μm, this error represents an uncertainty increasing from 1.07 to 1.43 pixels. The corresponding U-net and SupBD-net errors are 0.36-0.92 and 0.12-0.37 pixels, respectively. Hence, SupBD-net appears to be the least sensitive to the PSF sizes, followed by U-net and then by blind deconvolution. Increasing the bubble concentration reduces the average nearest neighbor distance, hence the likelihood of overlapping traces and detection error increases. Consistent with the samples shown in Figure 3-1, the SupBD-net method is the most successful in separating closely located bubbles, and is the least sensitive to the bubble concentration, resulting in the lowest localization uncertainties. Blind deconvolution is the least successful in separating traces, hence it is the most sensitive to the bubble concentration. The U-net errors fall between those of the other two approaches. Finally, as expected, for all methods, the uncertainty increases with the noise level. Yet, the changes in the SupBD-net errors are the lowest. For the highest bubble concentration and the largest PSF, the SupBD-net errors increase from 0.4 to 0.7 pixels with the increasing noise level, maintaining a subpixel level. Hence, SupBD-net achieves the highest accuracy in localizing the bubble centers and is the least sensitive to varying PSF sizes, noise levels, and bubble concentration.

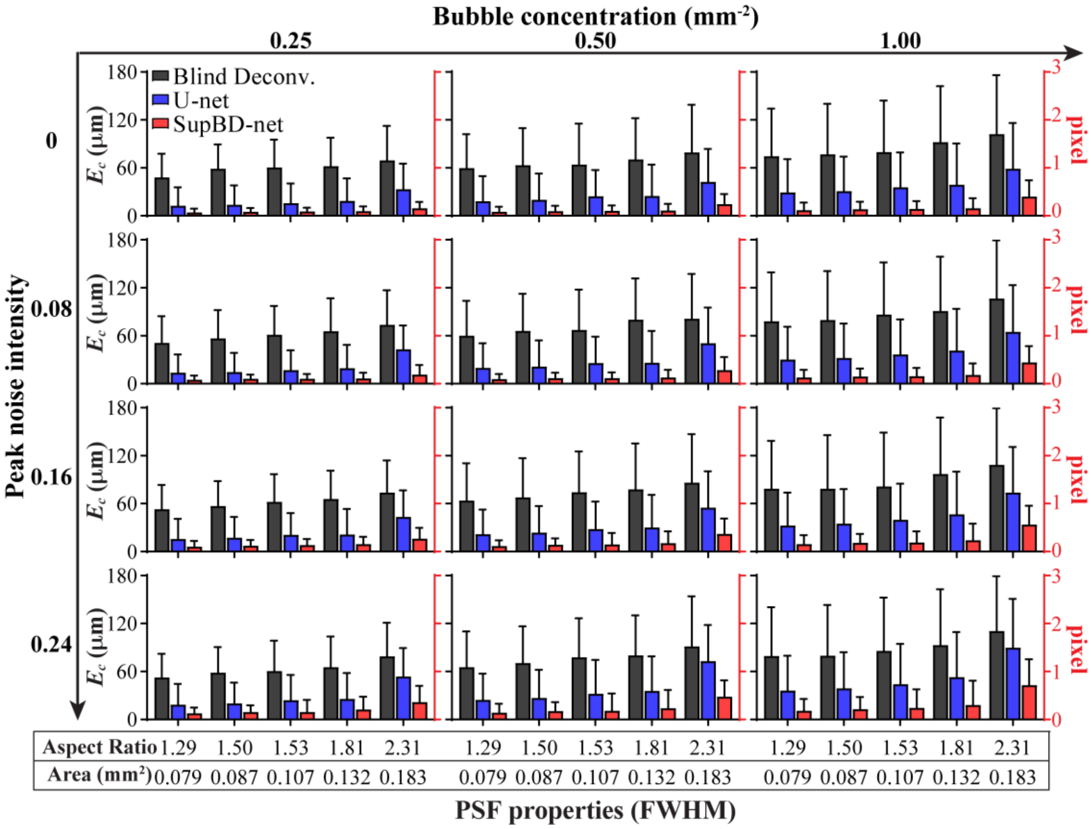

Figure 3-2 Variations of the mean error in the detected bubble center (E_c - bars) and its standard deviation (error bars) for varying bubble concentration (columns), peak noise levels (rows), and PSF area and aspect ratio (horizontal axis). Black bars: blind deconvolution, blue bars: U-net, and red bars: SupBD-net. The left vertical axis shows values in µm and the right shows values in pixels.

3.1.2. Bubble localization by self-supervised learning

Evaluation of SelfBD-net performance involves two aspects, namely the ability to reproduce the unknown PSF, and the errors in detecting the bubble centers. Sample results are visualized in Figure 3-3 using the synthetic images described in Section 2.3.2, where the PSF is vertically aligned, i.e., perpendicular to the data used for training the supervised networks. The accuracy of reproducing the unknown PSF is quantified by the 2D correlation coefficient (Q) between the intensity distributions of the true and the estimated PSFs, defined as:

$$Q = \sum_i \sum_j \left(\boldsymbol{k}_{ij} - \bar{\boldsymbol{k}}\right)\left(\tilde{\boldsymbol{k}}_{ij} - \bar{\tilde{\boldsymbol{k}}}\right) \Big/ \sqrt{\left(\sum_i \sum_j \left(\boldsymbol{k}_{ij} - \bar{\boldsymbol{k}}\right)^2\right)\left(\sum_i \sum_j \left(\tilde{\boldsymbol{k}}_{ij} - \bar{\tilde{\boldsymbol{k}}}\right)^2\right)} \qquad (3.1)$$

where $\bar{\boldsymbol{k}}$ is the spatially averaged value of the true intensity distribution and $\bar{\tilde{\boldsymbol{k}}}$ is the mean of SelfBD-net prediction. Images of the real and estimated PSFs are presented in Figure 3-3a, along with the corresponding values of Q for each sample. As is evident, the PSFs estimated by SelfBD-net are in good agreement with the real ones, with correlation coefficients varying between 0.988 to 0.992.

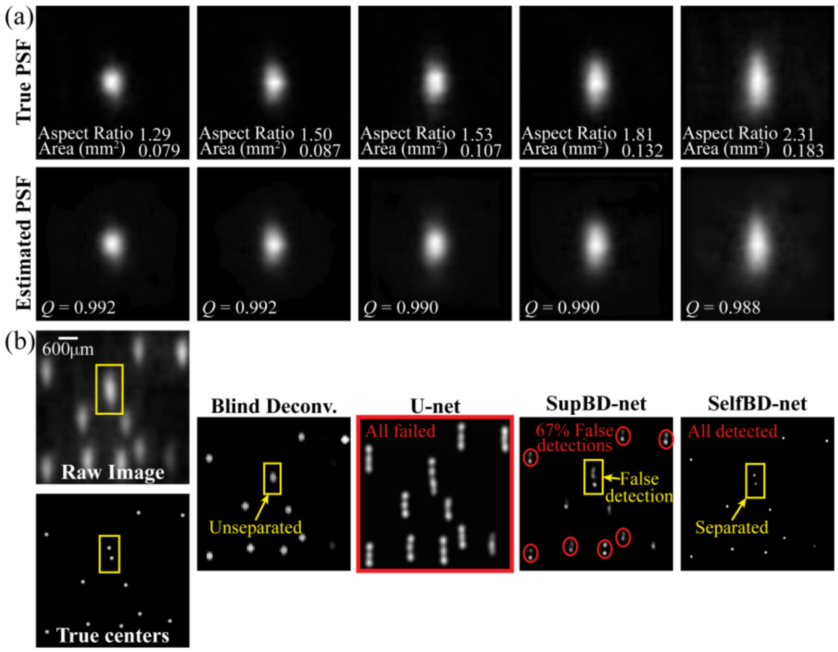
(a)
True PSF
Aspect Ratio 1.29
Area (mm²) 0.079
Aspect Ratio 1.50
Area (mm²) 0.087
Aspect Ratio 1.53
Area (mm²) 0.107
Aspect Ratio 1.81
Area (mm²) 0.132
Aspect Ratio 2.31
Area (mm²) 0.183
Estimated PSF
Q = 0.992
Q = 0.992
Q = 0.990
Q = 0.990
Q = 0.988
(b)
600µm
Raw Image
True centers
Blind Deconv.
Unseparated
U-net
All failed
SupBD-net
67% False detections
False detection
SelfBD-net
All detected
Separated

Figure 3-3 Visualization of the SelfBD-net outputs. (a) A comparison of the true (top row) and the estimated PSFs (bottom row) along with their 2D correlation coefficient (Q). (b) A sample case comparing the output of each method. Here, enclosed in the yellow box are two closely seated bubbles that are only correctly distinguished by the SelfBD-net.

A sample set of images comparing the synthetic raw CEUS image along with its corresponding true centers to those obtained by the different processing methods is demonstrated in Figure 3-3b. Similar to the results in Figure 3-1, blind deconvolution converts traces in the CEUS image into smaller blobs, which cannot distinguish closely located bubbles, e.g. the pair inside the yellow box. Both supervised learning methods (U-net and SupBD-net) encounter difficulties since the current PSF is substantially different from that of the training set. In fact, U-net fails completely by treating the vertically oriented PSF as several vertically distributed bubbles. The same issue, but to a lesser extent, affects the SupBD-net outputs. Here, the elongated PSFs are interpreted as brighter centers with dimmer ones near them, both located close to the true center. Overall, 67% of the traces are interpreted as bubble pairs. In contrast, the centers estimated by SelfBD-net appear to be in good agreement with the true data, without false detections, and with the closely located centers successfully separated.

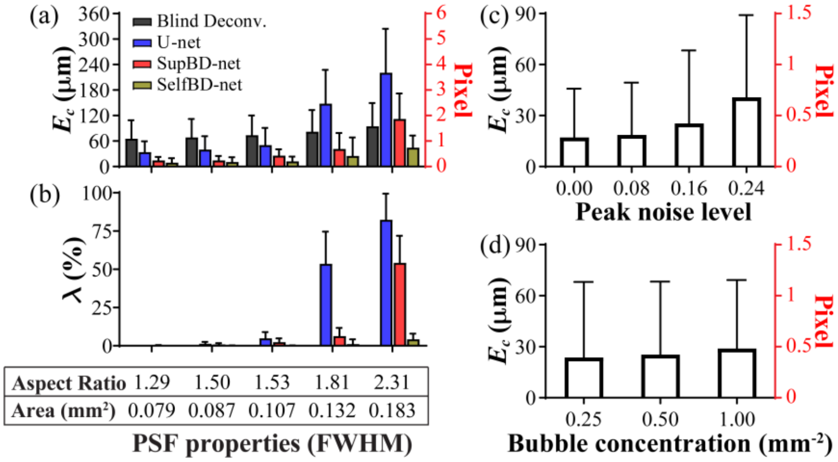

Figure 3-4 Evaluation of SelfBD-net using vertically oriented PSFs. Variations of E_c (a) and the percentage of falsely detected bubbles (λ, b) with increasingly elongated PSFs under a bubble concentration of 0.5mm^{-2} and a peak noise level of 0.16. For the PSF with an aspect ratio of 1.81, also shown are the variations of E_c with increasing noise level under a bubble concentration of 0.5mm^{-2} (c) and with increasing bubble concentration under a peak noise of 0.16 (d). For a,c, and d, the left vertical axis shows values in µm and the right in pixels. For a-d, the bar height shows mean values and the error bar shows the standard deviation.

Comparisons of E_c based on analysis of 2500 images with a bubble concentration of 0.5mm^{-2} and a peak noise level of 0.16, all for perpendicularly-oriented PSFs, are presented in Figure 3-4a. In cases of falsely detecting pairs/clusters of bubbles (Figure 3-3b), all the distances to the true center are accounted for. The corresponding percentages of falsely detected bubbles λ are shown in Figure 3-4b. Using PSF with an aspect ratio of 1.81 as an example, Figure 3-4c and d show the effects of noise and bubble concentration on the localization errors of SelfBD-net, respectively. Figure 3-4a indicates that the SelfBD-net errors are significantly lower than those of the other methods, remaining below one pixel for all the PSFs. The blind deconvolution errors increase mildly with aspect ratio but remain in the 1 to 2 pixels range. The U-net errors increase rapidly as the aspect ratio reaches 1.81, and those of the SupBD-net exceed 1 pixel for an aspect ratio of 2.31. The fraction of false detections (Figure 3-4b) of SelfBD-net remains less than 4% for all the PSFs. Consistent with the sample in Figure 3-3b, false detection of multiple bubbles is not an issue for blind deconvolution. For aspect ratios smaller or equal to 1.53, both supervised learning methods are able to handle unfamiliar PSFs with false detections of less than 5%. However, they fail at higher aspect ratios, U-net at 1.81 or higher, with over 50% false detections, and SupBD-net at 2.31. Hence, the current training strategies for supervised learning methods are able to extend their generalizability but to a limited extent. While the SelfBD-net errors increase with noise level (Figure 3-4c), they remain well below 1 pixel for a concentration of 0.5mm^{-2}. Furthermore, for a characteristic noise of 0.16 (Figure 3-4d), E_c does not increase significantly with the bubble concentration. Clearly, for the perpendicular PSFs, i.e. cases that the supervised learning methods are not trained for, the performance of SelfBD-net is superior to that of the other techniques, giving the least errors and false detection. Hence, such an analysis proves the better generalizability of SelfBD-net than that of other supervised learning methods.

Figure 3-5 compares the performance of SelfBD-net using the same evaluation dataset in Section 3.1.1, i.e., datasets with horizontally oriented PSFs. The analysis focuses on the case with a bubble concentration of 0.5mm^{-2} and a peak noise level of 0.16. The first part of the comparison examines the ability to distinguish closely located bubbles with overlapped bubble traces. The data are grouped in terms of D^*, the center-to-center distance of each bubble from its nearest neighbor normalized by the length of the PSF FWHM along the line connecting the two centers. The percentage of unseparated bubble traces as a function of D^* is plotted in Figure 3-5a. As is evident, in all cases, all the methods fail at some D^*. Blind deconvolution has the worst performance, with the fraction of failed separation exceeding 5% at $D^* < 1.05$, followed by U-net ($D^* < 0.97$), and then with significantly better outcomes by SelfBD-net and SupBD-net ($D^* < 0.6$). While the difference between the latter is small, as expected for this dataset, SupBD-net performs better for $D^* < 0.5$. The effect of PSF size on E_c for SelfBD-net and SupBD-net are plotted in Figure 3-5b. Results for the other methods, which have significantly higher errors are already presented in Figure 3-2. Both techniques maintain subpixel errors ranging between 0.2 to 0.4 pixels, with those of SelfBD-net being slightly higher. This difference can be traced back to the effect of noise. While SupBD-net is trained by comparing the predictions based on noisy data to the true centers, SelfBD-net only partially accounts for the noise by adding terms with higher SNR. Even with correctly estimated $\tilde{\boldsymbol{x}}$ and $\tilde{\boldsymbol{k}}$, the noise in $\boldsymbol{y}$ would result in a non-zero loss in Eqn. (2.6), hence the optimizer would adjust the parameters of the x-net and k-net that introduce errors in $\tilde{\boldsymbol{x}}$ and $\tilde{\boldsymbol{k}}$. Therefore, although SelfBD-net is initiated based on the bubble centers estimated by SupBD-net, its output may deviate slightly after a few iterations.

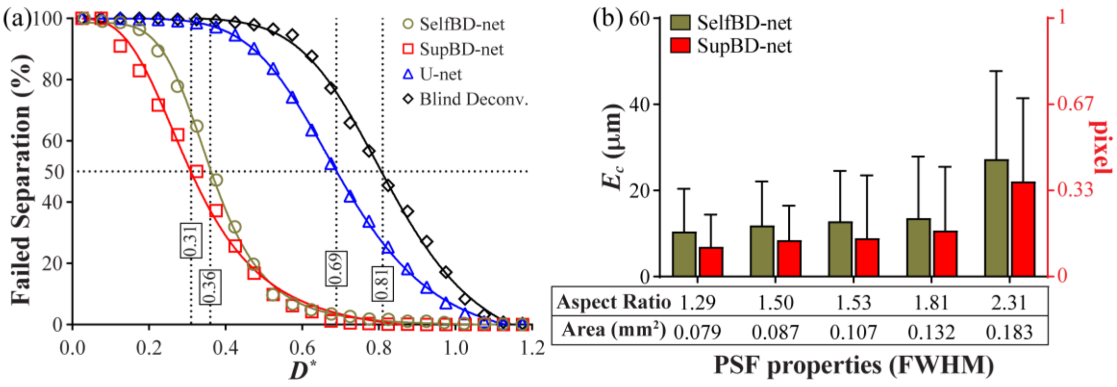

Figure 3-5 Evaluation of SelfBD-net using the same dataset as Section 3.1.1 with horizontally oriented PSFs, a bubble concentration of 0.5mm^{-2}, and a peak noise level of 0.16. (a) Variations of the percentage of unseparated bubbles with the normalized bubble distance, which is defined for each bubble as the distance to its nearest neighbor normalized by the length of the PSF FWHM along the line connecting the two centers (D^*). (b) Comparison of E_c between SelfBD-net and SupBD-net for increasing PSF size. The left vertical axis shows values in μm and the right in pixels. The bar height shows mean values and the error bar shows the standard deviation.

3.2. The spatial resolution of vessel detection for echo-PTV and ULM

3.2.1. Evaluation of the spatial resolution based on synthetic images

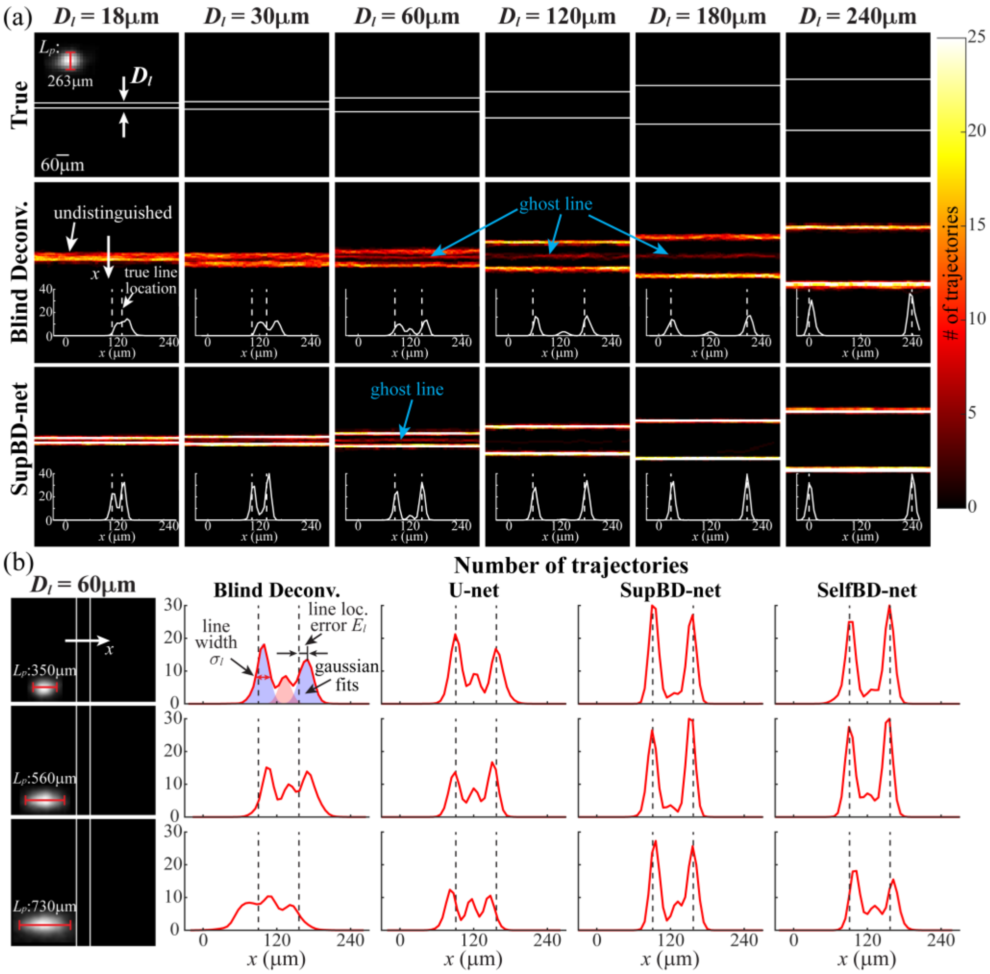

Figure 3-6 Spatial resolution of closely located parallel lines for different image processing methods. (a) Sample heatmaps of bubble trajectories showing the effect of increasing line spacing (D_l). (b) Sample cross-sectional profiles showing the effect of PSF FWHM length in the direction perpendicular to the line (L_p). The definitions of the error in line location (E_l) and line width (σ_l) are indicated in the top left. For (a) and (b), the vertical dashed lines show the true location of each line.

In this section, we evaluate the ability of the various image processing methods to distinguish closely located parallel bubble trajectories, and to determine the errors in their locations for varying PSF sizes and distances between vessels (D_l). As discussed by several recent papers, e.g. Demené et al. (2021) and Zhang et al. (2022), these trajectories are used for mapping the location of micro- and macro-blood vessels in internal organs. In the present analysis, the vessel locations are identified based on tracks of 60 random bubbles passing through each line. Note that the bubbles are generated and translated along the lines at two series of independent time points for each line, where bubbles from each line could be overlapped or isolated at different time steps. The PSFs are aligned horizontally, and the vessels are either horizontal (Figure 3-6a) or vertical (Figure 3-6b). Hence, the PSF dimension that affects the ability to resolve closely spaced vessels is the FWHM length in the direction perpendicular to the vessel (L_p), as indicated in the figures. The resulting bubble trajectories are pixelated on images at 10 times the native image resolution, where the pixel size is equivalent to the microbubble diameter.

Figure 3-6a demonstrates the impact of D_l on the detected pair of horizontal vessels for a fixed L_p of 263μm. The reference line spacing is shown in the top row, the blind deconvolution results are presented in the middle row, and the SupBD-net data is in the bottom row. For both cases, the reconstructed lines and their cross-sectional profiles averaged along the line are provided. Since each trajectory is defined based on 60 bubbles, a peak of e.g. 20 indicates that a third is detected exactly along the center. Also, each plot shows the location of the original line, and its distance from the detected peak represents a location error, which is quantified later. Figure 3-6a shows that for blind deconvolution results at D_l =18μm, the two lines cannot be distinguished. As D_l increases to 30μm, the two lines are separated, but with considerable overlap, and connected tails. For D_l =60μm, the image contains two primary lines with a "ghost" line between them. The latter occurs in cases where two bubbles appear at nearly the same time, and consequently overlap, resulting in trajectories defined by the combined point spread function. The height of the ghost line diminishes with increasing line spacing and disappears for D_l =240μm. The existence of a ghost line poses a challenge since one cannot simply dismiss it in a real image where the number of bubble traces varies among vessels. This topic is discussed later, as we introduce a systemic method for determining the proper threshold to identify a vessel. A similar progression that includes two overlapped lines, the formation of a ghost line, and complete separation occurs also for the SupBD-net data. Here, the two lines are already detected at D_l =18μm, and while the ghost line appears at 60μm, it completely disappears for D_l ≥120μm. Moreover, it could be observed that the blind deconvolution results have larger errors in the line location, especially for small line spacings, and decay with increasing line spacing. In contrast, the detected line location is very close to the reference location for all line spacings in SupBD-net results. The effect of PSF size is demonstrated for all four techniques in Figure 3-6b using examples of vertical trajectories for a fixed D_l of 60μm. For all cases, L_p is much larger than the line spacing. In general, for each L_p, the intensity of the ghost line is the highest for blind deconvolution, followed by U-net, SelfBD-net, and SupBD-net. With increasing L_p, the intensity of the ghost line increases for all techniques. These trends are consistent with the ability to separate closely located bubbles, as demonstrated in Figure 3-5a. Moreover, the line location errors also increase with increasing L_p for all methods, where errors are larger in blind deconvolution and U-net results than those of SupBD-net and SelfBD-net. Clearly, the trajectory detection by SelfBD-net and SupBD- net is superior to those of U-net and blind deconvolution.

For the quantitative analysis of the performance of each method in reconstructing the primary lines, as marked in the top left of Figure 3-6b, the profile is fitted with the sum of multiple gaussian distributions (shadowed region) matching the number of peaks using the MATLAB Curve Fitting Toolbox. The line location error (E_l) is defined as the distance between the gaussian fitted peak location of each primary line to the corresponding true line location, and the line width (σ_l) is defined as the distance between plus/minus one standard deviation of the gaussian. Since the spatial resolution of the parallel lines is jointly affected by D_l and L_p, we thereby define a nondimensionalized PSF size $L_p^* = L_p / D_l$, and plot its impact on the nondimensionalized E_l^* and σ_l^*, all by D_l, in Figure 3-7. As shown in Figure 3-7a, for each method, the E_l^* increases with increasing L_p^* following a power law. The power is highest for blind deconvolution, followed by U-net and SelfBD-net sharing a similar level, and then SupBD-net. The scaling coefficients are similar for blind deconvolution and U-net, but are 1.5 times larger than those of SupBD-net and SelfBD-net. Hence, in general, the E_l^*, from the largest to the smallest, are obtained from the results of blind deconvolution, U-net, SelfBD-net, and SupBD-net. Such an order is consistent with the trend for bubble location error. As for the nondimensionalized line width shown in Figure 3-7b, it also increases with L_p^* following a power law for each method, but the data are better aligned with the fit than those of E_l^*, as confirmed by the higher coefficient of determination R^2. The powers and the scaling coefficients follow the same trend as that of the E_l^*, showing the largest values for blind deconvolution and the smallest for SupBD-net, with U-net and SelfBD-net in the middle.

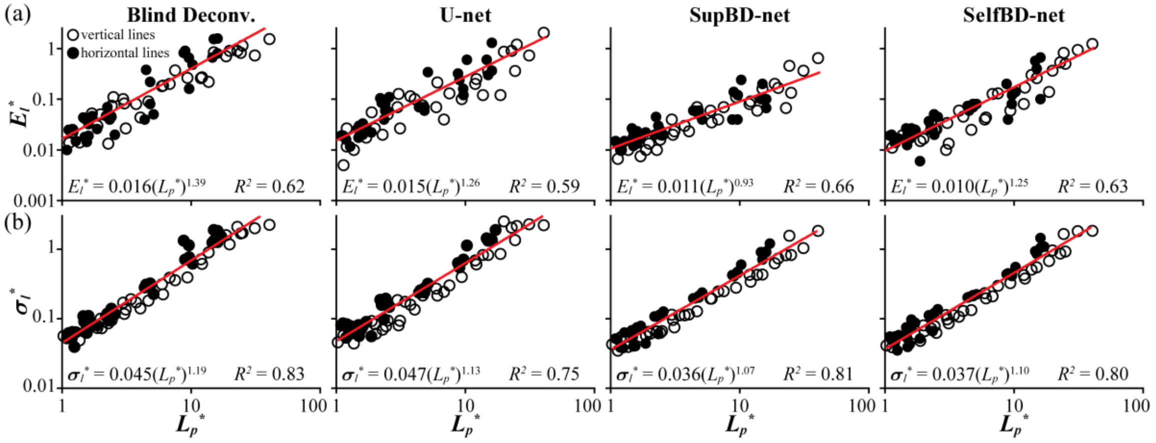

Figure 3-7 Variations of nondimensionalized: (a) line location error (E_l^*), and (b) line width (σ_l^*) with PSF size (L_p^*). All variables are nondimensionalized by the corresponding line spacing. The red line shows the least-square-fitted power law, whose expression as well as the coefficient of determination (R^2) are provided at the bottom of each panel. The solid dots denote data of horizontal lines, and hollow dots represent data of vertical lines.

As demonstrated in Figure 3-6, the existence of a ghost line causes false detection, where two closely located microvessels are identified as three, and in other cases, closely spaced lines could be detected as one. While some ghost lines share similar features as the primary lines, e.g. the blind deconvolution results for D_l=60µm, others are dimmer and discontinuous, e.g. the SupBD-net results for D_l=60µm, hence they can be identified and filtered out.

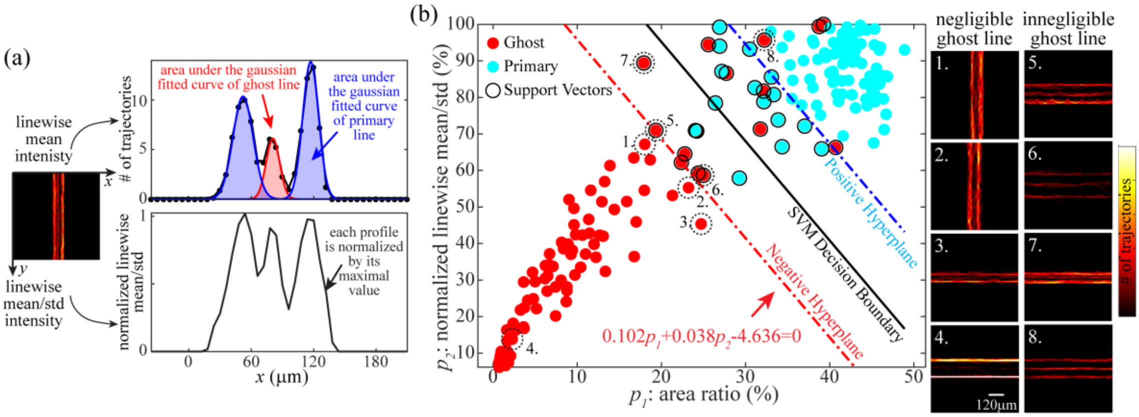

Figure 3-8 Determining the threshold for negligible ghost lines using Support Vector Machine (SVM). (a) Sample illustration of the definition of the parameters, namely, the area ratio occupied by each line structure, p_1, and the linewise mean/standard deviation of the intensity for each peak which is normalized by the maximum peak, p_2. (b) Scatter plots of p_1 and p_2, as well as the decision boundaries estimated by the SVM. The red dots represent data of ghost lines, the blue dots represent data of primary lines, and the black encircled ones are the support vectors. A few examples are shown on the right side demonstrating cases with negligible ghost lines (cases 1-4), and inngeligble ones (cases 5-8).

Two parameters have been selected to distinguish the ghost/false lines from the primary ones. As illustrated in Figure 3-8a, the first is the area covered by each line divided by the total area covered by all the lines (p_1), where the value associated with the ghost line quantifies the percentage of falsely detected bubbles. To calculate p_1, the linewise averaged heatmap profiles are fitted with the sum of multiple gaussian profiles, and the area is calculated based on these fits. The second is the linewise mean intensity divided by the standard deviation for each peak (p_2), which is normalized by the maximum value for each case. This parameter quantifies the structural continuity along the line, where dim structures with low mean values or discontinuous structures with high standard deviations have low values. A scatter plot of p_1 and p_2 is presented in Figure 3-8b, where red dots show the values for ghost lines and blue dots show values for the primary lines. As is evident, the data are generally divided into two groups but with some ambiguities in the middle. To determine a threshold for separating these two groups, we utilize a Support Vector Machine (SVM), provided by MATLAB Statistics and Machine Learning Toolbox, to search for an optimal decision boundary that separates the data into two classes (Cristianini and Shawe-Taylor 2000). In Figure 3-8b, the black encircled dots are the support vectors, the black line shows the decision boundary, and the red and blue lines show the negative and positive hyperplanes, respectively. A few examples are demonstrated on the right to visualize the effectiveness of this approach. Close to the negative hyperplane, the ghost lines appear to be visually negligible for cases located to the left, e.g., cases 1-3, whereas those on the right, e.g. cases 5-7, appear to be similar to the primary lines. Far below the negative hyperplane, e.g. case 4, there is no visible ghost line. In contrast, on the right of the positive hyperplane (case 8), the ghost line is similar to the primary lines. Hence, we have selected the negative hyperplane as the boundary of negligible ghost lines. Based on such an analysis, we have characterized the outcome of each method to separate closely located parallel lines into five categories, namely, unseparated, separated into two lines with overlap, separated with innegligible ghost lines, separated with negligible ghost lines, and fully separated. Note that for the profiles of two lines with significant overlap, if the intensity of the valley is larger than 95% of the primary line intensity, these two lines are considered unseparated. The results are summarized in Figure 3-9. It can be seen that blind deconvolution is not able to resolve all the lines that are 18μm apart, and it cannot resolve the ones that are 30μm apart for a PSF size larger than 410μm. For all lines that are 60 and 120μm apart, it yields ghost lines that are similar to the primary lines; and as the line spacing increases from 180 to 360μm, most of the cases are either separated with negligible ghost lines or fully separated. The amount of cases with unseparated lines reduces in the order of blind deconvolution, U-net, SelfBD-net, and SupBD-net, while the number of cases that are separated with negligible ghost lines or fully separated increases in the same order. For SupBD-net, except for the cases at D_l=18 to 60μm with L_p=730μm, all of the rest can be either fully separated or separated with overlap or with negligible ghost lines.

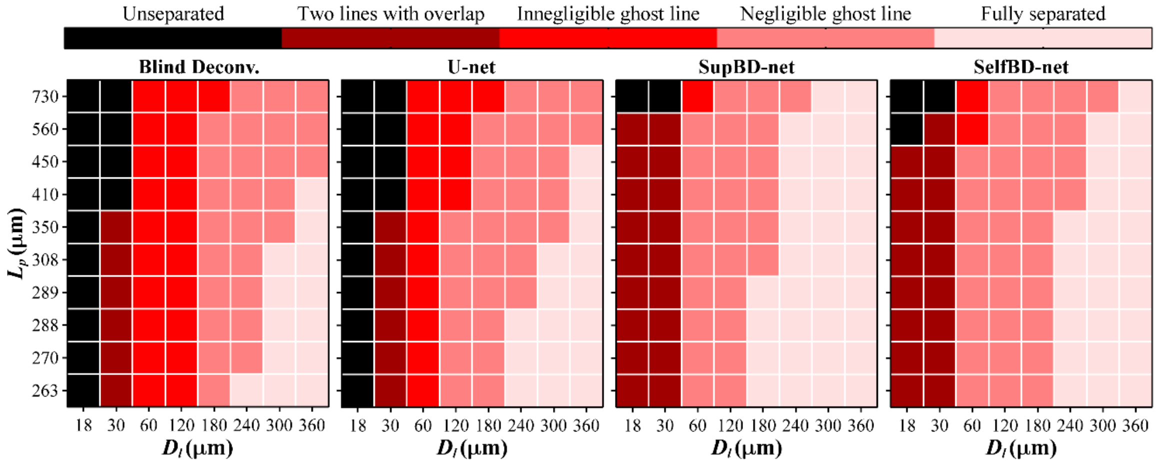

Figure 3-9 Summarization of the ability of each method to separate closely located parallel lines for all D_l and L_p.

It should be noted that the current analysis only focuses on two horizontally and vertically aligned lines. In actual CEUS images, the microvessels are aligned in all directions and there are usually more than two microvessels in the neighborhood. Nonetheless, such an analysis provides an estimation of the horizontal and vertical spatial resolution of each method in an ideal circumstance, which could be verified in the next section.

3.2.2. Evaluation of the spatial resolution and velocity measurement via real CEUS data

In this section, real CEUS images obtained from a piglet's cerebral cortex are used for verifying the spatial resolutions of different image processing methods for visualizing microvasculature. As demonstrated in Figure 3-10a, the data generally show consistent macrovascular structures, yet there are fewer signals in microvascular regions for blind deconvolution results than those of SupBD-net and SelfBD-net. To better demonstrate such a phenomenon, a magnified view of the white-enclosed subregion containing a cluster of microvessels is provided for each result. The densely distributed parallel microvessels are consistent for SupBD-net and SelfBD-net, while those for U-net and blind deconvolution are sparser and only contain larger scale microvessels.

To quantitatively compare the spatial resolution of different methods on the actual CEUS data, a magnified view of the microvascular region in the blue box of Figure 3-10a is provided in Figure 3-10b. The PSF FWHM short axis size for this region is 270µm. Two cross-sectional profiles along four closely spaced microvessels (line 1) and two microvessels spaced farther apart (line 2) are also demonstrated in Figure 3-10b. For line 1, the data of SupBD-net and SelfBD-net are consistent, both showing four microvessels that are spaced by, from left to right, ~85µm, ~80µm, and ~42µm. The U-net is able to separate, even though they are identified as spaced by 74µm, the vessels that are spaced by ~85µm, yet it cannot distinguish the latter two vessels that are spaced by ~42µm. As for blind deconvolution, the four vessels are identified as two, with a distance of ~80µm. Such a result is consistent with the previous analysis where the SupBD-net and SelfBD-net have the best spatial resolution, followed by U-net, and blind deconvolution. As the vessel spacing increases to more than 120µm, in line 2, the two blood vessels are separated by all methods. However, the blind deconvolution and U-net show similar line spacings of ~145µm, yet those of SupBD-net and SelfBD-net are ~135µm. The 10µm difference is equivalent to a relative error of

7% compared to the SupBD-net data.

The width of moderate blood vessels (with a diameter of ~250µm) has been used as a criterion to separate micro to macro vessels (Zhang et al. 2022), whereas their locations are needed to determine the regions containing only microvessels. Hence, the ability to identify the width and location of such vessels is demonstrated by a cross-sectional profile along line 3 in Figure 3-10b. The U-net, SupBD-net, and SelfBD-net show a consistent line location, while it is 189µm for blind deconvolution, resulting in a relative error of 9% compared to SupBD-net data. As for the vessel width, which is quantified by the FWHM of the profile, the SupBD-net and SelfBD-net give a similar value of 142µm, while U-net and blind deconvolution show a 6% and 28% smaller value than that of the SupBD-net. In general, for such vessels, the location and width results for U-net, SupBD-net, and SelfBD-net are consistent, while the blind deconvolution result might be less reliable.

To evaluate the velocity measured by the present tracking procedure, results obtained for a macro blood vessel are compared to those measured by pulsed-wave Doppler Ultrasound at the same location. As reported (Walker 2009), the uncertainty of Doppler measurement in the 2.5-10 cm/s range is lower than 5%, hence it could be used for validating the PTV data. Since the measurements are performed at different times, but under the same physiological conditions, the comparison is based on phase-averaged velocities in the cardiac cycle. Such a comparison could only be performed for the macro-vessels since the velocity in the micro-vessels falls below the detection limit of the Doppler system. The upper threshold of PTV measurements is selected as 11 cm/s by examining multiple images and assessing the maximum velocity for which three exposures could be readily detected based on the current framerate. The results are summarized in Figure 3-11. The scatter plot comparing phase-averaged data under the same conditions (piglet number, ICP, cardiac phase) in Figure 3-11a shows that the results of the two techniques agree well within their overlapping range. Results of the Bland-Altman analysis presented in Figure 3-11b confirm that the bias between the PTV and Doppler is nearly zero (-0.01 cm/s) and that the 95% confidence interval is ±1.2 cm/s. Finally, a series of phase-averaged velocity profiles for one piglet (Figure 3-11c) at varying ICP levels demonstrate that, for velocities falling below 11cm/s, the Doppler and PTV measurements agree well. Deviations occur when the velocity exceeds the maximum PTV limit, resulting in a downward bias in results. It should be emphasized that the velocities in the micro-vessels, the main topic of this work, are an order of magnitude smaller than the maximum detectability limit of PTV, i.e., they can be reliably measured at the current framerate.

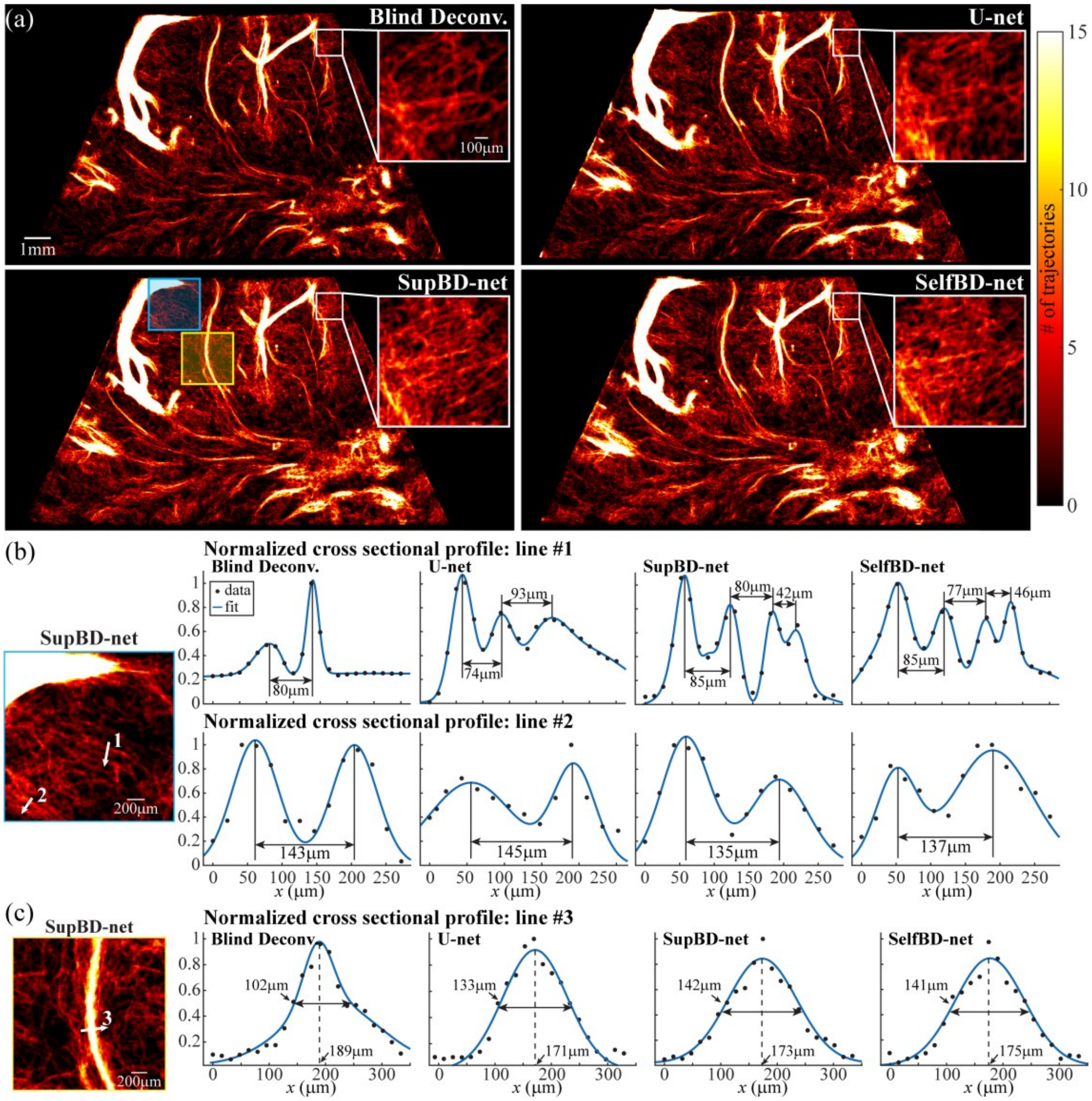
(a)
Blind Deconv.
U-net
SupBD-net
SelfBD-net
100μm
1mm
15
10
5
0
# of trajectories
(b)
Normalized cross sectional profile: line #1
Blind Deconv.
U-net
SupBD-net
SelfBD-net
data
fit
80μm
93μm
74μm
80μm
42μm
85μm
77μm
46μm
85μm
SupBD-net
1
2
200μm
Normalized cross sectional profile: line #2
143μm
145μm
135μm
137μm
x (μm)
(c)
SupBD-net
3
200μm
Normalized cross sectional profile: line #3
Blind Deconv.
U-net
SupBD-net
SelfBD-net
102μm
189μm
133μm
171μm
142μm
173μm
141μm
175μm
x (μm)

Figure 3-10 Visualization of cortical microvasculature in the left cerebral hemisphere of a piglet. (a) Maps of blood vessels obtained by different image processing methods. White-enclosed subregions are magnified to demonstrate their abilities to reconstruct a cluster of microvessels. (b) A magnified view of the blue-enclosed region in (a). Two cross-sectional profiles along four closely spaced microvessels (line 1) and two moderately spaced microvessels (line 2) are provided to compare the spatial resolution of different methods. (c) A magnified view of the yellow-enclosed region in (a), where the cross-sectional profile along a moderate blood vessel (line 3) is provided for all methods comparing their abilities to identify the location and width of such vessels.

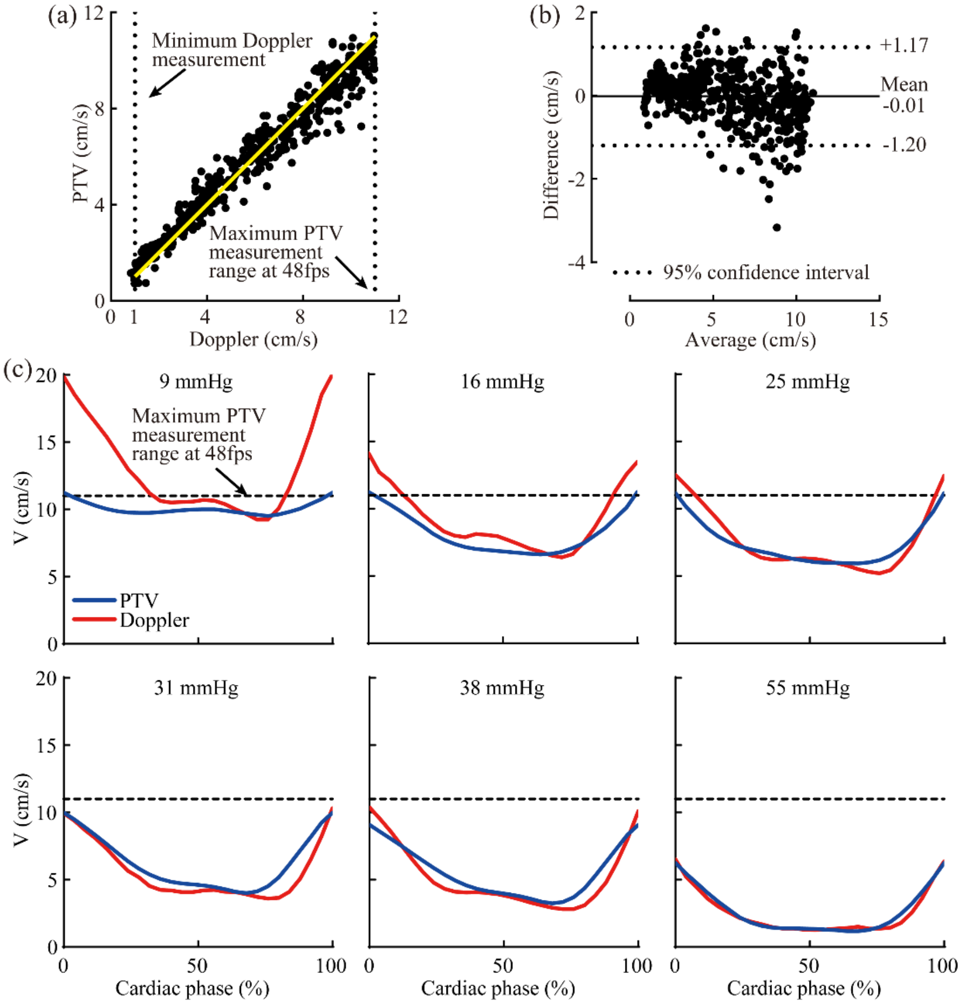

Figure 3-11 Evaluation of the velocity measurement. (a) A scatter plot comparing the phase averaged velocities measured by echo-PTV and pulsed-wave Doppler ultrasound. Results beyond the maximum PTV measurement range (11 cm/s), and below the minimum range of Doppler measurements (1 cm/s), are not included. Most of the micro-vessel data fall below the doppler limit. (b) A Bland-Altman plot comparing the PTV and Doppler measurements, with the mean value and the 95% confidence interval highlighted. (c) A comparison of the PTV- and Doppler-measured phase-averaged velocity distributions in a blood vessel at varying intracranial pressure levels.

Chapter 4. Application of Echo-PIV in Cardiovascular Flows

4.1. Background: monitoring cardiac flows during VA-ECMO

Veno-arterial extracorporeal membrane oxygenation (VA-ECMO) is a medical procedure that provides both respiratory and circulatory support to patients by oxygenating blood outside the body and returning it to the arterial system through the femoral artery (Pavlushkov et al. 2017). Determining the optimal VA-ECMO flow rate (Q_E) is challenging (Martin et al. 1991; Becker et al. 1998). High Q_E is favorable for adequate end-organ perfusion, but the retrograde arterial ECMO flow may increase the afterload to the heart (Burkhoff et al. 2015; Rao et al. 2018), increasing the metabolic work demand on the myocardium and hindering myocardial tissue recovery (Ostadal et al. 2015). Clinical management relies on monitoring the hemodynamic states (Chung et al. 2014; Schmidt et al. 2015), but outcomes of the therapy are influenced by patient- and treatment-related factors (Lim et al. 2017b; Donker et al. 2019). Insights regarding the interactions between ECMO flows and native cardiac output at the admixing zone may lead to a quantitative assessment of the impact of the afterload created by the retrograde arterial flow. Here we use the optimized echo-PIV/PTV to characterize the interactions between ECMO flow and native cardiac output in the aortic root of an adult Yorkshire pig with severe myocardial ischemia. The instantaneous and phase-averaged velocity distributions are analyzed to elucidate the effects of the ECMO flow rate on the flow patterns, as well as the duration and magnitude of cardiac outflow. These insights could potentially improve the management of patients receiving VA-ECMO.

4.2. Phase-averaged flow field

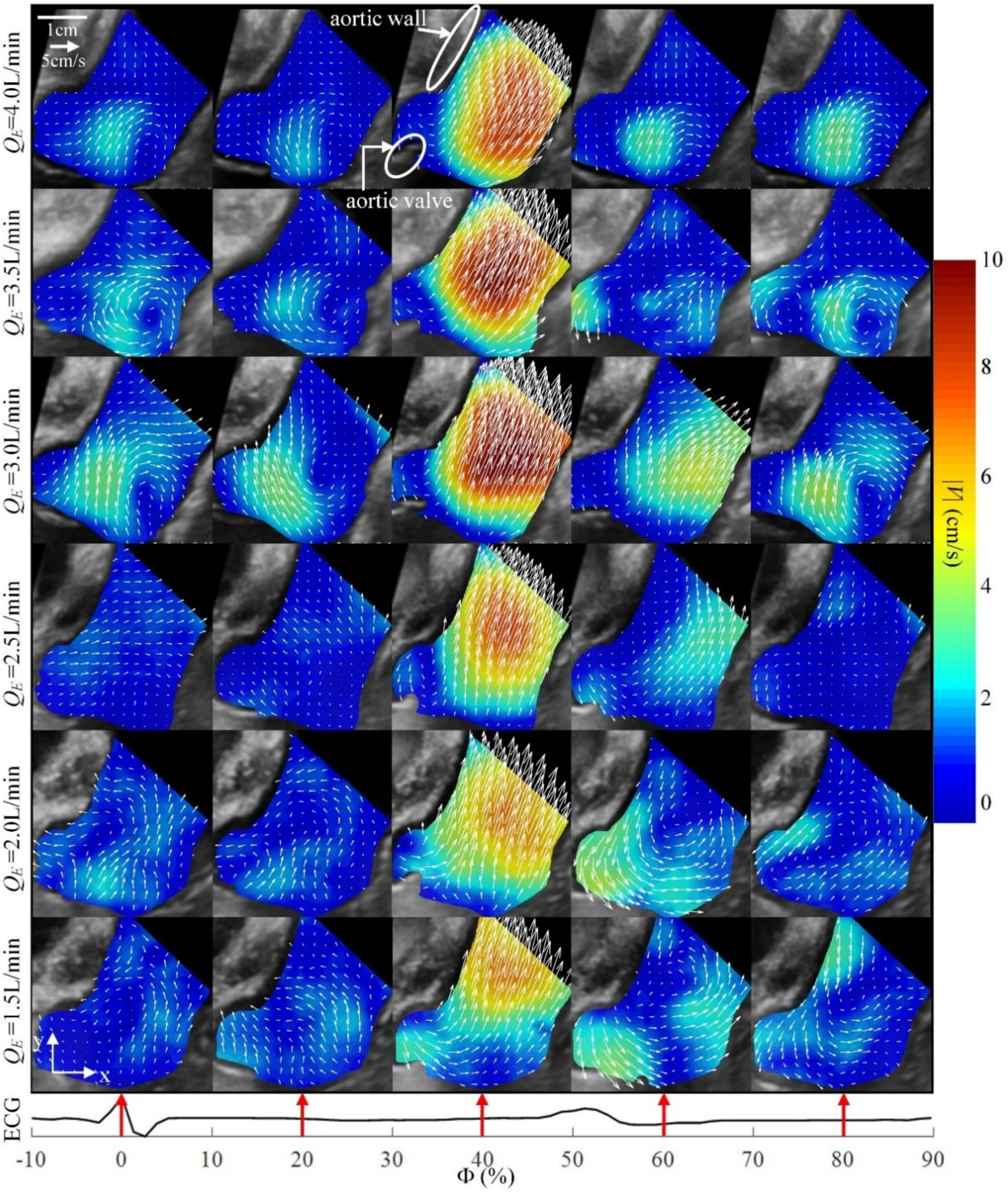
1cm
5cm/s
aortic wall
aortic valve
Q_E=4.0L/min
Q_E=3.5L/min
Q_E=3.0L/min
Q_E=2.5L/min
Q_E=2.0L/min
Q_E=1.5L/min
y
x
10
8
6
4
2
0
|V| (cm/s)
ECG
-10
0
10
20
30
40
50
60
70
80
90
Φ (%)

Figure 4-1 Vectors and contour maps of the phase-averaged velocity magnitude (|*V*|) for varying ECMO flow rates (rows) and phases in the cardiac cycle (columns). The ECMO flow rate is indicated on the left, and the cardiac phase in the bottom. A reference vector is provided in the top left corner. The sample electrocardiogram (ECG) corresponds to Q_E=4.0L/min.

Figure 4-1 shows the phase-averaged velocity for five selected phases of the cardiac cycle for all the present values of Q_E. The selected phases (Φ) are specified as a percentage of the cardiac cycle, starting from the R wave peak of the ECG. As is evident, the jetting during systole (Φ~40%) strengthens as Q_E is decreased from 4.0 to 3.0L/min, but then decreases with the further reduction of the flow rate. During diastole, prominent secondary flows consist of a clockwise vortex in the sinus at $Q_E \geq 3.0$L/min, and a counterclockwise vortex above the sino-tubular junction at lower Q_E. These vortices are most likely parts of three-dimensional flow phenomena that cannot be characterized based on the present 2D section through the aortic root. It should be noted that, in a few cases (Q_E=1.5, 2.0, and 4.0L/min) shown in Figure 4-1, the right sinus is not as prominent as others, which is caused by changes to the location of the transesophageal probe as time progressed.

4.3. Characterization of cardiac outflow during VA-ECMO

To quantify the cardiac outflow, we follow the spatio-temporal evolution of the velocity component perpendicular to the sino-tubular junction (v_c) over a line located 0.8cm downstream of it, which is visible and consistent in all the present sample areas, as defined in Figure 4-2. The corresponding extent of the aortic valve opening is characterized by the measured distance between the valve leaflet tips (Figure 4-2).

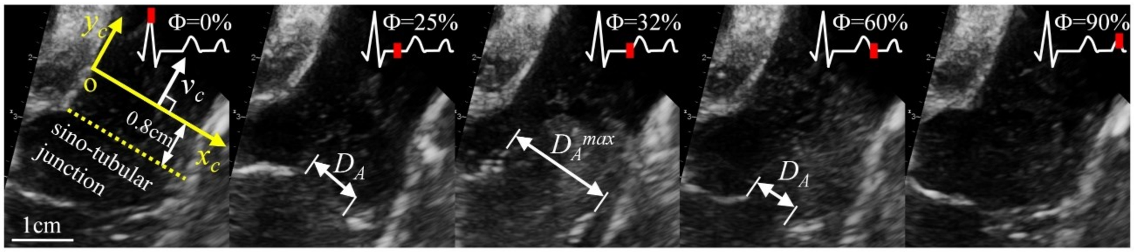

Figure 4-2 Sample instantaneous images of the aortic valve for Q_E=3.0L/min showing the distance between valve tips (D_A). Indicated in the first column is the location and orientation of the line ox_c located 0.8cm away from the sino-tubular junction where v_c is measured.

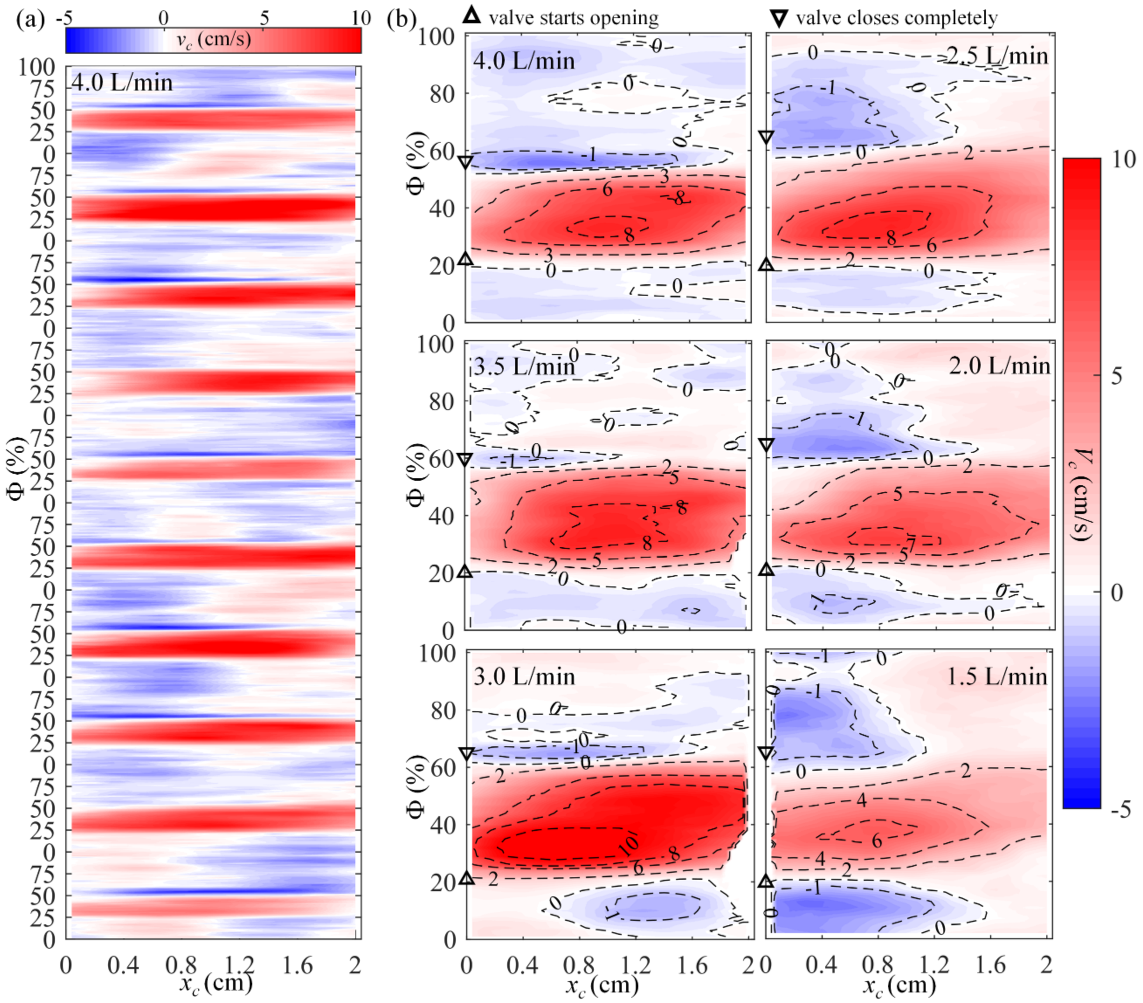

Figure 4-3 (a) Sample spatio-temporal evolution of v_c along the line ox_c for Q_E=4.0L/min. (b) Phase-averaged velocity distributions (V_c) along the line ox_c for each Q_E.

Sample time evolution of the distribution of v_c for Q_E=4.0L/min is presented in Figure 4-3a. Prominent features include periodic ejections with v_c=8-10cm/s, followed by a short period (ΔΦ~7%) of reverse flow across most of the aorta and in most cycles while the aortic valve closes. There are no persistent spatial velocity distributions among cycles during diastole. Plots of the phase-averaged velocity over ten cycles (V_c) for each Q_E are presented in Figure 4-3b. They indicate that the peak magnitude of V_c and phase interval of positive outflux increase as Q_E decreases from 4.0 to 3.0L/min, peaking at 10cm/s. Conversely, upon further reduction in Q_E to 2.5, 2.0, and

1.5L/min, the maximum V_c decreases to 8, 7, and 6cm/s, respectively, and the phase interval of positive outflux decreases to $\Delta\Phi$=44.5%, 42%, and 40%. The abovementioned short period of reverse flow (V_c<-1cm/s) across the aorta as the valve closes appears only at Q_E=4.0 and 3.0L/min. Longer periods with V_c<-1cm/s appear only in the upper part of the aorta at Q_E≤2.5L/min. Some of the present trends of the flow structures in the aortic root are consistent with phase contrast MRI measurements, which do not involve ECMO. For example, similar to the results in Figure 4-3b, the same retrograde flow has been measured in healthy human patients during late systole and early diastole along the left aortic wall (Kilner et al. 1993; Markl et al. 2004). The pattern resembling the presently observed pair of counter-rotating vortices during diastole at high ECMO flow rates (Figure 4-1), has also been observed using vector flow imaging (Hansen et al. 2015). Moreover, Gu et.al. (2018) have studied the flow field inside the aorta during VA-ECMO by numerical simulation. Their simulated flow fields have also shown that the ejection from the native heart gets stronger as the ECMO flow rate is reduced, which is consistent with our measurements.

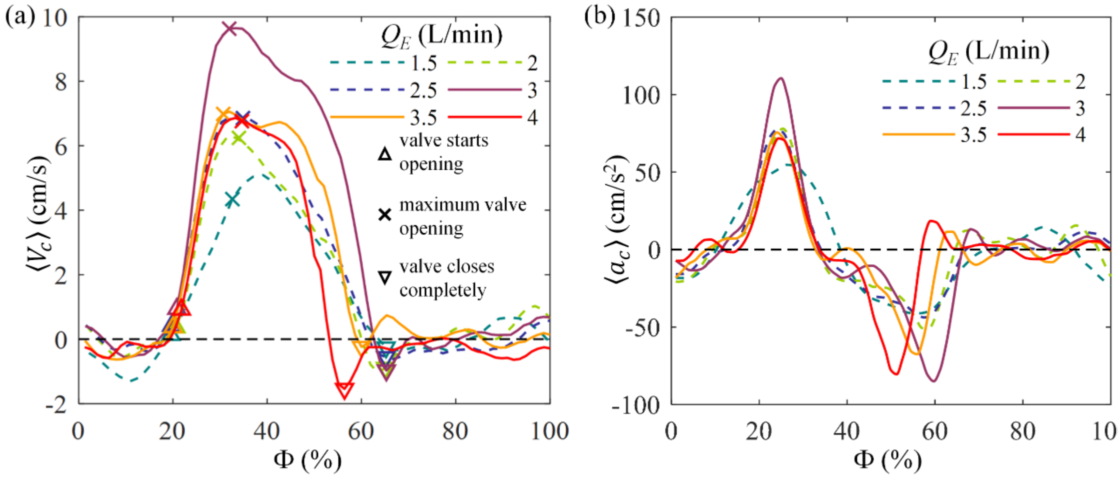

Figure 4-4 (a) Phase evolution of the spatially averaged velocity $\langle V_c \rangle$. (b) Phase evolution of the rate of change of $\langle V_c \rangle$ ($\langle a_c \rangle = \partial \langle V_c \rangle / \partial t$).

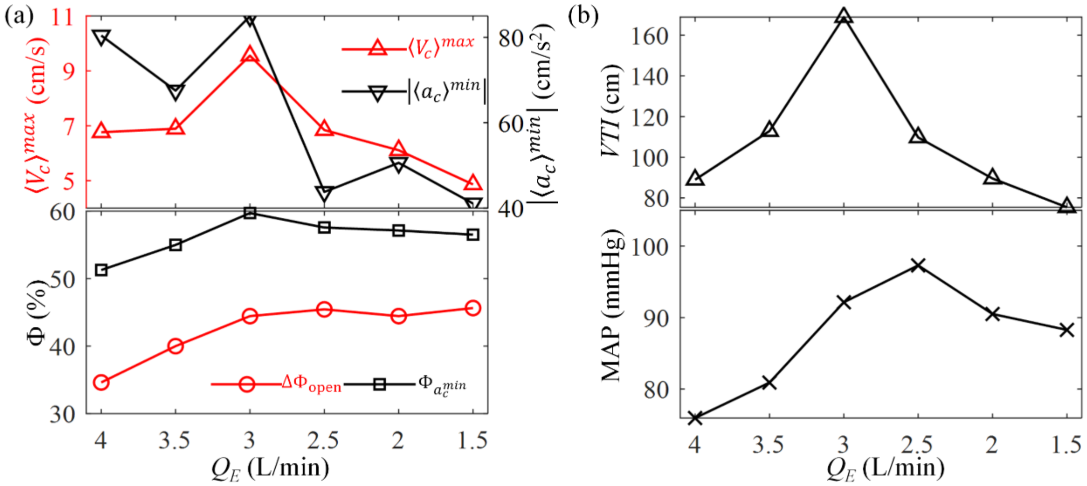

Figure 4-5 (a) Variations of maximum velocity ($\langle V_c\rangle^{\max}$), maximum deceleration magnitude ($|\langle a_c\rangle^{\min}|$), the phase interval between valve opening and closing ($\Delta\Phi_{\text{open}}$), and phase of the maximum deceleration ($\Phi_{a_c^{\min}}$) with Q_E. (b) Variations of velocity-time integral (VTI) over 1min calculated from $\langle V_c\rangle$, and MAP during image acquisition with Q_E.

Statistics of the evolution of V_c, phases of valve opening and closure, flow acceleration, and fluxes are summarized in Figure 4-4 and Figure 4-5. Figure 4-4a and b show the phase evolution of the cross-sectionally averaged velocity, denoted as $\langle V_c\rangle$, and its time derivative, i.e. flow acceleration $\langle a_c\rangle = \partial\langle V_c\rangle/\partial t$, respectively. Figure 4-4a also indicates the phases when the aortic valve begins to open, reaches the maximum opening, and closes. Variations of related flow parameters with Q_E are summarized in Figure 4-5. Included are (Figure 4-5a) the maximum velocity ($\langle V_c\rangle^{\max}$), the magnitude of peak deceleration during the transition to diastole ($|\langle a_c\rangle^{\min}|$), the phase of maximum deceleration ($\Phi_{a_c^{\min}}$), and the phase difference between valve opening and closure ($\Delta\Phi_{\text{open}}$). Several trends are evident. First, as expected, $\langle V_c\rangle$ increases rapidly, i.e. $\langle a_c\rangle>0$, during the early phases of systole, followed by a Q_E-dependent period of high outflow, and then decreases ($\langle a_c\rangle<0$), during the transition to diastole. The phase where the valve starts to open does not change significantly with the ECMO flow rate (Figure 4-4a). Also, except for Q_E=1.5L/min, the phases of maximum velocity (33%) and acceleration (24%) are not influenced appreciably by Q_E. The corresponding phases for 1.5L/min are delayed (26% and 38%, respectively). The phase of valve closure coincides with that of peak negative velocity.

Second, the trends of cardiac outflow can be divided into two ECMO flow rate regimes. For $Q_E \geq 3.0$L/min, the peak velocity (Figure 4-5a) increases as Q_E decreases. After the peak, $\langle V_c \rangle$ plateaus briefly (Figure 4-4a) i.e. the magnitude of $\langle a_c \rangle$ is low (Figure 4-4b), and then it decreases rapidly, resulting in a sharp negative $\langle a_c \rangle$ peak (Figure 4-4b). Furthermore, with decreasing Q_E, the phase interval with an open valve and the phase of peak deceleration increase (Figure 4-5a). Conversely, for $Q_E \leq 2.5$L/min, there is no high velocity plateau during systole (Figure 4-4a), and the peak velocity decreases as Q_E decreases (Figure 4-5a). Moreover, the milder deceleration peaks seem to occur at similar phases and have similar magnitudes, which are almost 2 times smaller than those of the high Q_E cases (Figure 4-5a). The values of $\Delta\Phi_{open}$ also change very little in this range. To evaluate the cumulative effect of these trends, we also calculate the velocity-time integral (VTI) in one minute as a surrogate for the cardiac output by integrating the positive values of $\langle V_c \rangle$ over the period that the valve is open, specifically, $VTI = \frac{Heart\ Rate}{frame\ rate} \sum_{\Delta\Phi_{open}} \langle V_c \rangle \big|_{\langle V_c \rangle > 0}$. Figure 4-5b shows that for $Q_E \geq 3.0$L/min, VTI increases with decreasing Q_E, peaking at 3.0L/min. The corresponding values of MAP during the period of image acquisition (Figure 4-5b) also increase, suggesting that in this Q_E range, the ECMO provides adequate support. In contrast, for $Q_E \leq 2.5$L/min, both the MAP and VTI decline with decreasing ECMO flow rate. These trends along with the hypovolemia that occurs prior to the period of image acquisition while Q_E=2.5L/min indicate that the ECMO flow provides inadequate support. Since the recommended optimal veno-arterial ECMO flow rate should be the lowest level that maintains adequate tissue perfusion (Ostadal et al. 2015), Q_E=3.0L/min appears to be the optimal flow rate for the particular physiological condition of this study.

Chapter 5. Application of Echo-PTV in Cerebral and Ocular Blood Flows

5.1. Background: non-invasive ICP assessment and brain ischemia detection using cerebral and ocular microcirculation

Hydrocephalus involves abnormal cerebrospinal fluid (CSF) accumulation in the brain ventricles (Tully and Dobyns 2014), leading to intracranial hypertension and ventriculomegaly (Shakeri et al. 2008; Kahle et al. 2016). Knowledge of intracranial pressure (ICP) is essential for making decisions about surgical interventions for hydrocephalus patients. However, direct ICP measurements utilizing invasive sensors are rarely adopted due to the risks associated with infection, catheter tract hemorrhage, parenchymal damage, and neurological deficits (Zhang et al. 2017). Prior studies have shown that microvascular flow in several cerebral regions is sensitive to changes in the ICP (Zaharchuk et al. 1999). Moreover, the ocular blood flows are exposed to the ICP via cerebrospinal fluid or optic nerve. Hence, we explore noninvasive methods, where the ICP is inferred from the hemodynamics of cerebral (for neonates) and ocular (for older children and adults) microvessels. Specifically, we use echo-PTV to perform ultrasound localization microscopy for mapping the microcirculation in the brain and eye of hydrocephalic pediatric pig models at varying ICP levels. The study evaluates the correlations between ICP and the combined effects of regional microcirculation density and other hemodynamic parameters. In addition, the lactate-to-pyruvate ratio is obtained to determine cerebral ischemia and correlates with the nondimensionalized cortical microperfusion. Overall, this study aims to provide a noninvasive method for determining ICP in hydrocephalus patients, which can help clinicians make informed decisions about surgical interventions.

5.2. Visualization of the cerebral vasculature

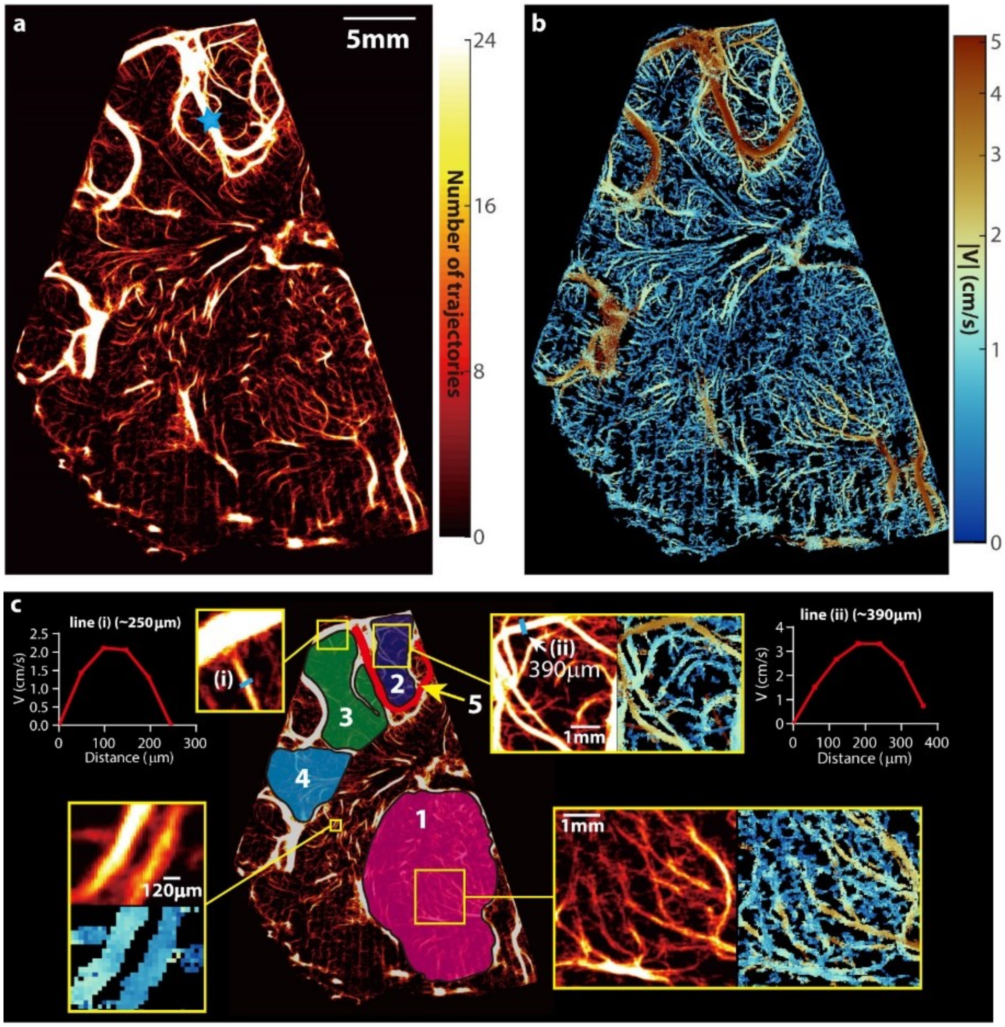
a
5mm
Number of trajectories
24
16
8
0
b
|V| (cm/s)
5
4
3
2
1
0
c
line (i) (~250μm)
V (cm/s)
2.5
2.0
1.5
1.0
0.5
0.0
0
100
200
300
Distance (μm)
(i)
1
2
3
4
5
(ii)
390μm
1mm
line (ii) (~390μm)
V (cm/s)
4
3
2
1
0
0
100
200
300
400
Distance (μm)
120μm
1mm

Figure 5-1 Cerebral vascular map and velocity distribution for piglet #0121 at the baseline ICP. (a) A heatmap of all the trajectories containing at least 4 exposures visualizing the micro- and macro-vascular distributions in a coronal plane. The blue star marks the location of the pulsed-wave Doppler ultrasound measurement. (b) The corresponding time-averaged velocity distribution. (c) Several sub-regions are labeled for statistical analysis of perfusion, including the micro-vessels in the thalamus (#1), several parts of the cortex (#2, #3, and #4), as well as a macro blood vessel (#5). A few regions are magnified to provide a closer view of the current regions of interest. Sample velocity profiles across two different blood vessels are also provided in (c).

Figure 5-1a is a sample visualization of the vascular distributions across the entire hemispherical coronal plane (piglet #0121, Table 2-1) at baseline ICP. The corresponding distribution of time-averaged velocity magnitude is presented in Figure 5-1b. The sample magnified vasculature and velocity distributions for several locations (Figure 5-1c) demonstrate that blood vessels that are separated by ~120μm can be readily distinguished. Moreover, sample time-averaged velocity profiles (Figure 5-1c) have parabolic profiles with a peak magnitude of 2.2cm/s and 3.4cm/s at the center of a 250μm vein, and a 390μm artery, respectively. The arteries are readily identified by the flow pulsatility during the cardiac cycle. The venal values are consistent with previously published data (Piechnik et al. 2008). The present arterial velocity for MAP=68mmHg is lower than simulated values (Piechnik et al. 2008) which are based on a steady 100mmHg intravascular pressure at the entrance to a 2mm artery, as expected. To facilitate the analysis of regional perfusion differences in response to ICP changes, several areas are selected and labeled in Figure 5-1c. Included are a macro blood vessel (region #5), the thalamus (region #1), and the cortex divided into three sub-regions (regions #2-4) based on their locations relative to macro-vessels. For the thalamus and cortex, taking advantage of the high spatial resolution features of the vascular map, the areas occupied by macro-vessels with in-plane widths of more than 400μm (corresponding to the second-order branches of the middle cerebral artery in piglets (Eriksen et al. 2016)) are excluded (Figure 5-1c, maximum width is ~390μm), and the analyses are focused on the micro-vessels. Initially, these microvascular regions are labeled manually. Subsequently, an automated procedure based on the vesselness filter (Jerman et al. 2016) has been implemented for defining the same microvascular regions of interest, by detecting and excluding vessels with a diameter equal to or larger than 400μm. The flow parameters (discussed below) obtained for cortical regions #2-4 using the two methods are statistically identical. Hence, the current microvascular flow evaluations are not affected by the values of major vessels associated with region selections. Only macro vessel #5 is used since it is the only one that appears consistently for all piglets, presumably owing to slight variations in the location of the imaging plane. A visual demonstration of the changes to the vascular map and velocity distribution caused by elevated ICP for the same piglet is provided in Figure 5-2a. In the cortex, the number of micro-vessels with blood flow and the velocity in each vessel gradually decreases as the ICP increases, with a particularly noticeable reduction from 40 to 46mmHg. The same trends occur in macro vessel #5. In contrast, the changes in the thalamus appear to be relatively small up to an ICP of 30mmHg. However, once the pressure is increased to 40 and then to 46mmHg, there is a reduction in microcirculation in the thalamus as well. Quantification of these trends is discussed in the following section.

5.3. Quantification of the impact of elevated ICP on the cerebral blood flow

Figure 5-2 Visualization and quantification of the influence of increasing ICP on cerebral perfusion. (a) Sample visualizations of cerebral blood vessels (top row) and the corresponding velocity distributions (bottom row) of piglet #0121 with increasing ICP. (b-d) Relationships between the ICP and the Cerebral Microcirculation (CMC, original cohort) parameter of the thalamus (b), cortical subregion #2 (c), and all three cortical subregions combined (d, CMC_{cort}). (e) Relationships between the ICP and the time-averaged velocity (V_5) in the macro blood vessel #5 at the point marked with a blue star in (a). For (b-e) data are presented as mean ± SD, where the error bars show the temporal standard deviations of CMCs or V_5 over n=20 cardiac phases. The curves are least-square fitted quadratic functions, with the corresponding coefficient of determination (R^2) shown on each plot. Also presented are the correlation coefficients (r) and the corresponding P values between the CMCs or V_5 and the ICP. (Figures attached on the next page.)

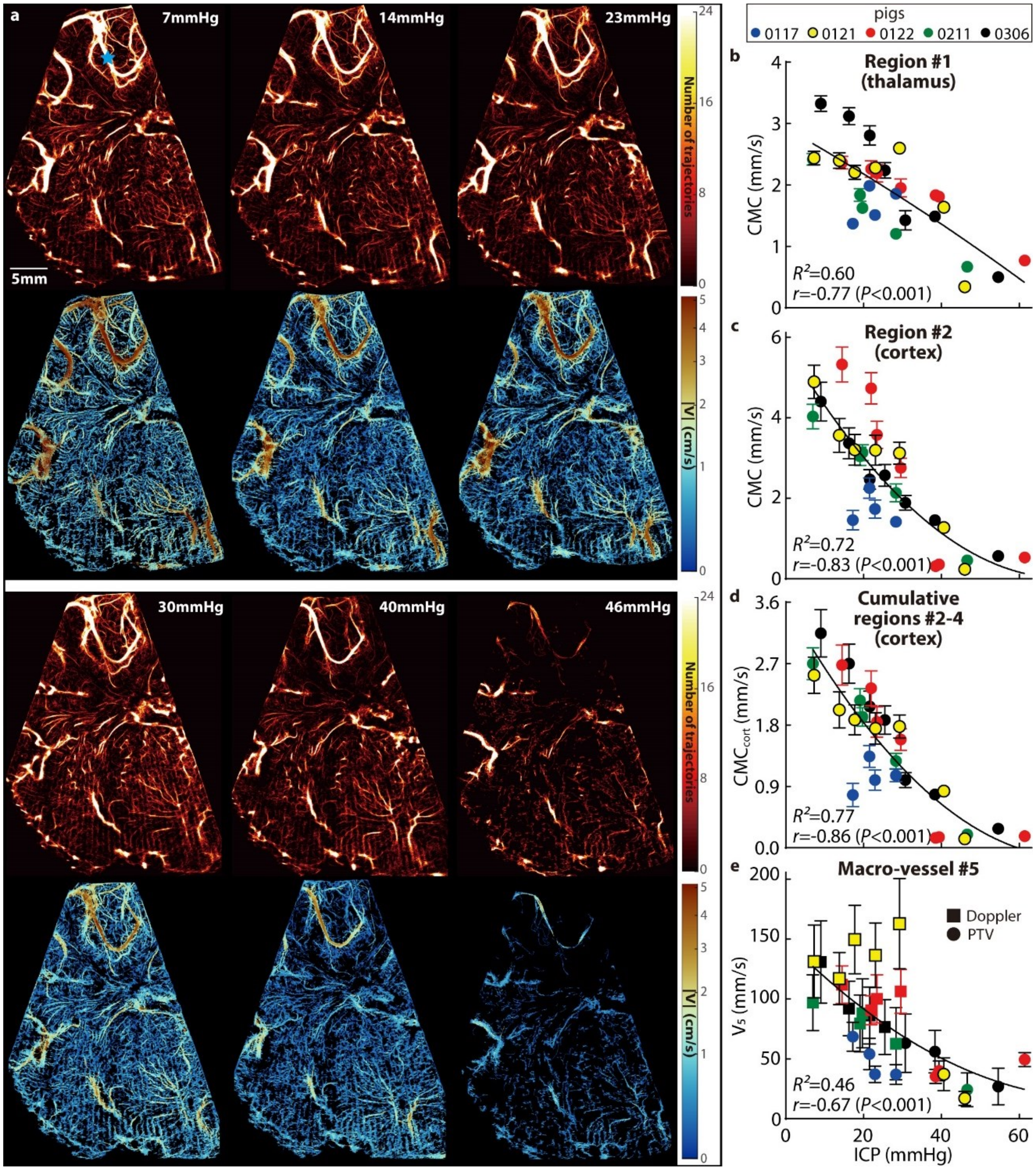

Two parameters have been adopted as surrogates for the cerebral perfusion: (i) The CMC parameter is calculated by summing the time-averaged velocity (in mm/s) in each pixel of the area occupied by micro-vessels (<400μm) and dividing the result by the total area of these regions (i.e., all pixels, including those with zero values). Hence, the CMC accounts for the changes to the density of micro-vessels and the velocity in them due to elevated ICP. Note that CMC values are inherently lower than the spatio-temporal averaged velocity since the CMC accounts for areas without vessels. (ii) The time-averaged velocity magnitude, V_5 (mm/s), is utilized for characterizing the flow in macro blood vessel #5. Owing to the limitations in the maximum velocity that can be measured based on CEUS data acquired at 48 frames/s, V_5 is based on the PTV data when all instantaneous speeds over the cardiac cycle are lower than 11 cm/s, and pulsed-wave Doppler ultrasound data recorded at the same location (Figure 5-2a, blue star) are used for cases with higher speeds. The CMCs for all the piglets of the original cohort (Table 2-1) in the thalamus (Figure 5-2b), cortical subregion #2 (Figure 5-2c), cumulative cortical CMC combining regions #2, 3, and 4 (CMC_{cort}, Figure 5-2d), and V_5 (Figure 5-2e) decrease with increasing ICP. The error bars in Figure 5-2b-e represent the temporal standard deviation of CMCs or V_5 for each case. The magnitudes of the (negative) correlation coefficients between ICP and CMCs are larger than 0.77 ($P<0.001$), and that between the ICP and V_5 is 0.67 ($P<0.001$). The coefficient of determination (R^2) for the shown least square parabolic fits falls in the 0.60 to 0.77 range for the CMCs, and 0.46 for the V_5.

Aiming to improve the collapse of the data, hence obtaining higher R^2 for better evaluation of ICP levels, effects of hemodynamic parameters, which are expected to affect cerebral perfusion, should also be accounted for in calculations. Based on the data of the original cohort (Table 2-1), plots of ICP and CMC_{cort} vs. the mean arterial pressure (MAP), cerebral perfusion pressure (CPP=MAP-ICP), systolic and diastolic pressures (SBP and DBP), and pulse pressure (PP=SBP-DBP) are presented in Figure 5-3a&b, all showing weak or poor correlations. Yet, plots with combinations of parameters, namely MAP/ICP, PP/ICP, and (PP-ICP)/MAP appear to have stronger correlations (Figure 5-3c&d). Accordingly, Figure 5-4a summarizes the highest values of R^2 obtained by least-square fitting several functions to the CMC (or V_5) vs. hemodynamic or combined parameters for each cerebral region, confirming that these combined variables yield higher R^2. Subsequently, isolating ICP from these relationships leads to CMC/MAP, CMC/PP, and PP-(0.17CMC-0.29)MAP (the constants 0.17 and 0.29 are based on the curve fit in Figure 5-3d), as likely candidates for obtaining collapsed trends. As Figure 5-4b demonstrates, the latter two fits vs. ICP have significantly higher R^2 ($P<0.01$ and $P<0.001$ respectively) compared to the CMC vs. ICP relationship. Values of R^2 exceeding 0.8 are obtained for the cortical microvascular regions, while lower values are obtained for the thalamus or macro-vessel (Figure 5-4b). For the data of the original cohort, plots of CMC/PP and V_5/PP vs. ICP are presented in Figure 5-4c-i by colored symbols, each showing a parabolic curve fit and corresponding values of R^2. Owing to its highest R^2 and correlation $CMC_{cort}/PP=5.2\times10^{-5}(ICP)^2-6.1\times10^{-3}(ICP)+0.18$ could be considered a potential functional relationship for evaluating the ICP (Figure 5-4c). This parabolic function is tested by the validation data (Figure 5-4c, hollow symbols). While the decrease in CMC_{cort}/PP persists, results are more scattered, resulting in R^2 decreasing from 0.87 to 0.72 for all data (original + validation). The primary discrepancy occurs for ICP>40mmHg, where the majority of the original cases are ischemic, while only one of the validation cases involves ischemia (further discussion follows). Accordingly, the validation CMCs are higher than the original ones in this ICP range. A comparison of the relative errors in ICP prediction, i.e., the difference between the predicted and measured ICP level divided by the measured ICP, between the original and validation sets are presented in Figure 5-5a. It shows that the relative validation errors for ICP=10 (i.e.,10±5) mmHg are higher than those of the original data, while there are no statistical differences between the original and validation data for ICP>10mmHg. The validation data indicates that the ICP can be predicted within 4.2mmHg at low to moderate pressure ($0<ICP<35$), and within 13.8mmHg for ICP>40mmHg. As for the macro-vessel, the scatter in the original data is caused primarily by piglet #0121. If the results for this pig are removed, R^2 for V_5/PP increases from 0.51 to 0.77. However, adding the validation cohort data reduces the R^2 to 0.08 for all data, and 0.01 for all data with pig #0121 excluded.

In exploring possible reasons for the differences in trends between the original and validation cohorts, especially at high ICP, we have found that the MAP for the validation cohort is generally higher than that of the original piglets by 25mmHg (Figure 5-3a). Hence, taking the effect of MAP into account has led to the following linear relationship (Figure 5-4b&j):

$$\text{ICP}=\text{PP}-(0.17\text{CMC}_{\text{cort}}-0.29)\text{MAP}+0.08 \tag{5.1}$$

This linear relationship has an R^2 of 0.91 for the original CMC_{cort}, and 0.84 for the combined original and validation cohorts. The corresponding relative error in ICP prediction between the original and validation cohorts is insignificant for all ICP levels. The absolute errors for the validation data vary from 3.1mmHg for ICP=0-35mmHg to 7.8mmHg for ICP>40mmHg. Hence, even with a validation cohort with higher MAP, the linear relationship presented in Eqn. (5.1) provides a reasonable prediction of the ICP level. In contrast, while adding the effect on MAP makes the validation and original data of V_5 overlap (Figure 5-4p), the results are scattered and R^2 for the combined data is only 0.12.

Note, the trends of the perfusion with increasing ICP differ among the cerebral regions. The rates of perfusion decrease are demonstrated by the nondimensionalized slopes of the fitted curves, namely, $k=\left[d(\text{CMC/PP})/d(\text{ICP})\right]_{average}\times(\text{ICP}\times\text{PP/CMC})_{ref}$, where the subscript 'average' refers to the average slope in the 8-40mmHg ICP range, and 'ref' to values at ICP=8mmHg, i.e., the average baseline ICP for all pigs. Results for each region are presented in Figure 5-4c-h. They indicate that rates of perfusion reduction in the cortical regions are similar and higher than that in the thalamus (by 38%). The cortical regions appear to be more vulnerable to intracranial hypertension.

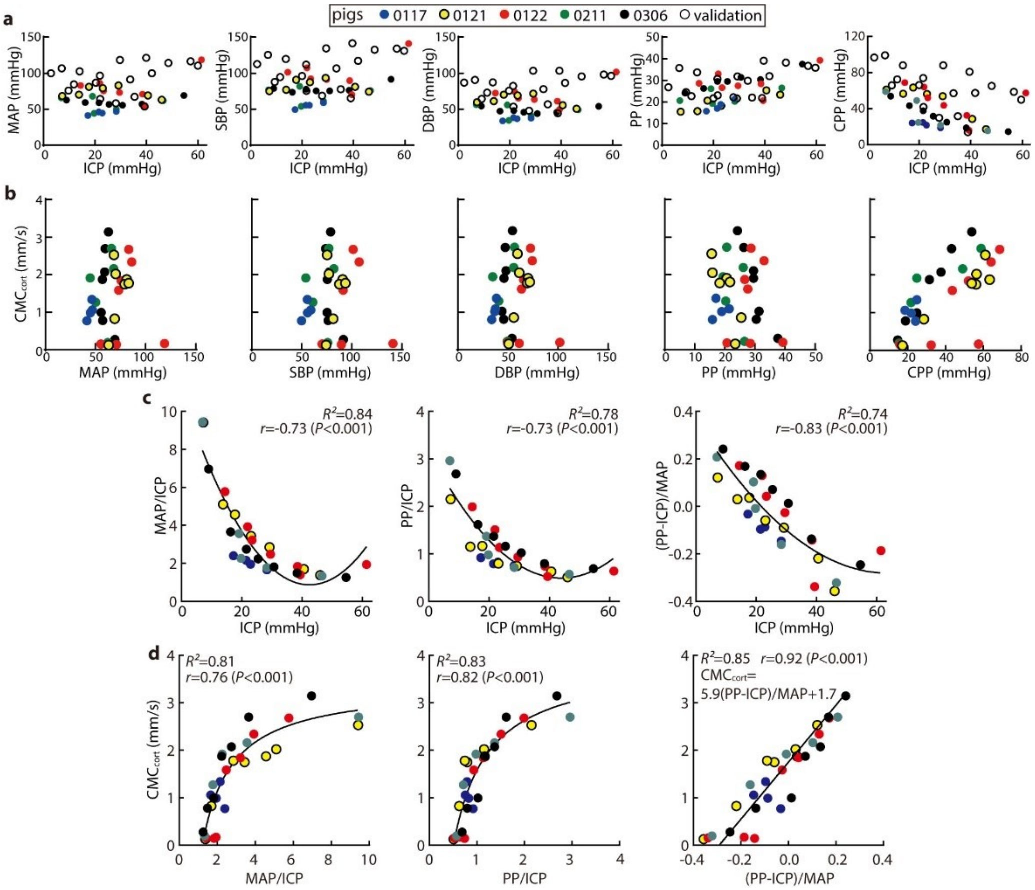

Figure 5-3 Exploring different combinations of perfusion and hemodynamic parameters aimed at improving the correlation with the ICP. (a) Relationships between hemodynamic parameters and ICP for all the piglets. From left to right: MAP, systolic (SBP) and diastolic blood pressure (DBP), pulse pressure (PP=SBP-DBP), and cerebral perfusion pressure (CPP=MAP-ICP). (b) Variations of the $\mathrm{CMC_{cort}}$ with hemodynamic parameters. (c) Variations of combinations of hemodynamic parameters with ICP. (d) Variations of $\mathrm{CMC_{cort}}$ with combinations of hemodynamic parameters. For (c, d), each plot contains a least square fitted curve along with its R^2, as well as r and P.

Figure 5-4 Combining the perfusion parameters with hemodynamic variables to obtain highly correlated functional relationships for the assessment of ICP. (a) A heatmap of R^2 of the least-squared fits between a series of hemodynamic parameters and CMC (or V_5). (b) A heatmap of R^2 of the least-squared fits between the ICP and the combined hemodynamic-perfusion parameters. Here, two-way ANOVA multiple comparison results with Benjamini-Hochberg correction are also demonstrated, where 'ns' indicates P=0.72, '**' P=0.0016, and '***' P=0.0001. (c-i) Variations of CMC/PP with ICP, in the: (c) combined cortical regions (#2-4); (d) thalamus (#1), and cortical subregions #2 (e), #3 (f), and #4 (g); (h) combined thalamus and cortical data (#1-4); and (i) macro vessel. Corresponding values of R^2 for the parabolic curve fit, as well as r and P for the two-tailed Pearson correlation, are provided for each plot. (j-p) Trends of PP-(0.17CMC-0.29)MAP with ICP in the: (j) combined cortical regions (#2-4); (k) thalamus (#1), and cortical subregions #2 (l), #3 (m), and #4 (n); (o) combined thalamus and cortical data (#1-4); and (p) macro vessel. Here, the corresponding R^2 for the fitting, as well as r and P for the two-tailed Pearson correlation are shown. For (c-p) the functions are developed based on the original cohort (colored symbols) and validated by validation data (hollow symbols). Subscript 'ori' denotes the values based on the original cohort, while 'all' denotes the values based on original and validation cohorts combined. (Figures attached on the next page.)

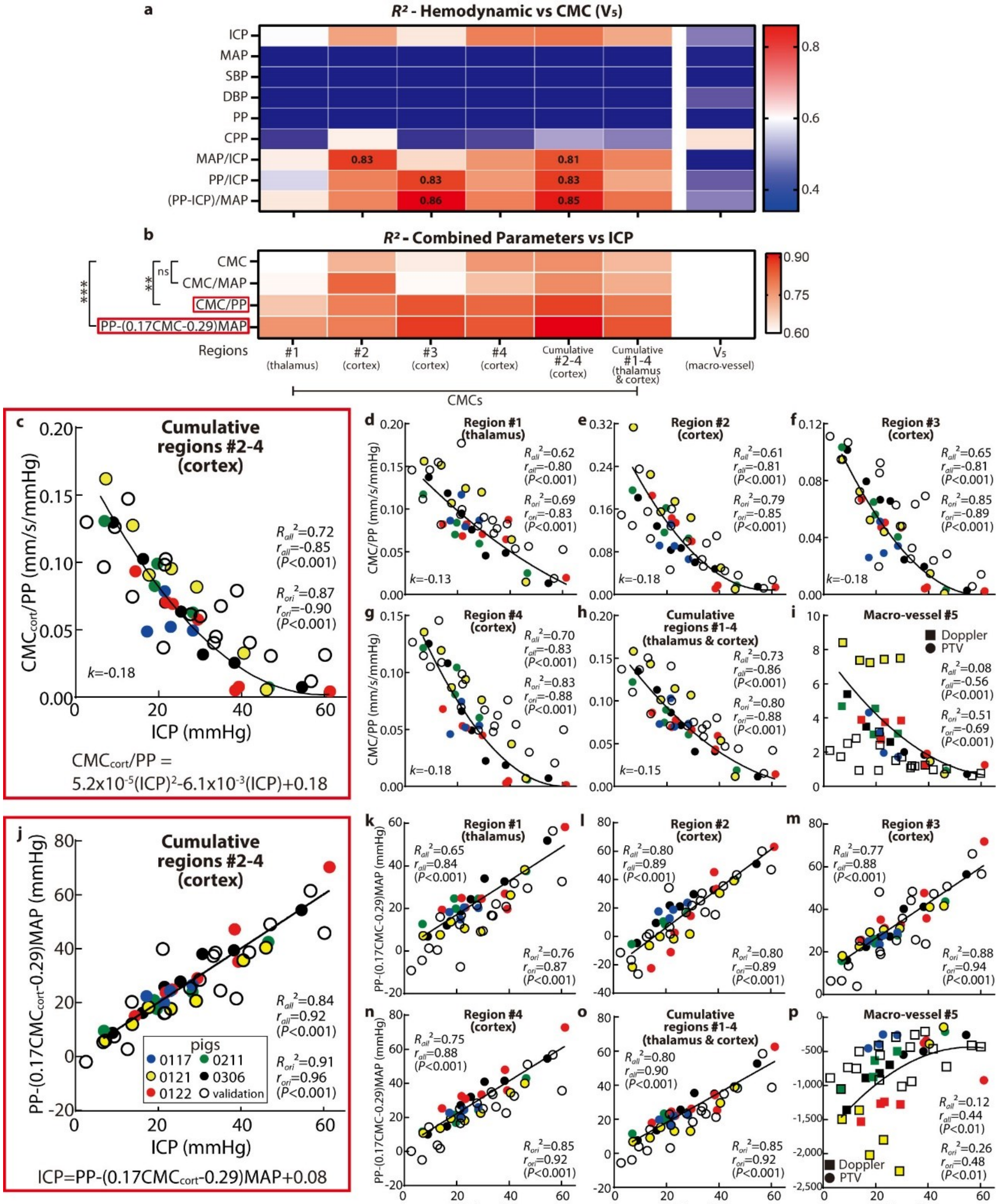
a
R² - Hemodynamic vs CMC (V₅)
ICP
MAP
SBP
DBP
PP
CPP
MAP/ICP
PP/ICP
(PP-ICP)/MAP
0.83
0.81
0.83
0.83
0.86
0.85
0.8
0.6
0.4
b
R² - Combined Parameters vs ICP
CMC
CMC/MAP
CMC/PP
PP-(0.17CMC-0.29)MAP
ns
**
***
0.90
0.75
0.60
Regions
#1 (thalamus)
#2 (cortex)
#3 (cortex)
#4 (cortex)
Cumulative #2-4 (cortex)
Cumulative #1-4 (thalamus & cortex)
V₅ (macro-vessel)
CMCs
c
Cumulative regions #2-4 (cortex)
CMCcort/PP (mm/s/mmHg)
ICP (mmHg)
R_all²=0.72
r_all=-0.85
(P<0.001)
R_ori²=0.87
r_ori=-0.90
(P<0.001)
k=-0.18
CMCcort/PP = 5.2x10⁻⁵(ICP)²-6.1x10⁻³(ICP)+0.18
d
Region #1 (thalamus)
R_all²=0.62 r_all=-0.80 (P<0.001)
R_ori²=0.69 r_ori=-0.83 (P<0.001)
k=-0.13
e
Region #2 (cortex)
R_all²=0.61 r_all=-0.81 (P<0.001)
R_ori²=0.79 r_ori=-0.85 (P<0.001)
k=-0.18
f
Region #3 (cortex)
R_all²=0.65 r_all=-0.81 (P<0.001)
R_ori²=0.85 r_ori=-0.89 (P<0.001)
k=-0.18
g
Region #4 (cortex)
R_all²=0.70 r_all=-0.83 (P<0.001)
R_ori²=0.83 r_ori=-0.88 (P<0.001)
k=-0.18
h
Cumulative regions #1-4 (thalamus & cortex)
R_all²=0.73 r_all=-0.86 (P<0.001)
R_ori²=0.80 r_ori=-0.88 (P<0.001)
k=-0.15
i
Macro-vessel #5
Doppler
PTV
R_all²=0.08 r_all=-0.56 (P<0.001)
R_ori²=0.51 r_ori=-0.69 (P<0.001)
CMC/PP (mm/s/mmHg)
j
Cumulative regions #2-4 (cortex)
PP-(0.17CMCcort-0.29)MAP (mmHg)
ICP (mmHg)
R_all²=0.84 r_all=0.92 (P<0.001)
R_ori²=0.91 r_ori=0.96 (P<0.001)
pigs
0117
0211
0121
0306
0122
validation
ICP=PP-(0.17CMCcort-0.29)MAP+0.08
k
Region #1 (thalamus)
R_all²=0.65 r_all=0.84 (P<0.001)
R_ori²=0.76 r_ori=0.87 (P<0.001)
l
Region #2 (cortex)
R_all²=0.80 r_all=0.89 (P<0.001)
R_ori²=0.80 r_ori=0.89 (P<0.001)
m
Region #3 (cortex)
R_all²=0.77 r_all=0.88 (P<0.001)
R_ori²=0.88 r_ori=0.94 (P<0.001)
n
Region #4 (cortex)
R_all²=0.75 r_all=0.88 (P<0.001)
R_ori²=0.85 r_ori=0.92 (P<0.001)
o
Cumulative regions #1-4 (thalamus & cortex)
R_all²=0.80 r_all=0.90 (P<0.001)
R_ori²=0.85 r_ori=0.92 (P<0.001)
p
Macro-vessel #5
R_all²=0.12 r_all=0.44 (P<0.01)
R_ori²=0.26 r_ori=0.48 (P<0.01)
Doppler
PTV
PP-(0.17CMC-0.29)MAP (mmHg)
ICP (mmHg)

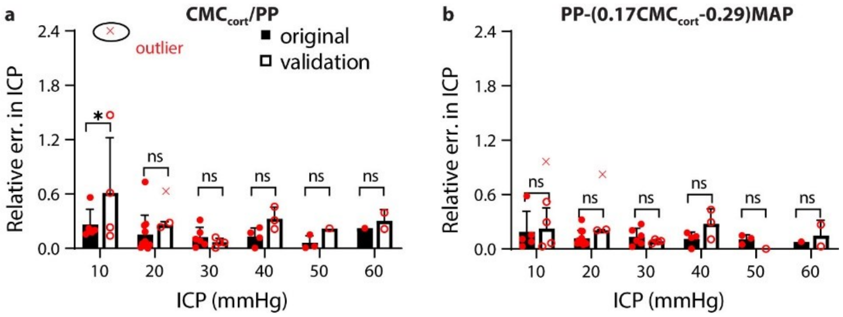

Figure 5-5 The relative errors in ICP prediction based on the (a) parabolic function in Figure 5-4c and (b) linear function in Figure 5-4j for the original (closed bar) and validation (open bar) data. For (a, b), the bar height denotes the mean value with the error bar showing the standard deviation. Here, two-way ANOVA multiple comparison results with Benjamini-Hochberg correction are also demonstrated, where 'ns' *P*>0.05, '*' *P*<0.05, '**' *P*<0.01, and '***' *P*<0.001.

5.4. Microdialysis and cerebral microcirculation during ischemia

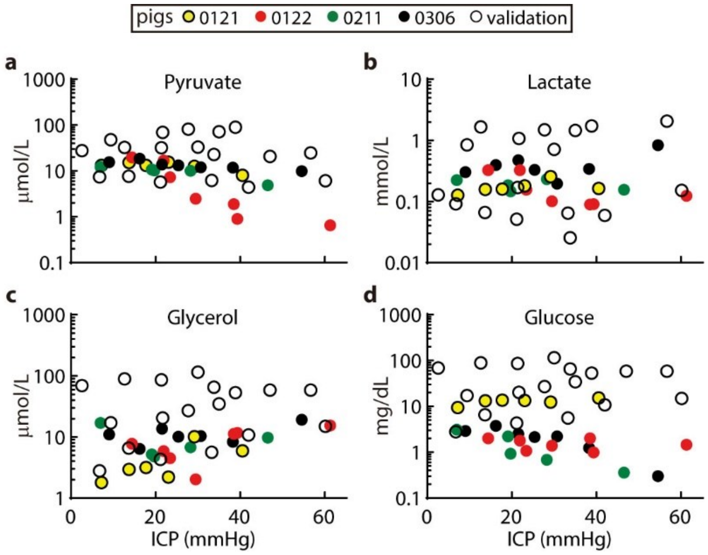

Figure 5-6 Microdialysis results. (a) Pyruvate. (b) Lactate. (c) Glycerol. (d) Glucose.

Cerebral microdialysis data have been obtained for seven of the eight piglets (Table 2-1), and their relationships with ICP are presented in Figure 5-6. As a characterization of the relationship between aerobic and anaerobic metabolism, a lactate-to-pyruvate ratio exceeding 30 has been linked to cerebral ischemia (Purins et al. 2012). Figure 5-7a shows the variations of L/P with ICP for the current study. This trend is consistent with the results of a previous study (Zoremba et al. 2007) (Figure 5-7a). The relationships between cerebral perfusion and L/P are plotted in Figure 5-7b. Here, from the perspective of fluid mechanics, the cortical microcirculation data are presented in a nondimensional form that compares the dynamic pressure of the blood flow to the pulse pressure, i.e., $\rho(\mathrm{CMC}_{\mathrm{cort}})^2/\mathrm{PP}$, where ρ is the average density of blood. A corresponding comparison to the ICP nondimensionalized by the MAP is presented in Figure 5-7c, where the values of $\rho(\mathrm{CMC}_{\mathrm{cort}})^2/\mathrm{PP}$ for original and validation cohorts collapse. Results of nondimensionalized perfusion parameters for other regions are provided in Figure 5-8. A few trends are evident in Figure 5-7a-c: (i) All the six cases (five original and one validation) with $\rho\mathrm{CMC}_{\mathrm{cort}}^2/\mathrm{PP}<10^{-7}$, which deviate from the rest of the data for at least one order of magnitude, involve cerebral ischemia. Note that for all of them, $\mathrm{ICP}/\mathrm{MAP} \geq 0.5$. (ii) Among the other 37 cases, where $\rho\mathrm{CMC}_{\mathrm{cort}}^2/\mathrm{PP}>10^{-7}$, 92% has L/P smaller than 30, i.e., they are considered non-ischemic. Hence, the non-dimensional cortical CMC could be used for detecting ischemia. Values smaller than 10^{-7} show 100% probability of ischemia while those larger than 10^{-7} indicate with 92% likelihood that they do not involve ischemia. In the macro vessel (Figure 5-7d), even though the rate of perfusion reduction appears to be increased for both original and validation cohorts when $\mathrm{ICP}/\mathrm{MAP} \geq 0.5$, their values are scattered. As a visualization of the reduction in perfusion during ischemia, Figure 5-7e and f compare the vasculature maps as L/P increases from the baseline level to L/P=85 for piglet #0306. In this sample, there is a 99.5% reduction in nondimensional cortical microcirculations and 97.3% in nondimensional V_5. Moreover, since $\mathrm{ICP}/\mathrm{MAP}$ exceeds 0.5 for all of the ischemia cases, with similar MAP levels (P=0.25) between ischemia and non-ischemia cases in this ICP range, the significant reduction in micro-perfusion might have been caused by the collapse and/or deformation of the micro-vessels owing to the elevated ICP.

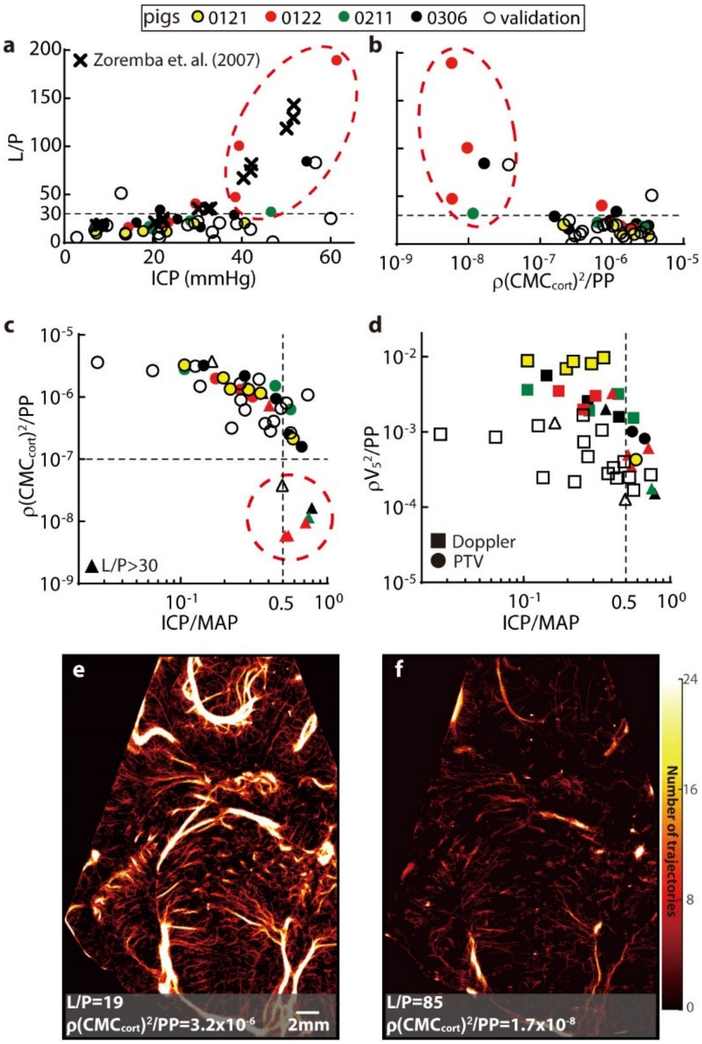

Figure 5-7 Comparison to microdialysis data showing a drastic reduction in perfusion once cerebral ischemia occurs. (a) Trends of lactate-to-pyruvate ratio (L/P) with increasing ICP for the current experiment (circles) and previously reported results (cross, Zoremba et al. 2007). The dashed line at L/P=30 has been suggested as the threshold for cerebral ischemia (Purins et al. 2012). (b) Trends of L/P vs. the nondimensionalized cortical micro-perfusion parameter $\rho(CMC_{cort})^2/PP$. (c) Trends of $\rho(CMC_{cort})^2/PP$ with ICP/MAP in logarithmic scales. In (a-c), the same group of encircled cases is identified to have cerebral ischemia, all occurring at $ICP/MAP \geq 0.5$. (d) Variations of $\rho V_5^2/PP$ with ICP/MAP . (e and f) A sample comparison of the baseline (e) and ischemia (f) cases for piglet #0306 showing the omnipresent sharp reduction in perfusion during ischemia.

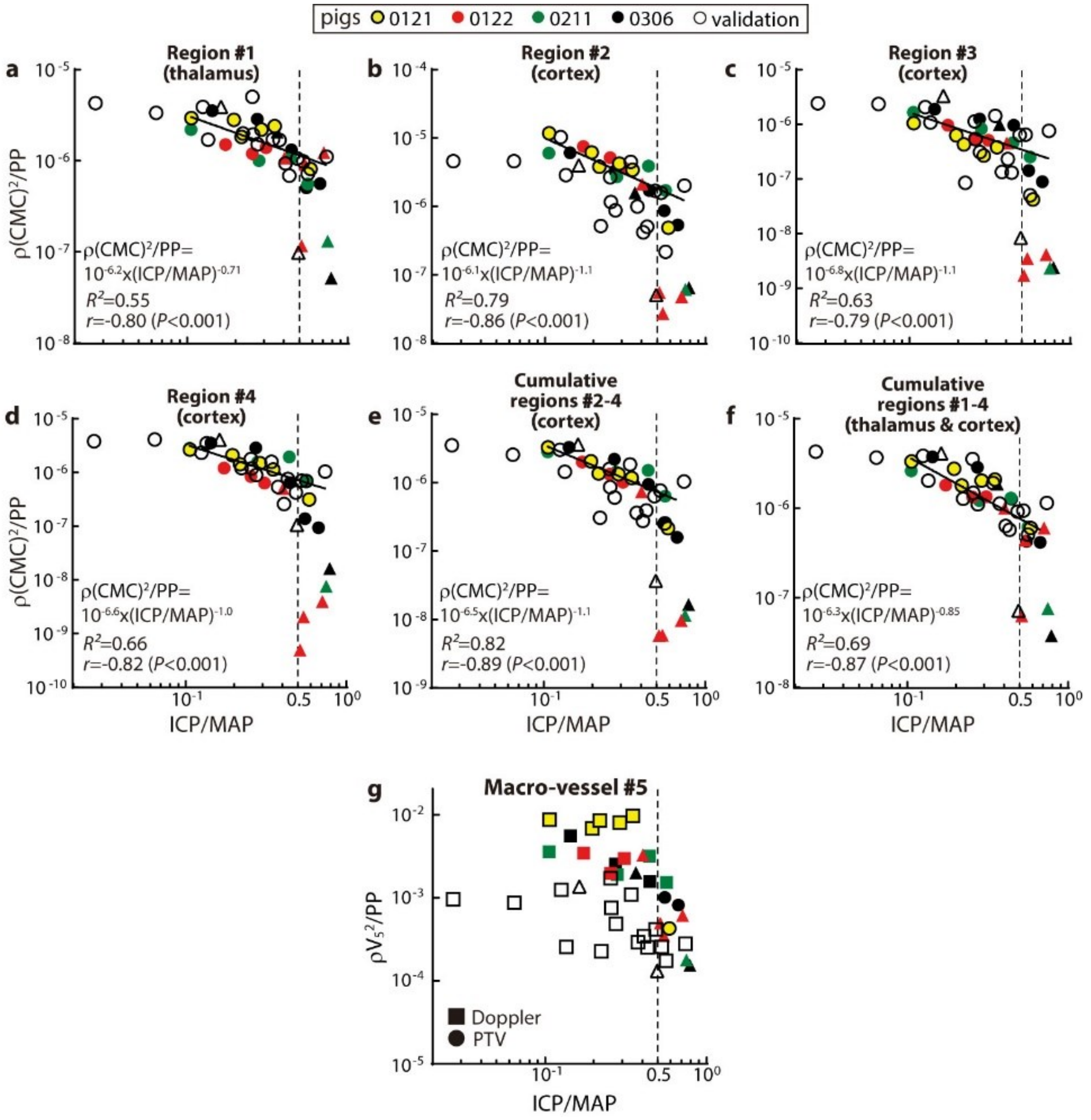

Figure 5-8 Relationships between nondimensional perfusion parameters and ICP/MAP in different parts of the brain. The locations of measurements include microcirculation in the: (a) Thalamus, and cortical regions #2 (b), 3 (c), and 4 (d), as well as: (e) the combined cortical microcirculation in regions #2-4, (f) The combined microcirculation in regions #1-4, and (g) the velocity in macro blood vessel #5. All cases whose L/P>30 are marked in the triangle. In (a-f), the fitted functions are based on the data of the original cohort, along with their R^2, the correlation coefficients and P values for the two-tailed Pearson correlation.

5.5. The impact of ICP on the pulsatility of cerebral blood flow

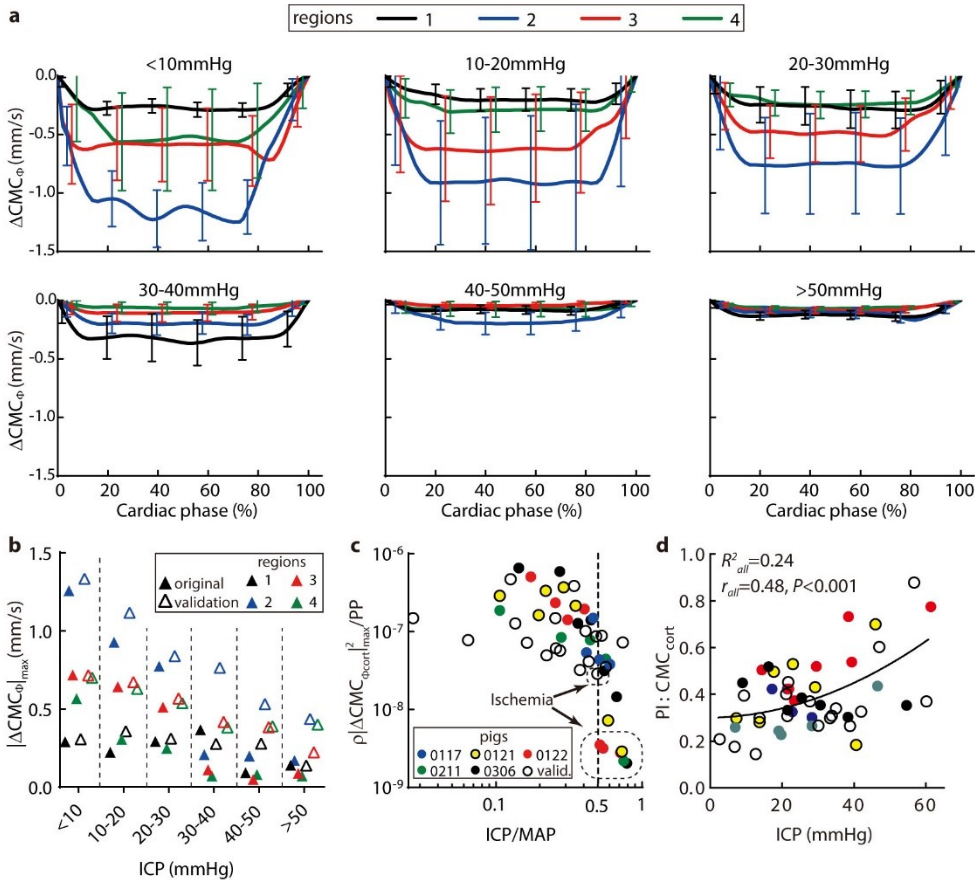

Figure 5-9 Influence of increasing ICP on the pulsatility of the micro-perfusion. (a) Variations with the cardiac phase of the phase-averaged CMC (over 250 cardiac cycles) after subtracting the systolic value ($\Delta\mathrm{CMC}_{\Phi}$). Data are presented as mean ± SD, where error bars indicate the standard deviations among cases. (b) Trends of the maximum cyclic variations in micro-perfusion ($|\Delta\mathrm{CMC}_{\Phi}|_{\max}$) with increasing ICP for different brain regions. (c) The nondimensional cyclic variations in CMC for the cortex regions combined, $\rho|\Delta\mathrm{CMC}_{\Phi\mathrm{cort}}|_{\max}^{2}/\mathrm{PP}$, plotted vs. $\mathrm{ICP/MAP}$. The encircles cases correspond to the ischemia cases marked in Figure 5-7. (d) The pulsatility index for the $\mathrm{CMC}_{\mathrm{cort}}$. Corresponding values of R^2 for the parabolic curve fit, as well as r and P (0.0006) for the two-tailed Pearson correlation, are provided.

Tracking of the bubbles also enables measurements of perfusion variations at different phases of the cardiac cycle. The phase-averaged CMCs (denoted as CMC_{Φ}) are determined by dividing each cardiac cycle into 20 phases based on the ECG signal, and averaging the values corresponding to each phase over 250 cycles. Figure 5-9a shows CMC_{Φ} of each region for increasing ICP range. Results for all piglets are averaged, with the error bars showing the standard deviations among them. To focus on the cyclic variations, the peak value is subtracted from each data point, hence the results are denoted as $\Delta\mathrm{CMC}_{\Phi}$. Figure 5-9b summarizes the trends of $\Delta\mathrm{CMC}_{\Phi}$ by comparing the maximum values ($|\Delta\mathrm{CMC}_{\Phi}|_{\max}$). For the original cohort, in the cortical regions, $|\Delta\mathrm{CMC}_{\Phi}|_{\max}$ decreases gradually at varying rates as the ICP is increased up to 30mmHg, and then drops sharply at higher pressures. Conversely, in the thalamus, where the cyclic variations are initially lower than the cortical levels, the cyclic variations appear to remain at a similar level up to 40mmHg, and then decrease. The flow oscillation amplitudes for the validation cohort in these regions show the same trend (Figure 5-9b), where they decrease with increasing ICP. However, since there is only one ischemia case for the validation cohort and the MAP is generally higher, there are no sharp decreases when ICP>30mmHg. Further insights can be derived by non-dimensionalizing the cumulative cortical values (i.e., $\rho|\Delta\mathrm{CMC}_{\Phi\mathrm{cort}}|_{\max}^{2}/\mathrm{PP}$) and plotting them with $\mathrm{ICP}/\mathrm{MAP}$ in Figure 5-9c. Here, the cortical values for all piglets collapse and decrease at a growing rate with increasing ICP/MAP. For $\mathrm{ICP}/\mathrm{MAP} \geq 0.5$, the values for the ischemia cases in the original cohort (encircled in Figure 5-9c) are significantly lower ($P<0.01$) than those of the non-ischemia cases in the same ICP range, but that for the validation cohort is not. Since the magnitudes of PP for the ischemia cases, which drive the cyclic variations, are not different ($P=0.19$) from those of the non-ischemia ones (Figure 5-3), the reduced flow oscillation amplitudes indicate an increase in the blood flow resistance, consistent with the severe reduction in the mean micro-perfusion. The values of the pulsatility index ($\mathrm{PI}=|\Delta\mathrm{CMC}_{\mathrm{cort}}|_{\max}/\mathrm{CMC}_{\mathrm{cort}}$) are presented in Figure 5-9d, with baseline magnitudes ranging between 0.1 to 0.4, consistent with previous results for the cortical micro-vessels (Rashid et al. 2012). Moreover, the PI increases with ICP (r=0.48, P<0.001), in agreement with prior doppler-based studies (Ungersböck et al. 1995), but there is a considerable scatter in the data (R^2=0.24). The decreasing $|\Delta\mathrm{CMC}_{\Phi}|_{\max}$ and increasing PI also indicate that the changes to the mean flow are stronger than the pulsatility when ICP increases.

5.6. Quantification of the impact of elevated ICP on the ocular blood flow

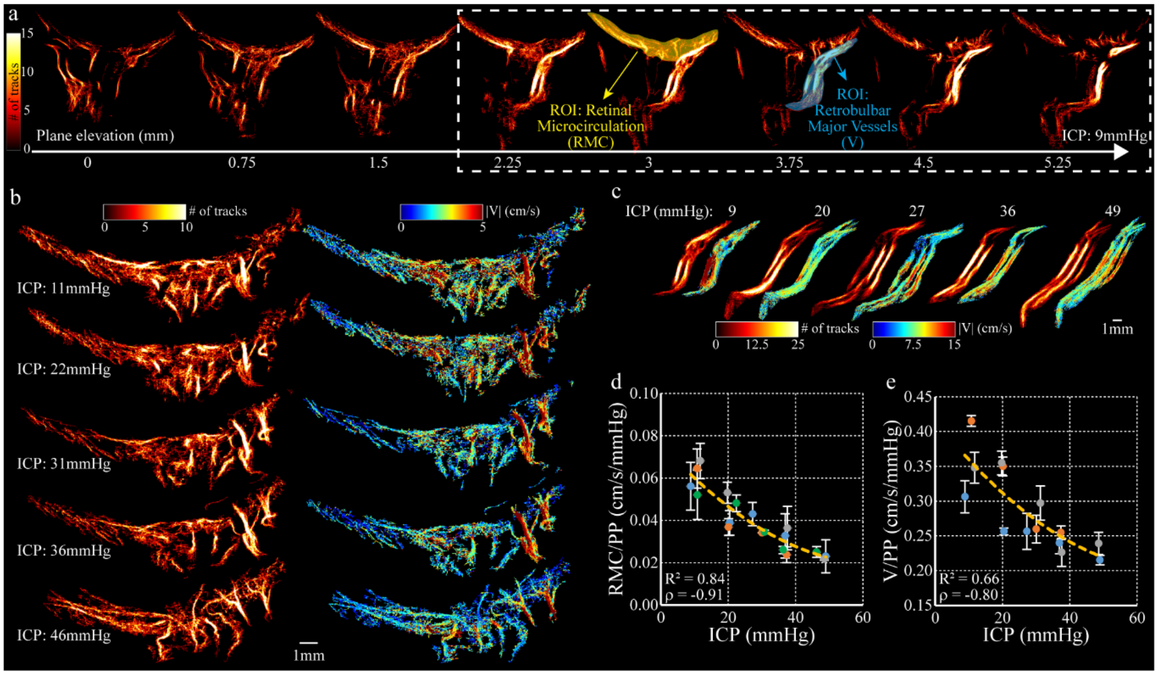

a
15
10
5
0
# of tracks
Plane elevation (mm)
0
0.75
1.5
2.25
3
3.75
4.5
5.25
ROI: Retinal Microcirculation (RMC)
ROI: Retrobulbar Major Vessels (V)
ICP: 9mmHg
b
# of tracks
0 5 10
|V| (cm/s)
0 5
ICP: 11mmHg
ICP: 22mmHg
ICP: 31mmHg
ICP: 36mmHg
ICP: 46mmHg
1mm
c
ICP (mmHg): 9 20 27 36 49
# of tracks
0 12.5 25
|V| (cm/s)
0 7.5 15
1mm
d
RMC/PP (cm/s/mmHg)
0.10
0.08
0.06
0.04
0.02
0.00
$R^2 = 0.84$
ρ = -0.91
0 20 40 60
ICP (mmHg)
e
V/PP (cm/s/mmHg)
0.45
0.40
0.35
0.30
0.25
0.20
0.15
$R^2 = 0.66$
ρ = -0.80
0 20 40 60
ICP (mmHg)

Figure 5-10 Variations of ocular vascular blood flow with increasing ICP. (a) Sample vasculatures in eight parallel ocular axial planes at ICP=9mmHg. (b) Visualization of the effect of increasing ICP on the retinal microvascular heatmaps (left) and the average blood flow velocity (right). (c) Heatmaps (left) and velocity (right) in the retrobulbar major vasculature with increasing ICP. (d) The Retinal Microcirculation Coefficient (RMC) scaled by the PP plotted vs. the ICP. (e) Variations of the mean velocity in the retrobulbar major vessels scaled by PP with increasing ICP. In d and e, each color indicates a different pig, and the yellow curve is a parabolic least-square fit to the data. The corresponding R^2 and r are indicated on each plot.

Figure 5-10a displays sample heatmaps of bubble tracks showing the ocular blood vessels in eight parallel axial planes at ICP=9mmHg for one pig. Since the structures in the five planes enclosed by a dashed line are consistent for all ICP levels and pigs, they have been used for statistical analysis. The reduction in retinal microvascular perfusion with increasing ICP is demonstrated in Figure 5-10b, and changes to the flow in retrobulbar macro-vessels are presented in Figure 5-10c. Clearly, both micro- and macro-vascular flows decrease with increasing ICP. The macro- and microvessels are distinguished based on the number of tracks, vessel width, and velocity magnitude. Similar to the previous discussion, two statistical variables quantify the perfusion: (i) The mean velocity V in the retrobulbar large vessels (blue ROI in Figure 5-10a), and (ii) the retinal microcirculation coefficient, RMC, which is defined as the sum of time-averaged velocity per unit area in all microvessels located within selected regions (yellow ROI in Figure 1a). Hence, the RMC characterizes the density of micro-perfusion, accounting for the number of vessels and velocity in them. Figure 5-10d shows a highly correlated decrease of RMCs averaged over five planes and scaled by the pulse pressure with increasing ICP (r=-0.91, R^2=0.84). The retrobulbar velocity (Figure 5-10e) scaled by PP also generally decreases with increasing ICP, but the data are more scattered, with a 22% lower R^2. Hence, retinal microcirculation can also serve for the noninvasive assessment of ICP, especially for cases where easy acoustic access to the brain is not available, e.g., for adult patients.

5.7. Discussions about the advantages and limitations of the current method

The present findings in the cerebral microcirculation are qualitatively consistent with previous studies reporting a reduction in CBF in patients with hydrocephalus (Leliefeld et al. 2008). This reduction has been attributed to distortion of the periventricular vessels due to ventricular dilation (Bigio and Bruni 1988) and increased flow resistance caused by compression of arterioles and venules (Mori et al. 2002). Previously reported reductions in the number and caliber of capillaries in periventricular and cortical regions during hydrocephalus (Bigio and Bruni 1988;

McAllister and Chovan 1998) also agree with the presently observed decrease in the number of micro-vessels. The trends of decrease in micro-perfusion with increasing ICP vary among brain sections. However, the prediction of the ICP becomes more reliable (higher R^2) when the analysis is based on a broad area in the cortex.

Previous animal studies (Baron 2001) have shown that when the CBF decreases below 20% of the normal level, the neurological damage to the brain becomes irreversible. In the current investigation, for the cases identified as ischemia, the values of $\mathrm{CMC_{cort}}$ are less than 20% of the baseline level. These findings suggest that the significant reduction in $\rho(\mathrm{CMC_{cort}})^2/\mathrm{PP}$ when $\mathrm{ICP/MAP} \geq 0.5$ involves irreversible brain damage. The validity of this postulate needs to be verified by independent cerebral damage assessments. For humans, the reported threshold for irreversible tissue damage is 16-18% of the normal level (Schlaug et al. 1999). The occurrence of ischemia is also accompanied by a significant reduction in the cyclic variations of perfusion during the cardiac cycle. While both PP and MAP for the ischemic and non-ischemic cases are similar when $\mathrm{ICP/MAP} \geq 0.5$, the reduced mean and cyclic variations in flux for ischemic cases suggest that the contraction of the micro-vessels has reached a level that it severely restricts the flow in them. The suppressed micro-perfusion also appears to accelerate the decrease in macro-perfusion. Since the intravascular pressure decreases with increasing branching hierarchy, “remote” vessels 1) are likely to have lower mean flow and flow oscillation magnitudes (Ungersböck et al. 1995; Rashid et al. 2012), and 2) are more likely to be influenced by the external pressure. Accordingly, region 2, which appears to be located “closer” to major arteries, should have higher values of CMC and ΔCMC than regions 1, 3, and 4 at the baseline level, in agreement with the present findings. Moreover, while the observed regional differences in flow pulsatility could be due to the aforementioned reasons, they may be dependent on other factors, including cerebrospinal fluid dynamics and pulsatility, intrinsic regional differences in vascular morphology, compliance and regulation, and/or spatial heterogeneity in brain elasticity.

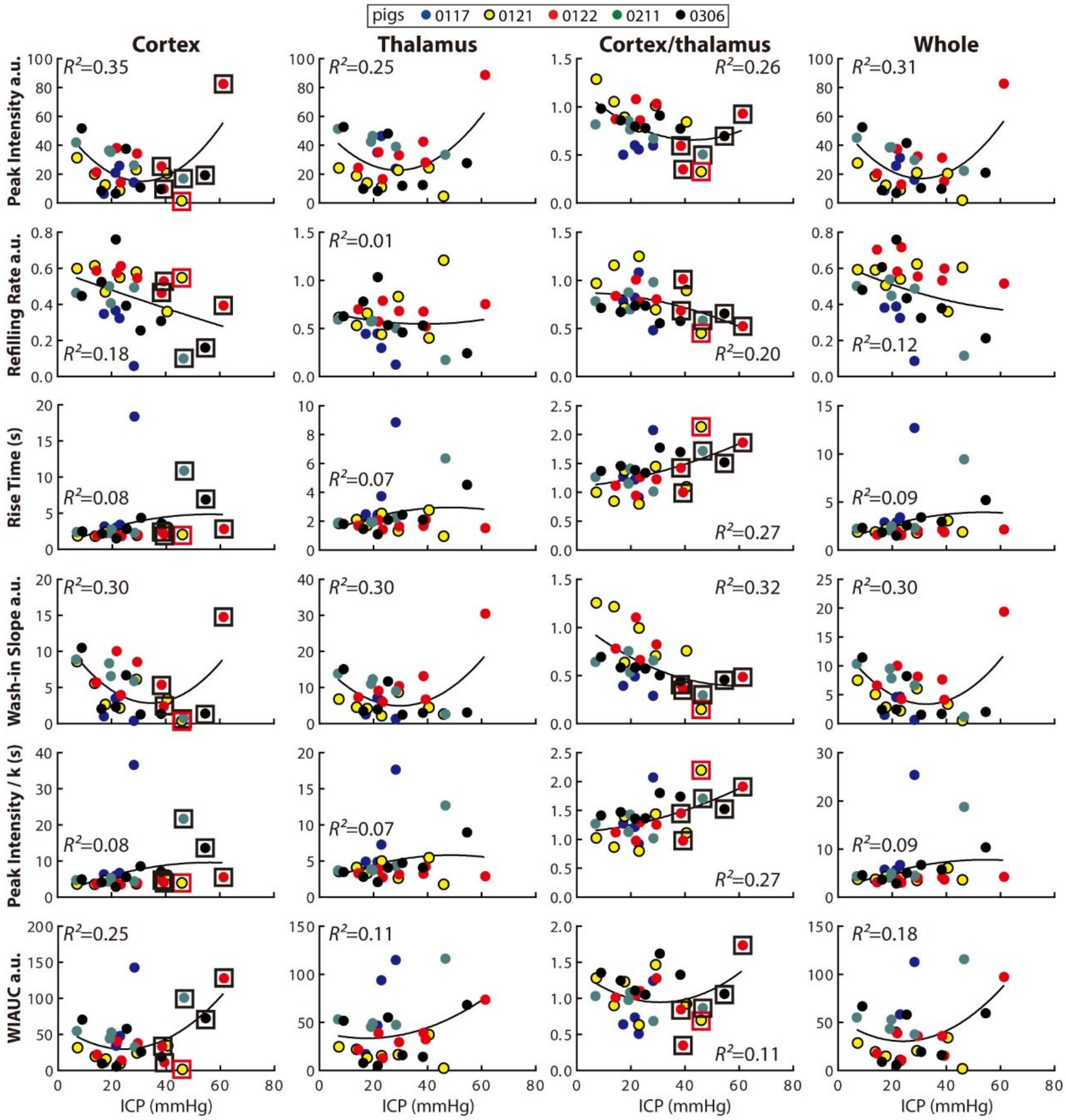

Figure 5-11 The time-intensity curve analysis of disruption & replenishment sequences. Columns (left to right): values of the cortex, thalamus, cortex/thalamus, and the whole coronal plane. Rows (top to bottom): parameters including peak intensity, refilling rate, rise time, average wash-in slope (k), max intensity/k, and area under the curve of the wash-in phase (WIAUC). The ischemia cases are marked by black boxes. The R^2 for each parabolic fit is provided.

Quantifying cerebral and ocular microcirculation appears to provide a feasible method for measuring the ICP and detecting ischemia. Hence, neurosurgical management of neonatal hydrocephalus could be based on the early detection of elevated ICP and a detailed assessment of brain ischemia. The echo-PTV-based approach has several advantages over other methods for characterizing blood circulation. For example, analyses of the time-intensity variations of CEUS images using disruption & replenishment sequences or bolus injection (Greis 2011) could be simpler alternatives for assessing the ICP levels. However, as the quantitative results show (Figure 5-11), all the parameters are scattered without a clear trend with variations in ICP. Moreover, for the ischemia cases, their results are very scattered and are not significantly different from non-ischemic cases in the same ICP range. Hence, these parameters are not suitable for direct quantification of the ICP or for detecting ischemia. As for Doppler, the present data also show that trends of the velocity in the large vessel are less correlated with ICP than the microcirculation statistics. This finding is consistent with that of Hanlo et al. (1995), namely that the Doppler indices measured in the major cerebral arteries are inadequate for monitoring the complex intracranial dynamic responses in patients with raised ICP. Next, MRI and CT have been used extensively for mapping the regional distributions of the CBF, but they cannot resolve the flow in specific blood vessels. The correlations between the MRI-measured CBF and ICP are low with substantial scatter in data (Leliefeld et al. 2008). Furthermore, CEUS imaging can be easily performed at the bedside. Another approach, namely NIRS, is limited to a shallow depth. Hence, it cannot quantify microcirculatory disturbances in the deep cortical matter, which has the most prognostic value in infants with brain injury (Okereafor et al. 2008). In this context, the quantitative perfusion maps extend the potential applications of CEUS imaging well beyond the hydrocephalus population. For example, the risk of elevated ICP with ischemic brain injury is also high in infants with traumatic brain injury, stroke, in-hospital cardiac arrest, and during extracorporeal membrane oxygenation.

The present method has several limitations. First, due to the paucity of published clinical reports and safety data, the application of CEUS to diagnose intracranial pathologies is off-label in the United States (Hwang 2019). For this reason, the present study doesn’t have access to human data. Second, CEUS imaging could be extended to 3D imaging. Third, while the present findings demonstrate the potential role of cerebral and ocular micro-vessels as imaging biomarkers of ICP and brain ischemia, our study is limited to small sample size and an acute hydrocephalus model. The CMC/RMC vs. ICP relationships are likely to be affected by hemodynamics, medications, duration and severity of prior insult, maturation, genetics, metabolomics, and systemic factors. They might also be complicated by the phase of hydrocephalus, i.e., whether it is acute, subacute, chronic, or acute on chronic. For example, previous studies have reported contradictory results about the differences between acute and chronic phases of hydrocephalus. Rashid et al. (2012) report that the mean cerebral capillary diameters of rats are 4.4±0.7, 4.5±0.8, and 4.7±1.0μm for the acute (5-7days), chronic (3-5weeks), and control animals, respectively. The corresponding mean blood flow rates are 0.6±0.6, 0.8±0.7, and 0.8±0.9nL/min, being higher during the chronic phase than that of the acute phase. In contrast, in Higashi et al. (1986), the regional CBFs in the cortex, thalamus, and midbrain show no differences between acute (~1 week) and chronic (4-6 weeks) phases in cat models, but both are lower than the control cases. In order to make our results generalizable to patients with hydrocephalus of various etiologies and disease duration, this study needs to be expanded significantly to investigate how the biomarker accuracy is affected by individual variabilities, accounting for all the aforementioned factors. Moreover, taking advantage of the high spatial resolution features of ULM results, future data analysis could probe into the micro-vascular structures well beyond the flow parameter. For example, one could account for the impact of physiological conditions on several microvascular parameters, such as vessel sizes, branching orders, vessel types, individual microvascular velocities, etc. Accounting for these parameters is likely to improve the robustness of diagnostic potential of CEUS imaging in general, and the assessment of ICP or ischemia in particular.

Chapter 6. Conclusion

This dissertation focuses on the development of echo-PIV and PTV techniques and their applications in cardiovascular and cerebrovascular flows.

The processing of CEUS images consists of image enhancement and bubble motion analysis. In technical development, this dissertation has proposed new methods for the entire pipeline of CEUS image processing. For image enhancements, the primary challenge is to obtain accurate bubble locations from noisy CEUS images. Since the bubble trace is modeled as the convolution between point scatters and spatially varying PSFs, this dissertation has introduced a blind deconvolution method for estimating the PSF and bubble locations simultaneously. Subsequently, we have introduced a U-net, a superresolution network (SupBD-net), and a self-supervised learning method (SelfBD-net) to perform an end-to-end task for locating the bubble centers directly from the raw CEUS images and to improve the processing speed as well as the subpixel localization accuracy. The bubble localization performances of these methods are evaluated based on realistic synthetic CEUS images. The result shows that, for all methods, the bubble center location error increases with increasing PSF size, increasing noise, and increasing bubble density. The SupBD-net and SelfBD-net have outperformed the blind deconvolution in terms of localization accuracy, where the bubble center location error for SupBD-net is less than one-third of that of the blind deconvolution. Moreover, the SupBD-net and SelfBD-net can distinguish closely located microbubbles that are separated by 60% of the local PSF size, while the blind deconvolution can only distinguish bubbles that are separated by 108% of the local PSF size.

The bubble motion analysis consists of two parts, namely, the multi-parameter optimized echo-PIV procedure and echo-PTV. The procedures for echo-PIV mainly follow the previous work of Sampath et al. (2018). As for bubble tracking, the primary challenge is to determine the correct bubble tracks out of low temporal resolution datasets where the bubbles are densely distributed and moving in various velocities. Hence, this dissertation has proposed a multi-hypothesis, global-optimized, Kalman-filter-based echo-PTV strategy. The validity of bubble tracking is verified by the pulse-wave doppler measurements in real CEUS images, showing good agreement in the measured velocity. Combining the improved bubble localization by SupBD-net and optimized tracking, the current methods could distinguish microvessels that are 40μm apart in actual CEUS images, which is 3 times higher spatial resolution than that of blind deconvolution.

Based on the improved image processing procedures, this dissertation performs echo-PIV for the quantitative characterization of the effect of ECMO flow rate on the native cardiac output in the aortic root of a pig model with severe myocardial injury. The ECMO flow rate affects the direction and location of secondary vorticial flow structures generated during diastole, as well as the velocity, acceleration, and duration of the cardiac outflux during systole. Two flow rate regimes are identified: For $Q_E \geq 3.0$L/min, the maximum velocity, phase of peak deceleration, duration with open valve, MAP, and VTI increase with decreasing flow rate, peaking at $Q_E=3.0$L/min, suggestive of sufficient ECMO support. Conversely, for $Q_E \leq 2.5$L/min, as the ECMO flow rate is reduced, the peak velocity, MAP, and VTI decrease, while the phase of peak deceleration and duration with open valve plateau during systole. The deceleration during the transition to diastole is much milder in this range. For the specific physiological condition of the current animal, the optimal ECMO flow rate is 3.0L/min. Beyond the specific details, the current study suggests that combining the aortic flow structure and associated parameters with conventional hemodynamic measurements provides a more comprehensive knowledge of the pressure-volume loading state during ECMO. This kind of information might improve the clinical management of patients undergoing VA-ECMO.

In the second application, detailed maps of the cerebral and ocular microcirculation, obtained by tracking microbubbles in CEUS images of hydrocephalic pediatric porcine models, are used for quantifying the impact of elevated ICP on cerebral and ocular perfusion. The results show that the CMCs in the cortex and thalamus, the velocity in the cerebral macro-vessel, the retinal microcirculation, and the retrobulbar major vascular flow decrease with increasing ICP. Functional relationships are obtained when the analysis incorporates hemodynamic effects. A decaying quadratic function (r=-0.85, R^2=0.72) describes the relationship between increasing ICP and $\mathrm{CMC_{cort}/PP}$. Alternatively, $\mathrm{PP\text{-}(0.17CMC_{cort}\text{-}0.29)MAP}$ shows a highly correlated (r=0.92, R^2=0.84) linear increase with ICP. Moreover, a highly correlated relationship between the RMC/PP and ICP is also discovered for retinal blood flow. In contrast, results based on macrovascular perfusion are more scattered and less correlated. Hence, quantitative evaluation of the cortical and retinal microcirculation could be developed into a plausible method for noninvasive bedside assessment of ICP. Furthermore, when $\mathrm{ICP/MAP} \geq 0.5$, several ischemia cases are identified by a lactate-to-pyruvate ratio exceeding 30. These cases involve significant reductions in the nondimensionalized cortical microcirculation ($\rho\mathrm{CMC_{cort}^2/PP}$) that deviate from the rest of the data. These findings suggest that measurements of cortical micro-perfusion could potentially be used for the detection of cerebral ischemia.

In general, the development and implementation of echo-PIV and PTV techniques for analyzing microbubbles in CEUS images to quantify cardiovascular and cerebrovascular flows have significant potential for improving diagnostic and treatment outcomes in various medical fields. With ongoing advancements in image processing and machine learning algorithms, these techniques may become more efficient and widely applicable, providing a non-invasive and accurate method for assessing blood flow and detecting abnormalities in patients. Further research and clinical trials will be essential to fully realize the potential of this technology in diagnosis and treatment outcomes in cardiology, neurology, and critical care medicine.

Bibliography

Abe H, Caracciolo G, Kheradvar A, et al (2013) Contrast echocardiography for assessing left ventricular vortex strength in heart failure: a prospective cohort study. Eur Hear Journal–Cardiovascular Imaging 14:1049–1060

Ackermann D, Schmitz G (2016a) Detection and Tracking of Multiple Microbubbles in Ultrasound B-Mode Images. IEEE Trans Ultrason Ferroelectr Freq Control 63:72–82. https://doi.org/10.1109/TUFFC.2015.2500266

Ackermann D, Schmitz G (2016b) Detection and Tracking of Multiple Microbubbles in Ultrasound B-Mode Images. IEEE Trans Ultrason Ferroelectr Freq Control 63:72–82. https://doi.org/10.1109/TUFFC.2015.2500266

Adams-Chapman I, Hansen NI, Stoll BJ, Higgins R (2008) Neurodevelopmental outcome of extremely low birth weight infants with posthemorrhagic hydrocephalus requiring shunt insertion. Pediatrics 121:e1167–e1177

Adrian L, Adrian RJ, Westerweel J (2011) Particle image velocimetry. Cambridge University Press

Agati L, Cimino S, Tonti G, et al (2014) Quantitative analysis of intraventricular blood flow dynamics by echocardiographic particle image velocimetry in patients with acute myocardial infarction at different stages of left ventricular dysfunction. Eur Hear Journal–Cardiovascular Imaging 15:1203–1212

Assmann A, Benim AC, Gül F, et al (2012) Pulsatile extracorporeal circulation during on-pump cardiac surgery enhances aortic wall shear stress. J Biomech 45:156–163

Bai C, Liu C, Yu X, et al (2019) Imaging enhancement of light-sheet fluorescence microscopy via deep learning. IEEE Photonics Technol Lett 31:1803–1806

Baron J-CC (2001) Perfusion thresholds in human cerebral ischemia: Historical perspective and therapeutic implications. Cerebrovasc Dis 11:2–8. https://doi.org/10.1159/000049119

Becker JA, Short BL, Martin GR (1998) Cardiovascular complications adversely affect survival during extracorporeal membrane oxygenation. Crit Care Med 26:1582–1586

Bigio MR Del, Bruni JE (1988) Changes in periventricular vasculature of rabbit brain following induction of hydrocephalus and after shunting. J Neurosurg 69:115–120

Blackman SS (2004) Multiple hypothesis tracking for multiple target tracking. IEEE Aerosp Electron Syst Mag 19:5–18

Bragin DE, Bush RC, Müller WS, Nemoto EM (2011) High intracranial pressure effects on cerebral cortical microvascular flow in rats. J Neurotrauma 28:775–785

Burkhoff D, Sayer G, Doshi D, Uriel N (2015) Hemodynamics of mechanical circulatory support. J Am Coll Cardiol 66:2663–2674

Caner H, Atasever A, Kilinc K, et al (1993) Lipid peroxide level increase in experimental hydrocephalus. Acta Neurochir (Wien) 121:68–71

Christensen-Jeffries K, Browning RJ, Tang M-X, et al (2014) In vivo acoustic super-resolution and super-resolved velocity mapping using microbubbles. IEEE Trans Med Imaging 34:433–440

Chung M, Shiloh AL, Carlese A (2014) Monitoring of the adult patient on venoarterial extracorporeal membrane oxygenation. Sci World J 2014:. https://doi.org/10.1155/2014/393258

Couture O, Hingot V, Heiles B, et al (2018) Ultrasound localization microscopy and super-resolution: A state of the art. IEEE Trans Ultrason Ferroelectr Freq Control 65:1304–1320

Crapper M, Bruce T, Gouble C (2000) Flow field visualization of sediment-laden flow using ultrasonic imaging. Dyn Atmos Ocean 31:233–245

Cristianini N, Shawe-Taylor J (2000) An introduction to support vector machines and other kernel-based learning methods. Cambridge university press

Dai X, Bragina O, Zhang T, et al (2016) High intracranial pressure induced injury in the healthy rat brain. Crit Care Med 44:e633

Demené C, Deffieux T, Pernot M, et al (2015) Spatiotemporal clutter filtering of ultrafast ultrasound data highly increases Doppler and fUltrasound sensitivity. IEEE Trans Med Imaging 34:2271–2285

Demené C, Robin J, Dizeux A, et al (2021) Transcranial ultrafast ultrasound localization microscopy of brain vasculature in patients. Nat Biomed Eng 5:219–228. https://doi.org/10.1038/s41551-021-00697-x

Desailly Y, Couture O, Fink M, Tanter M (2013) Sono-activated ultrasound localization microscopy. Appl Phys Lett 103:174107. https://doi.org/10.1063/1.4826597

Donker DW, Brodie D, Henriques JPS, Broomé M (2019) Left Ventricular Unloading During Veno-Arterial ECMO: A Simulation Study. ASAIO J 65:11–20. https://doi.org/10.1097/MAT.0000000000000755

Duhaime A-C, Margulies SS, Durham SR, et al (2000) Maturation-dependent response of the piglet brain to scaled cortical impact. J Neurosurg 93:455–462

Eriksen VR, Abdolalizadeh B, Trautner S, et al (2016) Mechanical and vasomotor properties of piglet isolated middle cerebral artery. Pharmacol Res Perspect 5:e00279–e00279. https://doi.org/10.1002/prp2.279

Errico C, Pierre J, Pezet S, et al (2015) Ultrafast ultrasound localization microscopy for deep super-resolution vascular imaging. Nature 527:499–502

Falk T, Mai D, Bensch R, et al (2019) U-Net: deep learning for cell counting, detection, and morphometry. Nat Methods 16:67–70

Fernell E, Hagberg G, Hagberg B (1993) Infantile hydrocephalus in preterm, low-birth-weight infants—a nationwide Swedish cohort study 1979–1988. Acta Pædiatrica 82:45–48

Firsching R, Müller C, Pauli S-U, et al (2011) Noninvasive assessment of intracranial pressure with venous ophthalmodynamometry. J Neurosurg 115:371–374

Foiret J, Zhang H, Ilovitsh T, et al (2017) Ultrasound localization microscopy to image and assess microvasculature in a rat kidney. Sci Rep 7:1–12

Foroozan F, O'Reilly MA, Hynynen K (2018) Microbubble localization for three-dimensional superresolution ultrasound imaging using curve fitting and deconvolution methods. IEEE Trans Biomed Eng 65:2692–2703

Glorot X, Bengio Y (2010) Understanding the difficulty of training deep feedforward neural networks. In: Proceedings of the thirteenth international conference on artificial intelligence and statistics. JMLR Workshop and Conference Proceedings, pp 249–256

Greis C (2011) Quantitative evaluation of microvascular blood flow by contrast-enhanced ultrasound (CEUS). Clin Hemorheol Microcirc 49:137–149

Gu K, Guan Z, Lin X, et al (2019) Numerical analysis of aortic hemodynamics under the support of venoarterial extracorporeal membrane oxygenation and intra-aortic balloon pump. Comput Methods Programs Biomed 182:105041

Gu K, Zhang Z, Gao B, et al (2018) Hemodynamic effects of perfusion level of peripheral ECMO on cardiovascular system. Biomed Eng Online 17:1–14

Guerra Paradas E (2017) Monocular SLAM: data association and sensing through a human-assisted uncalibrated visual system. Universitat Politècnica de Catalunya

Hanlo PW, Gooskens R, Nijhuis IJM, et al (1995) Value of transcranial Doppler indices in predicting raised ICP in infantile hydrocephalus. Child's Nerv Syst 11:595–603

Hansen KL, Møller-Sørensen H, Kjaergaard J, et al (2016) Intra-operative vector flow imaging using ultrasound of the ascending aorta among 40 patients with normal, stenotic and replaced aortic valves. Ultrasound Med Biol 42:2414–2422

Hansen KL, Møller-Sørensen H, Kjaergaard J, et al (2017) Vector flow imaging compared with conventional Doppler ultrasound and thermodilution for estimation of blood flow in the ascending aorta. Ultrason Imaging 39:3–18

Hansen KL, Møller-Sørensen H, Pedersen MM, et al (2015) First report on intraoperative vector flow imaging of the heart among patients with healthy and diseased aortic valves. Ultrasonics 56:243–250

He K, Sun J (2015) Convolutional neural networks at constrained time cost. In: Proceedings of the IEEE conference on computer vision and pattern recognition. pp 5353–5360

He K, Zhang X, Ren S, Sun J (2016) Deep Residual Learning for Image Recognition. In: 2016 IEEE Conference on Computer Vision and Pattern Recognition (CVPR). pp 770–778

Heiles B, Correia M, Hingot V, et al (2019) Ultrafast 3D Ultrasound Localization Microscopy Using a 32$\times $32 Matrix Array. IEEE Trans Med Imaging 38:2005–2015

Higashi K, Asahisa H, Ueda N, et al (1986) Cerebral blood flow and metabolism in experimental hydrocephalus. Neurol Res 8:169–176. https://doi.org/10.1080/01616412.1986.11739750

Hope MD, Hope TA, Meadows AK, et al (2010) Bicuspid aortic valve: four-dimensional MR evaluation of ascending aortic systolic flow patterns. Radiology 255:53–61

Hope TA, Markl M, Wigström L, et al (2007) Comparison of flow patterns in ascending aortic aneurysms and volunteers using four-dimensional magnetic resonance velocity mapping. J Magn Reson Imaging An Off J Int Soc Magn Reson Med 26:1471–1479

Hwang M (2019) Introduction to contrast-enhanced ultrasound of the brain in neonates and infants: current understanding and future potential. Pediatr Radiol 49:254–262

Iskandar BJ, McLaughlin C, Mapstone TB, et al (1998) Pitfalls in the diagnosis of ventricular shunt dysfunction: radiology reports and ventricular size. Pediatrics 101:1031–1036

Isola P, Zhu J-Y, Zhou T, Efros AA (2017) Image-to-image translation with conditional adversarial networks. In: Proceedings of the IEEE conference on computer vision and pattern recognition. pp 1125–1134

Jerman T, Pernuš F, Likar B, Špiclin Ž (2016) Enhancement of vascular structures in 3D and 2D angiographic images. IEEE Trans Med Imaging 35:2107–2118

Jeronimo MD, Najjari MR, Rival DE (2020) Echo-Lagrangian particle tracking: an ultrasound-based method for extracting path-dependent flow quantities. Meas Sci Technol 31:54008

Kahle KT, Kulkarni A V, Limbrick Jr DD, Warf BC (2016) Hydrocephalus in children. Lancet 387:788–799

Keane RD, Adrian Rj, Zhang Y (1995) Super-resolution particle imaging velocimetry. Meas Sci Technol 6:754

Khan MN, Shallwani H, Khan MU, Shamim MS (2017) Noninvasive monitoring intracranial pressure–a review of available modalities. Surg Neurol Int 8:

Kilner PJ, Yang GZ, Mohiaddin RH, et al (1993) Helical and retrograde secondary flow patterns in the aortic arch studied by three-directional magnetic resonance velocity mapping. Circulation 88:2235–2247

Kim C, Li F, Ciptadi A, Rehg JM (2015) Multiple hypothesis tracking revisited. In: Proceedings of the IEEE international conference on computer vision. pp 4696–4704

Kim H-B, Hertzberg JR, Shandas R (2004) Development and validation of echo PIV. Exp Fluids 36:455–462

Kingma DP, Ba J (2014) Adam: A method for stochastic optimization. arXiv Prepr arXiv14126980

Kirkpatrick PJ, Smielewski P, Czosnyka M, et al (1995) Near-infrared spectroscopy use in patients with head injury. J Neurosurg 83:963–970

Kochan M, McPadden J, Bass WT, et al (2017) Changes in cerebral oxygenation in preterm infants with progressive posthemorrhagic ventricular dilatation. Pediatr Neurol 73:57–63

Kolarovszki B, Zubor P, Kolarovszka H, et al (2013) The assessment of intracranial dynamics by transcranial Doppler sonography in perioperative period in paediatric hydrocephalus. Arch Gynecol Obstet 287:229–238

Kvitting J-PE, Ebbers T, Wigström L, et al (2004) Flow patterns in the aortic root and the aorta studied with time-resolved, 3-dimensional, phase-contrast magnetic resonance imaging: implications for aortic valve–sparing surgery. J Thorac Cardiovasc Surg 127:1602–1607

Ledig C, Theis L, Huszár F, et al (2017) Photo-realistic single image super-resolution using a generative adversarial network. In: Proceedings of the IEEE conference on computer vision and pattern recognition. pp 4681–4690

Leliefeld PH, Gooskens RHJMJM, Vincken KL, et al (2008) Magnetic resonance imaging for quantitative flow measurement in infants with hydrocephalus: a prospective study. J Neurosurg Pediatr 2:163–170. https://doi.org/10.3171/PED/2008/2/9/163

Lim B, Son S, Kim H, et al (2017a) Enhanced Deep Residual Networks for Single Image Super-Resolution. In: 2017 IEEE Conference on Computer Vision and Pattern Recognition Workshops (CVPRW). pp 1132–1140

Lim HS, Howell N, Ranasinghe A (2017b) Extracorporeal life support: physiological concepts and clinical outcomes. J Card Fail 23:181–196

Lin F, Shelton SE, Espíndola D, et al (2017) 3-D ultrasound localization microscopy for identifying microvascular morphology features of tumor angiogenesis at a resolution beyond the diffraction limit of conventional ultrasound. Theranostics 7:196

Liu X, Zhou T, Lu M, et al (2020) Deep learning for ultrasound localization microscopy. IEEE Trans Med Imaging 39:3064–3078

Mahalanobis PC (1936) On the generalized distance in statistics. Proc Natl Inst Sci India 2:49–55

Makdisi G, Wang I (2015) Extra Corporeal Membrane Oxygenation (ECMO) review of a lifesaving technology. J Thorac Dis 7:E166

Mangual JO, Kraigher-Krainer E, De Luca A, et al (2013) Comparative numerical study on left ventricular fluid dynamics after dilated cardiomyopathy. J Biomech 46:1611–1617. https://doi.org/https://doi.org/10.1016/j.jbiomech.2013.04.012

Manly BFJ, Alberto JAN (2016) Multivariate statistical methods: a primer. CRC press

Markl M, Draney MT, Hope MD, et al (2004) Time-resolved 3-dimensional velocity mapping in the thoracic aorta: visualization of 3-directional blood flow patterns in healthy volunteers and patients. J Comput Assist Tomogr 28:459–468

Martin GR, Short BL, Abbott C, O'brien AM (1991) Cardiac stun in infants undergoing extracorporeal membrane oxygenation. J Thorac Cardiovasc Surg 101:607–611

Martínez-Legazpi P, Bermejo J, Benito Y, et al (2014) Contribution of the Diastolic Vortex Ring to Left Ventricular Filling. J Am Coll Cardiol 64:1711 LP – 1721.

https://doi.org/10.1016/j.jacc.2014.06.1205

McAllister JP, Chovan P (1998) Neonatal hydrocephalus. Mechanisms and consequences. Neurosurg Clin N Am 9:73–93

Morbiducci U, Ponzini R, Rizzo G, et al (2011) Mechanistic insight into the physiological relevance of helical blood flow in the human aorta: an in vivo study. Biomech Model Mechanobiol 10:339–355

Mori K, Maeda M, Asegawa S, Iwata J (2002) Quantitative local cerebral blood flow change after cerebrospinal fluid removal in patients with normal pressure hydrocephalus measured by a double injection method with N-isopropyl-p-[123] iodoamphetamine. Acta Neurochir (Wien) 144:255–263. https://doi.org/10.1007/s007010200033

Munch TN, Rostgaard K, Rasmussen M-LH, et al (2012) Familial aggregation of congenital hydrocephalus in a nationwide cohort. Brain 135:2409–2415. https://doi.org/10.1093/brain/aws158

Nakada J, Oka N, Nagahori T, et al (1992) Changes in the cerebral vascular bed in experimental hydrocephalus: an angio-architectural and histological study. Acta Neurochir (Wien) 114:43

Natarajan BK (1995) Sparse approximate solutions to linear systems. SIAM J Comput 24:227–234

Nehme E, Weiss LE, Michaeli T, Shechtman Y (2018) Deep-STORM: super-resolution single-molecule microscopy by deep learning. Optica 5:458–464

Oka N, Nakada J, Endo S, et al (1985) Angioarchitecture in experimental hydrocephalus. Neurol Med Chir (Tokyo) 25:701–706

Okereafor A, Allsop J, Counsell SJ, et al (2008) Patterns of brain injury in neonates exposed to perinatal sentinel events. Pediatrics 121:906–914

Opacic T, Dencks S, Theek B, et al (2018) Motion model ultrasound localization microscopy for preclinical and clinical multiparametric tumor characterization. Nat Commun 9:1527. https://doi.org/10.1038/s41467-018-03973-8

Ostadal P, Mlcek M, Kruger A, et al (2015) Increasing venoarterial extracorporeal membrane oxygenation flow negatively affects left ventricular performance in a porcine model of cardiogenic shock. J Transl Med 13:266

Östergård PRJ (2001) A new algorithm for the maximum-weight clique problem. Nord J Comput 8:424–436

Pan J, Hu Z, Su Z, Yang M (2017) L_0 -Regularized Intensity and Gradient Prior for Deblurring Text Images and Beyond. IEEE Trans Pattern Anal Mach Intell 39:342–355. https://doi.org/10.1109/TPAMI.2016.2551244

Pavlushkov E, Berman M, Valchanov K (2017) Cannulation techniques for extracorporeal life support. Ann Transl Med 5:70. https://doi.org/10.21037/atm.2016.11.47

Piechnik SK, Chiarelli PA, Jezzard P (2008) Modelling vascular reactivity to investigate the basis of the relationship between cerebral blood volume and flow under CO2 manipulation. Neuroimage 39:107–118. https://doi.org/https://doi.org/10.1016/j.neuroimage.2007.08.022

Poelma C (2017) Ultrasound imaging velocimetry: a review. Exp Fluids 58:1–28

Purins K, Enblad P, Wiklund L, et al (2012) Brain tissue oxygenation and cerebral perfusion pressure thresholds of ischemia in a standardized pig brain death model. Neurocrit Care 16:462–469. https://doi.org/10.1007/s12028-012-9675-3

Radford A, Metz L, Chintala S (2015) Unsupervised representation learning with deep convolutional generative adversarial networks. arXiv Prepr arXiv151106434

Rao P, Khalpey Z, Smith R, et al (2018) Venoarterial Extracorporeal Membrane Oxygenation for Cardiogenic Shock and Cardiac Arrest: Cardinal Considerations for Initiation and Management. Circ Hear Fail 11:e004905

Rashid S, McAllister JP, Yu Y, Wagshul ME (2012) Neocortical capillary flow pulsatility is not elevated in experimental communicating hydrocephalus. J Cereb Blood Flow Metab 32:318–329

Reed Murtagh F, Quencer RM, Poole CA (1979) Cerebrospinal fluid shunt function and hydrocephalus in the pediatric age group: a radiographic/clinical correlation. Radiology

132:385–388

Ronneberger O, Fischer P, Brox T (2015) U-Net: Convolutional Networks for Biomedical Image Segmentation BT - Medical Image Computing and Computer-Assisted Intervention – MICCAI 2015. In: Navab N, Hornegger J, Wells WM, Frangi AF (eds). Springer International Publishing, Cham, pp 234–241

Ruesch A, Yang J, Schmitt S, et al (2020) Estimating intracranial pressure using pulsatile cerebral blood flow measured with diffuse correlation spectroscopy. Biomed Opt Express 11:1462–1476. https://doi.org/10.1364/BOE.386612

Sampath K, Harfi TT, George RT, Katz J (2018) Optimized time-resolved echo particle image velocimetry–particle tracking velocimetry measurements elucidate blood flow in patients with left ventricular thrombus. J Biomech Eng 140:41010

Schinkel AFL, Kaspar M, Staub D (2016) Contrast-enhanced ultrasound: clinical applications in patients with atherosclerosis. Int J Cardiovasc Imaging 32:35–48

Schlaug G, Benfield A, Baird AE, et al (1999) The ischemic penumbra: operationally defined by diffusion and perfusion MRI. Neurology 53:1528

Schmidt M, Burrell A, Roberts L, et al (2015) Predicting survival after ECMO for refractory cardiogenic shock: the survival after veno-arterial-ECMO (SAVE)-score. Eur Heart J 36:2246–2256

Shakeri M, Vahedi P, Lotfinia I (2008) A review of hydrocephalus: history, etiologies, diagnosis, and treatment. Neurosurg Q 18:216–220

Sheng J, Malkiel E, Katz J (2008) Using digital holographic microscopy for simultaneous measurements of 3D near wall velocity and wall shear stress in a turbulent boundary layer. Exp Fluids 45:1023–1035

Shin H-C, Roth HR, Gao M, et al (2016) Deep convolutional neural networks for computer-aided detection: CNN architectures, dataset characteristics and transfer learning. IEEE Trans Med Imaging 35:1285–1298

Siepmann M, Schmitz G, Bzyl J, et al (2011) Imaging tumor vascularity by tracing single microbubbles. In: 2011 IEEE International Ultrasonics Symposium. IEEE, pp 1906–1909

Solomon O, van Sloun RJG, Wijkstra H, et al (2019) Exploiting flow dynamics for superresolution in contrast-enhanced ultrasound. IEEE Trans Ultrason Ferroelectr Freq Control 66:1573–1586

Stevens MC, Callaghan FM, Forrest P, et al (2017) Flow mixing during peripheral veno-arterial extra corporeal membrane oxygenation–A simulation study. J Biomech 55:64–70

Stevens MC, Callaghan FM, Forrest P, et al (2018) A computational framework for adjusting flow during peripheral extracorporeal membrane oxygenation to reduce differential hypoxia. J Biomech 79:39–44

Szabo TL (2004) Diagnostic ultrasound imaging: inside out. Academic press

Tang S, Song P, Trzasko JD, et al (2020) Kalman Filter-Based Microbubble Tracking for Robust Super-Resolution Ultrasound Microvessel Imaging. IEEE Trans Ultrason Ferroelectr Freq Control 67:1738–1751. https://doi.org/10.1109/TUFFC.2020.2984384

Tully HM, Dobyns WB (2014) Infantile hydrocephalus: a review of epidemiology, classification and causes. Eur J Med Genet 57:359–368

Ulyanov D, Vedaldi A, Lempitsky V (2016) Instance normalization: The missing ingredient for fast stylization. arXiv Prepr arXiv160708022

Ungersböck K, Tenckhoff D, Heimann A, et al (1995) Transcranial Doppler and cortical microcirculation at increased intracranial pressure and during the Cushing response: an experimental study on rabbits. Neurosurgery 36:147–157

van Sloun RJG, Solomon O, Bruce M, et al (2020) Super-resolution ultrasound localization microscopy through deep learning. IEEE Trans Med Imaging 40:829–839

Viessmann OM, Eckersley RJ, Christensen-Jeffries K, et al (2013) Acoustic super-resolution with ultrasound and microbubbles. Phys Med Biol 58:6447–6458. https://doi.org/10.1088/0031-9155/58/18/6447

Vincent J-L, Rhodes A, Perel A, et al (2011) Clinical review: Update on hemodynamic monitoring-a consensus of 16. Crit care 15:1–8

Vu T, Van Nguyen C, Pham TX, et al (2018) Fast and efficient image quality enhancement via desubpixel convolutional neural networks. In: Proceedings of the European Conference on Computer Vision (ECCV) Workshops. p 0

Walker A (2009) Testing of Doppler Ultrasound Systems. Linköping University Electronic

Wang T-C, Liu M-Y, Zhu J-Y, et al (2018) High-resolution image synthesis and semantic manipulation with conditional gans. In: Proceedings of the IEEE conference on computer vision and pattern recognition. pp 8798–8807

Wang Z, Ling Q, Huang T (2016) Learning deep ℓ 0 encoders. In: Proceedings of the AAAI Conference on Artificial Intelligence

Whyte O, Sivic J, Zisserman A (2014) Deblurring shaken and partially saturated images. Int J Comput Vis 110:185–201

Wozniak M, McLone DG, Raimondi AJ (1975) Micro-and macrovascular changes as the direct cause of parenchymal destruction in congenital murine hydrocephalus. J Neurosurg 43:535–545

Xu L, Lu C, Xu Y, Jia J (2011) Image smoothing via L 0 gradient minimization. In: Proceedings of the 2011 SIGGRAPH Asia conference. pp 1–12

Yeom KW, Lober RM, Alexander A, et al (2014) Hydrocephalus decreases arterial spin-labeled cerebral perfusion. Am J Neuroradiol 35:1433–1439

Zaharchuk G, Mandeville JB, Bogdanov AA, et al (1999) Cerebrovascular dynamics of autoregulation and hypoperfusion. An MRI study of CBF and changes in total and microvascular cerebral blood volume during hemorrhagic hypotension. Stroke 30:2195–2197. https://doi.org/10.1161/01.str.30.10.2197

Zhang Q, Gao B, Chang Y (2018) The numerical study on the effects of cardiac function on the aortic oxygen distribution. Med Biol Eng Comput 56:1305–1313

Zhang X, Medow JE, Iskandar BJ, et al (2017) Invasive and noninvasive means of measuring intracranial pressure: a review. Physiol Meas 38:R143

Zhang Z, Hwang M, Kilbaugh TJ, et al (2022) Cerebral microcirculation mapped by echo particle tracking velocimetry quantifies the intracranial pressure and detects ischemia. Nat Commun 13:666. https://doi.org/10.1038/s41467-022-28298-5

Zhang Z, Zhou X, Suarez-Pierre A, et al (2020) Time-Resolved Echo-Particle Image/Tracking Velocimetry Measurement of Interactions Between Native Cardiac Output and Veno-Arterial ECMO Flows. J Biomech Eng 143:

Zorc JJ, Krugman SD, Ogborn J, Benson J (2002) Radiographic evaluation for suspected cerebrospinal fluid shunt obstruction. Pediatr Emerg Care 18:337–340

Zoremba N, Schnoor J, Berens M, et al (2007) Brain metabolism during a decrease in cerebral perfusion pressure caused by an elevated intracranial pressure in the porcine neocortex. Anesth Analg 105:744–750. https://doi.org/10.1213/01.ane.0000278160.66389.1c

Curriculum Vitae

Zeng Zhang

Address: 960 Southerly Road, J469, Towson, MD 21204;

E-mail: zeng@jhu.edu;

Phone: (001) 4103696390

Education

Ph.D. in Fluids Dynamics, The Johns Hopkins University, Baltimore, MD **March 2023**

Thesis title: *Echo particle image/tracking velocimetry: technical development and in vivo applications in cardiovascular and cerebrovascular flows*

Thesis advisor: Professor Joseph Katz

B.Eng. in Engineering Mechanics, Beihang University, Beijing, China **June 2016**

Thesis title: *Reduction of Gurney Flap Drag Penalty using DBD Plasma Actuator* (Excellent Thesis Award)

Thesis advisor: Professor Jinjun Wang GPA**:** 3.92/4.0

Research Experience

Research Assistant at The Johns Hopkins University 09/2017-present

Advisor: Prof. Joseph Katz & Dr. Misun Hwang (From Children's Hospital of Philadelphia)

General topic: Ultrasound Localization Microscopy (ULM) is a technique for obtaining super-resolved microvasculature in various organs at a micrometer spatial resolution by localizing and tracking intravascular echogenic microbubbles. This batch of research activities involves: **1) developing the entire ULM method/algorithm pipeline for both commercial and ultrafast ultrasound scanners; 2) applications of ULM for the noninvasive assessment of intracranial pressure (ICP).**

a) Noninvasive assessment of ICP via ocular hemodynamics measured by ULM 02/2022-present

1. ULM code and algorithm development for **ultrafast ultrasound scanners** (>400 frames/s), including SVD filtering for extracting bubble signals; spatio-temporal filtering for separating bubbles moving at different speeds; self-supervised deep learning for precise subpixel localization of bubbles; multi-hypothesis and globally optimized Kalman tracker for bubble tracking.

2. Built a motorized six-degree-of-freedom robotic arm for precisely controlling ultrasound transducers during transocular imaging.

3. Discovered that at constant intraocular pressure, the retinal microvessel blood flows were highly correlated with ICP (>0.9) when the effect of pulse pressure was accounted for. Hence, retinal microcirculation can be used for the noninvasive assessment of ICP.

b) Improving sub-pixel accuracy for ULM using supervised and self-supervised deep learning

06/2021-02/2022

1. Developed a supervised superresolution network for localizing microbubbles. The resulting error in bubble centers was one-third that of conventional methods, resulting in a 2~3-fold increase in spatial resolution for the microvessels.

2. Developed a self-supervised network for precisely localizing microbubbles in any ultrasound systems, particularly those unknown to the superresolution network's training set. The resulting resolution and accuracy were comparable to the supervised methods.

c) Noninvasive assessment of ICP via cerebral hemodynamics measured by ULM 09/2019-06/2021

1. ULM code and algorithm development for **clinically available ultrasound scanners**, including an image stabilization procedure based on affine transformation and non-rigid demon algorithm; piecewise blind deconvolution for precisely localizing bubbles; multi-hypothesis and globally optimized Kalman tracker for bubble tracking.

2. Discovered that the cortical microvessel blood flows were highly correlated with ICP (>0.9) when the effect of pulse pressure was accounted for. Hence, cortical microcirculation can be used for the noninvasive assessment of ICP.

3. Discovered that nondimensionalized cortical blood flow was one order of magnitude lower in brain ischemia cases than in non-ischemia cases. Hence, cortical microcirculation can be used for detecting brain ischemia.

d) Time-resolved echo-particle image/tracking velocimetry measurement of interactions between native cardiac output and veno-arterial ECMO Flows 01/2018-09/2019

1. Echo-particle image/tracking velocimetry code and algorithm development for **clinically available ultrasound scanners**, enabling the real-time monitoring of the flow structures in the aortic root of the patients undergoing veno-arterial ECMO treatment.
2. The results demonstrated the ability of echo-particle image/tracking velocimetry techniques to noninvasively monitor the patient's cardiac outputs during veno-arterial ECMO treatment. The ECMO flow rate can be adjusted to maintain an optimal cardiac output, increasing the rate of successful care for ECMO patients.

Teaching Experience

Teaching assistant for "*Thermodynamics*", The Johns Hopkins University Fall 2018

Teaching assistant for "*Jet and Rocket Propulsion*", The Johns Hopkins University Spring 2020

Teaching assistant for "*Thermodynamics*", The Johns Hopkins University Fall 2020

Publication & Patent

Publication

Journals

- **Zeng Zhang**, Misun Hwang, Todd J. Kilbaugh, and Joseph Katz. "Improving Sub-pixel Accuracy in Ultrasound Localization Microscopy Using Supervised and Self-supervised Deep Learning." (2023, in preparation)
- Misun Hwang, **Zeng Zhang (co-first)**, Todd J. Kilbaugh, and Joseph Katz. " Ocular Microvascular Indices of Intracranial Pressure in Hydrocephalus." (2023, in preparation)
- **Zeng Zhang**, Misun Hwang, Todd J. Kilbaugh, Anush Sridharan, and Joseph Katz. "Cerebral Microcirculation Mapped by Echo Particle Tracking Velocimetry Quantifies the Intracranial Pressure and

Detects Ischemia." ***Nature communications*** 13, no. 1 (2022): 1-15.

● Misun Hwang, **Zeng Zhang**, Joseph Katz, Colbey Freeman, and Todd Kilbaugh. "Brain Contrast-Enhanced Ultrasonography and Elastography in Infants." *Ultrasonography* 41, no. 4 (2022): 633-649.

● **Zeng Zhang**, Xun Zhou, Alejandro Suarez-Pierre, Cecillia Lui, Sean Kearney, Enoch Yeung, Henry Halperin, Chun Woo Choi, and Joseph Katz. "Time-Resolved Echo-Particle Image/Tracking Velocimetry Measurement of Interactions between Native Cardiac Output and Veno-Arterial ECMO Flows." *Journal of Biomechanical Engineering* 143, no. 2 (2021).

● **Zeng Zhang**, Lihao Feng, Jinjun Wang, and Peiqing Liu. "Gurney-Flap Drag Penalty Reduction with a DBD Plasma Actuator." *Journal of Aerospace Engineering* 30, no. 5 (2017): 04017060.

Conferences

(full-length papers)

● **Zeng Zhang**, Misun Hwang, Todd J. Kilbaugh, Anush Sridharan, and Joseph Katz. "Visualization and Quantification of the Cerebral Microcirculation using Contrast-enhanced Ultrasound Particle Tracking Velocimetry." In *14th International Symposium on Particle Image Velocimetry*, vol. 1, no. 1. 2021.

● **Zeng Zhang**, Joseph Katz, Xun Zhou, Alejandro Suarez Pierre, Cecillia Lui, Sean Kearney, Enoch Yeung, John Young, and Dan Choi. "In Vivo Time-Resolved Echo-PIV Measurement of Cardiovascular Flows with Extracorporeal Membrane Oxygenation." In *13th International Symposium on Particle Image Velocimetry*, vol. 1, no. 1. 2019.

(abstracts & presentations)

● **Zeng Zhang**, Misun Hwang, Todd Kilbaugh, Sophie Haddad, Theodore Cary, Mrigendra Karmacharya, and Joseph Katz. "Assessment of Intracranial Pressure via Ocular Hemodynamics Using Transocular Ultrasound Localization Microscopy." *Bulletin of the American Physical Society* (2022).

● **Zeng Zhang**, Misun Hwang, Todd Kilbaugh, Anush Sridharan, and Joseph Katz. "Application of Echo-PTV and Deep Learning for the Visualization and Quantification of the Cerebral Microcirculation." In *APS Division of Fluid Dynamics Meeting Abstracts*, pp. M03-004. 2021.

● **Zeng Zhang**, Misun Hwang, Todd J. Kilbaugh, Thomas Hallowell, Anush Sridharan, Joshua Y. Choi, and Joseph Katz. "Influence of Intracranial Pressure on the Cerebral Microcirculation in Pig Models with

Hydrocephalus." In *APS Division of Fluid Dynamics Meeting Abstracts*, pp. W08-007. 2020.

- **Zeng Zhang**, Joseph Katz, and Misun Hwang. "Cerebral Vascular Super Resolution Imaging and Blood Flow Measurement Using Ultrasound Enhanced Particle Tracking Velocimetry." In *APS Division of Fluid Dynamics Meeting Abstracts*, pp. H18-005. 2019.

Patent

- Jinjun Wang, **Zeng Zhang**, Lihao Feng, Chong Pan, Qi Gao, Peiqing Liu, Guosheng He, Xi He, *Combined Control Method for Lift-drag Ratio Enhancement.* 2016 CHINESE PATENT, Application No. 201610644119.1.
- Jinjun Wang, **Zeng Zhang**, Lihao Feng, Chong Pan, Qi Gao, *High Performance Wing Based on Bionics Design and DBD Plasma Actuator.* 2016 CHINESE PATENT, Application No. 201610968343.6.

Professional Associations

Student Member of American Physical Society	2018-present

Skill

Fluid Mechanics: Particle Image Velocimetry, Particle Tracking Velocimetry, Computational Fluids Dynamics

Ultrasound: Ultrasound Localization Microscopy, Ultrafast Doppler

Machine Learning: Convolutional Neural Networks, Supervised and Self-Supervised Learning, Neural Partial Differential Equations, Physics Informed Neural Networks

Computer Skills: MATLAB, python